DOCTOR OF SCIENCES

Design, synthesis molecular modelling and biological evaluation of modulators of the NF-kappa activation

Mortier, Jérémie

Award date:
2010

Awarding institution:
University of Namur

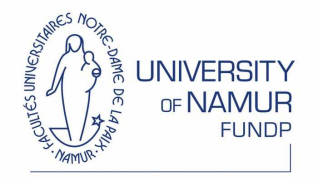

Design, synthesis, molecular modelling and biological evaluation of modulators of the NF-κB activation

Faculté de Médecine
Département de Pharmacie

Dissertation presented by
Jérémie MORTIER
for the grade of Doctor
in Pharmaceutical Sciences

Rempart de la Vierge, 13
B - 5000 Namur (Belgique)

Imprimé en Belgique
ISBN : 978-2-87037-685-0
Dépôt légal: D / 2010 / 1881 / 31

There's a crack in everything
that's how the light gets in.

L. Cohen

Je tiens à remercier chaleureusement l'équipe du Département de Pharmacie de l'Université de Namur au grand complet, en particulier le Professeur Bernard Masereel qui m'honore de sa confiance et son soutien pour la réalisation de ce projet; Raphaël Frederick qui m'a formé et assisté tout au long du travail de modélisation moléculaire présenté dans cette thèse; Lionel Pochet pour ses explications, précisions, argumentations, exemplifications et conclusions exhaustives (toutes choses égales par ailleurs); Carine Bertolla pour sa disponibilité ainsi que toutes ces remarques et conseils pratiques permettant à tout un travail de se mettre en place au quotidien; Julien Deglim pour son écoute, sa disponibilité, ses avis et ses conseils avisés (entre autre en chimie); Eddy Dolusic pour son indispensable expertise en synthèse organique et en new-wave croate; Catherine Marbehant, Mustapha Dinguizli, Nicolas Moniotte et feu Francis-Francis pour leurs encouragements et leurs amitiés; Anne-Marie Murray pour les analyses élémentaires et Jean-Michel Dogné pour ses remarques sur mon travail.

Emmanuel Dejardin ainsi que Corinne Ganeff et Caroline Remouchamps, de l'Université de Liège, furent eux aussi tout à fait indispensables à la réalisation de ce projet. En effet, tous les tests cellulaires décrits dans cette thèse (ainsi que les longues et périlleuses mises au point non décrites) sont le fruit de leur travail. Leur recul vis-à-vis de notre recherche et leur réflexion sur notre démarche furent en tous points critiques pour l'aboutissement de cette thèse. Je les remercie aussi pour leur patience, leur grande disponibilité et leur courtoisie transformant ce projet en une fructueuse et enrichissante collaboration.

Je tiens également à remercier le Professeur Johan Wouters pour ses conseils ainsi que pour la mise à ma disposition de l'infrastructure dont dispose son laboratoire de Chimie Bio-Structurale (CBS), au département de

Chimie de l'Université de Namur. De même, je remercie Marie Ledecq qui m'a assisté durant la première année mon travail de thèse.

Merci à Patrice Talaga, représentant UCB Pharma, parrain du projet, pour sa participation active au projet, ses conseils, ainsi que son aide matérielle (en particulier pour le test multikinase).

Merci aussi à Jaques Piette, Marie-Paule Merville, Alain Chariot et Félicia Patrascu de l'Université de Liège.

Merci à Christine Renard, coordinatrice de la Région Wallonne qui a financé l'intégralité de ce projet (PRALTER n° 0516272).

Merci à Marisa Morata Hurtado pour les corrections grammaticales et orthographiques apportées au manuscrit.

Et enfin, merci aux membres du jury qui me font l'honneur d'évaluer ce travail.

...à la mémoire de Ferdinand Courtoy et de ses fantômes.

ABBREVIATIONS

AKT	RAC-α serine/threonine-protein kinase
Abl	Abelson proto-oncogene
ALK	Anaplastic lymphoma kinases
AP-1	Transcription factor activator protein 1
ATP	Adenosine triphosphate
BAFF	B cell-activating factor
BAFFR	B cell-activating factor receptor
Bcl	Protein family which's founder was discovered at the chromosomal breakpoint of t(14;18) bearing human B-Cell Lymphomas
Bcr	Breakpoint cluster region
BLC	B lymphocyte chemoattractant
$BMimpF_6$	1-Butyl-3-methylimidazolium hexafluorophosphate
CBS	Bio-Structural Chemistry laboratory
CDK4	Cyclin-dependent kinase 4
cIAP	Baculoviral Inhibitor of Apoptosis repeat-containing protein
cKIT	Citokine receptor encoded by the kit gene
CML	Chronic myelogenous (or myeloid) leukemia
COX-2	Cyclooxygenase 2
Cpd	Compound
DDR1	Discoidin domain receptor tyrosine kinase 1
DEC	*N*-(3-dimethylaminopropyl)-*N*'-ethylcarbodiimide
DHMEQ	Dehydroxymethylepoxyquinomicin
DMARD	Disease-modifying anti-rheumatic drug
DNA	Desoxyribonucleic acid
EBV	Epstein Barr virus
EGFR	Epidermal growth-factor receptor
ELC	Epstein-Barr virus induced molecule 1 ligand chemokine
erk	Extracellular signal-regulated kinases
ESI	Ionisation electro-spray
Et	Ethyl
FADD	Fas (TNFRSF6)-associated via death domain
FLS	Fibroblast-like synoviocyte

FRET	Fluorescence resonance energy transfer
GIST	Gastrointestinal stromal tumor
H	Hydrogen
HDAC	Histone Deacetylase
HEK	Human embryonic kidney
HeLa	Cell line was derived from cancer cells taken from Henrietta Lacks
HER	Human Epidermal growth factor Receptor
HS	Hypereosinophilic syndrome
HOBt	1-Hydroxybenzotriazol
HTLV	Human T-cell lymphotrophic virus
ICAM-1	Intracellular adhesion molecule-1
IKK	IκB kinase
IL	Interleukin
ILR	Interleukin receptor
iNOS	Inducible nitric oxyde synthase
IRAK	Interleukin receptor associated kinase
IκB	Inhibitor of NF-κB
JNK	c-Jun N-terminal kinase
KA	*ent*-kaurenoic acid
LIGHT	TNF superfamily member homologous to lymphotoxins
LPS	Lipopolysaccharides
LRR	Leucine rich region
LTB	Lymphotoxin β
LTβR	Lymphotoxin β receptor
MAP	Mitogen activated protein
Me	Methyl
MEK	MAP-erk kinase
MKK	Mitogen-activated protein kinase kinase
mTOR	Mammalian Target of Rapamycin
Myc	Gene encoding for a transcription factor
NDO	Number of different orientations
NEMO	NF-κB essential modulator - also known as IκB kinase gamma (IKKγ)

NF-κB	Nuclear Factor κB
NIK	NF-κB inducing kinase
NLR	NACHT-LRR
NSAID	Non-steroidal anti-inflammatory drug
NSCLC	Non-small cell lung cancer
O	Oxygen
OH	Hydroxy
OMe	Methoxy
PAK	p21 activated kinases
PDB	protein databank
PDGFR	Platelet-derived growth-factor receptor
PDK	3-phosphoinositide dependent protein kinase-1
Ph	Phenyl
PI3K	phosphatidylinositol 3-kinase
PIP_2	Phosphatidylinositol-4,5-bisphosphate
PIP_3	Phosphatidylinositol-3,4,5-trisphosphate
Pr	Propyl
PRR	Pathogen-recognition receptors
RA	Rheumatoid arthritis
RCC	Renal cell carcinoma
Rel	Protein structurally related to the NF-κB family
RHD	Rel Homology Domain
SLO	Secondary lymphoid organ
SRC	Sarcoma (proto-oncogenic tyrosine kinases)
TAK1	TGF-β Activated kinase 1
Tec	Tyrosine-protein kinase encoded by the tec gene
TGF	Transforming Growth Factor
TLC	Thin Lame Chromatography
TLO	Tertiary lymphoid organ
TLR	Toll-like receptor
TMS	Trimethylesilane
TNF	Tumor necrosis factor

TNFL	Tumor necrosis factor ligand
TNFR	Tumor necrosis factor receptor
TRADD	TNFRSF1A-associated via death domain
TRAF	TNFR Associated Factor
VEGFR	Vascular endothelial growth-factor receptor
VS	Virtual screening

A	Ala	alanine	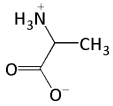	M	Met	methionine	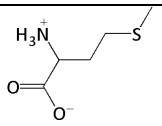
C	Cys	cysteine	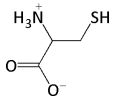	N	Asn	asparagine	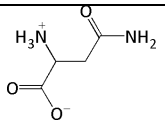
D	Asp	aspartic acid	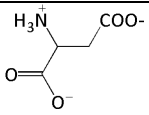	P	Pro	proline	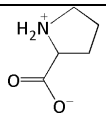
E	Glu	glutamic acid	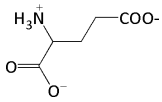	Q	Gln	glutamine	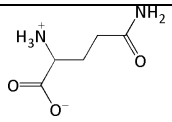
F	Phe	phenyl-alanine	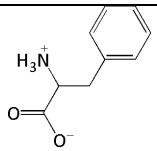	R	Arg	arginine	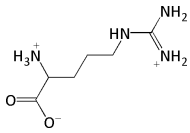
G	Gly	glycine	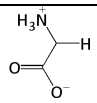	S	Ser	serine	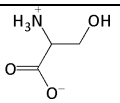
H	His	histidine	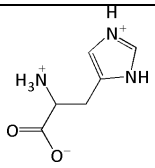	T	Thr	threonine	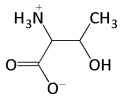
I	Ile	isoleucine	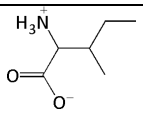	V	Val	valine	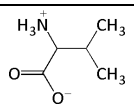
L	Leu	leucine	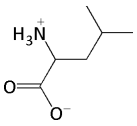	W	Trp	trypto-phane	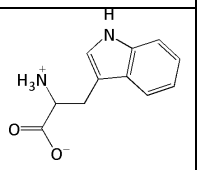
K	Lys	lysine	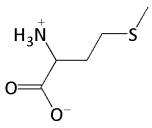	Y	Tyr	tyrosine	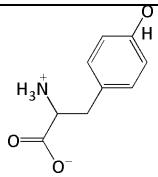

Introduction

1. Rheumatoid Arthritis

Rheumatoid arthritis (RA) is a systemic autoimmune disease affecting around 1-2% of worldwide population with a men/woman ratio of 2.5/1, and a worldwide geographical distribution. Clinically, RA manifests as a symmetric arthritis associated with swelling and pain in multiple joints. It often initially occurs in the joints of the hand, wrists, and feet, but disease onset is insidious in most cases, and several months can elapse before ascertaining a firm diagnosis.[1,2] An inflamed synovium is central to the pathophysiology of RA and the main histological changes are characterised by pronounced angiogenesis, cellular hyperplasia, inflammatory leucocytes influx and changes in the expression of cell-surface adhesion molecules. As the synovial lining becomes hyperplasic, the sublining undergoes striking alterations in cellular number and content (T cells, B cells, macrophages and plasma cells).[1] A locally invasive synovial tissue (pannus) is then formed, growing into the synovium region and leading to the progressive destruction of cartilage and bone (Figure 1).[3,4]

Many cytokines such as tumor necrosis factor α (TNFα) and interleukin-1β (IL-1β) are abundant in RA synovium.[5-7] Produced by macrophages and fibroblast-like synoviocytes (FLS), TNFα and IL-1β likely contribute to synovial inflammation by stimulating fibroblast proliferation and increasing production of various cytokines, chemokines as well as enzymes that result in irreversible joint destruction. In turn, these cytokines can activate macrophages in the environment and lead to continued cytokine production.

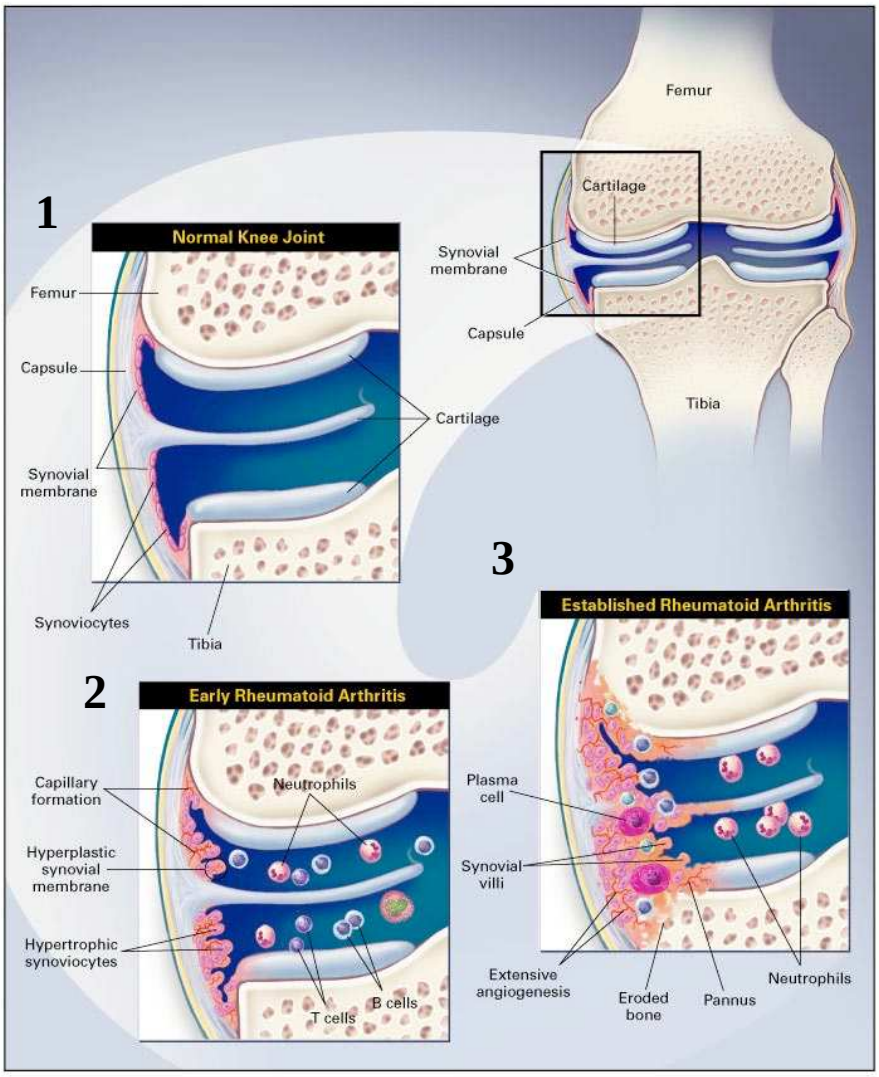

Figure 1: Evolution of RA in knee joint[8]

Such conditions create a positive feedback mechanism between FLS and macrophages, perpetuating synovial inflammation.[9] In the synovium, these inflammatory mediators activate multiple intracellular signal transduction and transcription factor pathways. Most of these signalling pathways lead to the activation of the transcription factor NF-κB, the transcription factor activator protein 1 (AP-1) and the mitogen activated

protein (MAP) kinases cascade which are especially central in the regulation of synovial inflammation.[10] In 2002, the importance of NF-κB in constitutive TNFα production in RA was demonstrated, predicting that blocking NF-κB should be an effective therapeutic target for this pathology.[11]

2. Therapeutic principles

Medications which are used to treat RA are divided into four main classes:

1. non-steroidal anti-inflammatory drugs (NSAIDs) including cyclooxygenase-2 (COX-2) inhibitors;
2. corticosteroids ;
3. disease-modifying anti-rheumatic drugs (DMARDs);
4. biologic agents.

NSAIDs are particularly helpful during the first few weeks in which the patient develops symptoms. These drugs provide partial relief of pain and stiffness until a definitive diagnosis of RA can be established.[12] Both traditional NSAIDs and COX-2 inhibitors have been associated with various side effects (gastric and duodenal ulcers, increased fluid retention, exacerbation of hypertension, impairment of renal function in susceptible patients).[13-16]

Corticosteroids are also potent suppressors of the inflammatory response in RA despite their dose-dependent side effects (skin thinning, cataracts, osteoporosis, hypertension and hyperlipidemia).[12,17,18] Controversy continues about their therapeutical scheme in the treatment of RA. Nevertheless, some studies established that corticosteroids decrease the progression of RA.[19,20]

Considering that drugs should be used to slow down the damage caused by the disease rather than simply to control symptoms led to the introduction of various agents known as DMARDs.[21] These drugs are defined as medications that delay or stop the progression of the disease.[12] Methotrexate emerged as the lead molecule of the antirheumatic arsenal (Figure 2).[22] This antimetabolite and antifolate drug was shown to have a considerable protective effect in terms of joint destruction.[23,24] It demonstrated efficacy, durability, acceptable toxicity and low cost.[12,25] An observational study has shown that patients with RA who have been treated with methotrexate have significantly lower mortality than untreated patients.[26] Methotrexate became then the most widely used, alone or in combination with other DMARDs (like sulphasalazine or hydroxychloroquine).[12,27]

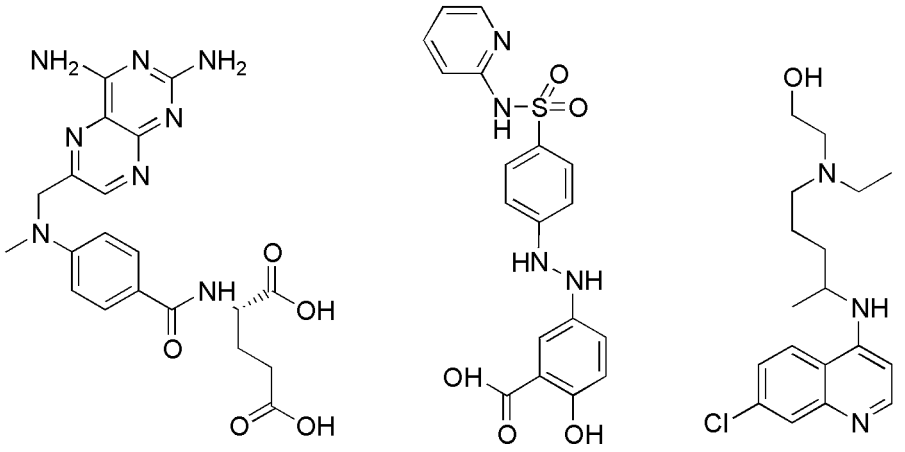

Figure 2: Methotrexate, sulphasalazine and hydroxychloroquine (from left to right)

But, as the last 20 years have seen an accumulation of insights into the pathogenetic pathways, new therapeutic targets have been identified.[8] One of the major advances in the treatment of RA occurred with biologic agents (also known as biologic DMARDs) produced through expression of recombinant DNA and modifying the immune response by blocking the

effect of the pro-inflammatory cytokines.[28] In 1999, infliximab (a monoclonal antibody, figure 3) and etanercept (a fusion protein) were the first anti-TNFα registered and marketed. Then, several new biologic agents were designed to target specific cytokines like IL-1 and TNFα,[29] or cell surface molecule like IL-1R,[30] IL-6R,[29,31] and CD20 (phosphoprotein expressed on the surface of all mature B-cells).[32,33] Thousands of patients have then been treated with anti-TNFα, leading to the identification of multiple mechanisms of action for these medications.[34] However, a wider use of TNFα antagonists resulted in reports of adverse effects including serious bacterial infections (i.e. tuberculosis),[35-39] cancer,[40] injection-site and infusion reactions (like headache or nausea),[41] immune and autoimmune disease (because of a reduction of the antibodies formation),[29,42] demyelinating syndromes,[43] and heart failure.[44]

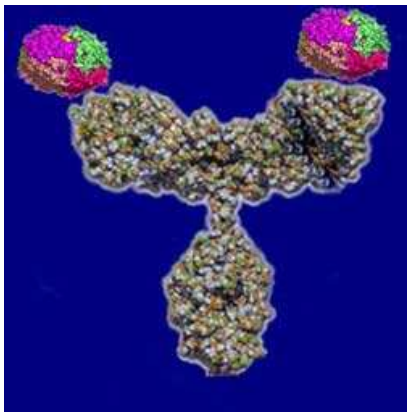

Figure 3: infliximab-TNFα complex[45]

Morevover, controversies are reported in RA management: should biologic agents be used as first-line therapy? Should glucocorticoid therapy be used in early RA? Should these drugs be switched or cycled? In what order? Nevertheless, majority of trials support the overall superiority of combination therapies.[22] The most widely used treatment for RA is the

combination of an anti-TNFα and methotrexate,[21] but such issues clearly indicate a strong need in new approaches in the treatment of RA. Moreover, if methotrexate is a cheap medication (3 €/month/patient in Belgium, in 2009), anti-TNFα like infliximab or adalimumab are very expensive drugs (between 1100€ and 1200€/month/patient in Belgium, in 2009).[46,47] This high cost illustrates the necessity of novel therapeutic strategies. Finally, cure remains an elusive goal and true remission is achieved by only a minority of patients. Destructive process cannot be stopped as well as repair of previous damage is unreached in most of patients. It remains a considerable unmet need in RA therapy. Fortunately, several alternative strategies are currently being investigated raising hope for a better future for patients with this disease. Modulation of the NF-κB alternative activation pathway is a promising approach considering results published by Dejardin *et al.*[48] and Claudio *et al.*[49] In the following section, the two main NF-κB activation pathways are described in order to clarify the interest of this new strategy.

3. NF-κB activation

Initially identified in activated B cells, the transcription factor NF-κB rapidly emerged as essential for both innate and adaptative immunity, cell survival, apoptosis and inflammation among others.[50-53] Being activated in the RA synovium, this transcription factor controls the transcription of inflammatory genes implicated in RA, including TNFα, IL-1, IL-6, IL-8, COX-2, inducible nitric oxyde synthase (iNOS) and intracellular adhesion molecule-1 (ICAM-1).[54] In mammals, the Rel/NF-κB family is comprised of p65 (Rel-A), c-Rel (Rel), Rel-B, p50 and p52. These structurally related proteins share extensive sequence similarities within their N-terminal Rel

Homology Domain (RHD) that enables them to dimerise, to translocate into the nucleus, and to bind to specific DNA sequences, named κB sites. Among the Rel/NF-κB family, only p65, c-Rel and Rel-B contain a C-terminal transcriptional activation domain. Therefore, they are able to directly activate the transcription. The two other members, p50 and p52, are synthesised as precursors called p105 and p100, respectively. Proteins p50 and p52 can behave as transcriptional activators only upon dimerisation with p65, c-Rel, RelB or Bcl3.[55]

It has been shown that two main pathways control the activation of NF-κB. The first one, named classical NF-κB pathway (or canonical), is triggered by inflammatory cytokines such as TNFα, IL-1, or by bacterial and viral proteins through pathogen-recognition receptors (PRR) like TLRs and NLRs (Figure 4).[56] These inducers activate the recruitment of specific adaptor proteins to their cognate receptors, which enable the activation of a cascade of kinases. Among them, TGF-β activated kinase 1 (TAK1) plays a key role at the crossroad of the NF-κB and MAPK signalling pathways (Figure 4). TAK1 is part of the MAP kinase subfamily.[57] However, some studies showed that IL-1β and TNFα signalling pathways are affected in TAK1 KO mice.[58,59] TAK1 activates the IKK complex by phosphorylating the IKKβ subunit. Moreover, TAK1 acts on MKK6 to trigger the activation of p38 and JNK (Figure 4). Upon TAK1 activation, the activated IKK complex phosphorylates IκBα, the main inhibitor of the classical NF-κB pathway, releasing NF-κB (e.g; p50/p65), which finally, translocates into the nucleus.[60] This pathway is activated within minutes and relies on the indispensable adaptor protein NEMO (or IKKγ), holding together IKKβ and IKKα to form the IKK complex.

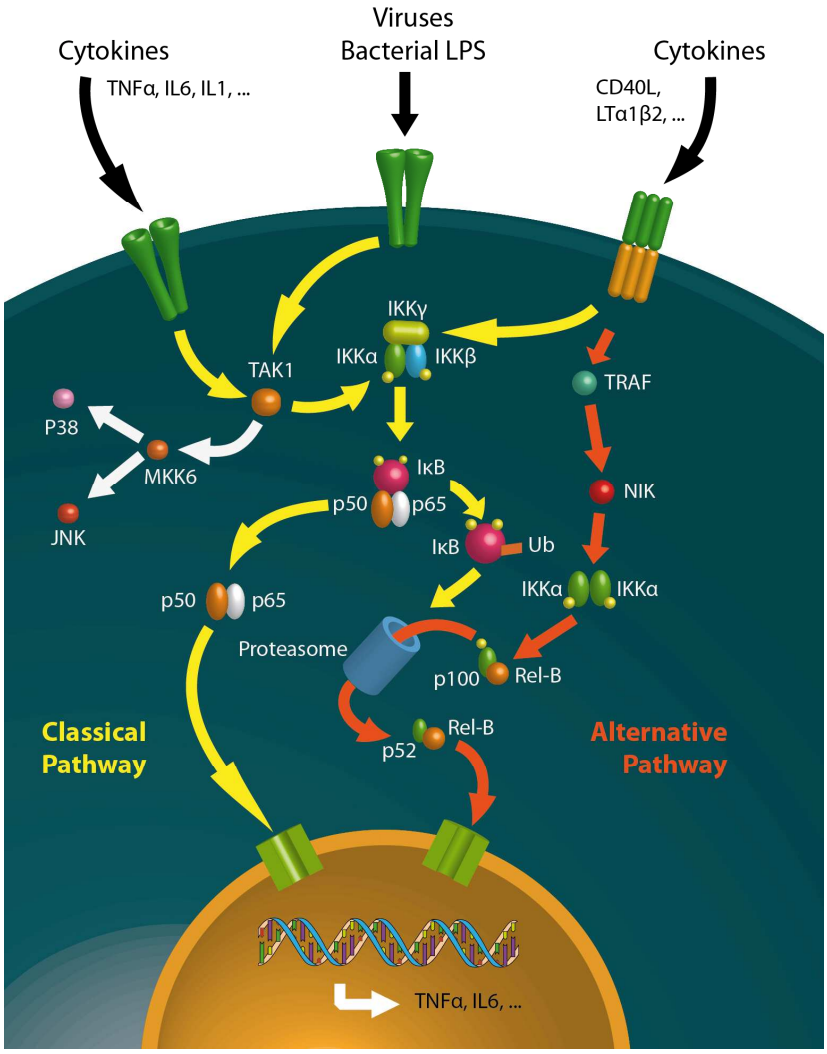

Figure 4: Classical (yellow) and alternative (orange) NF-κB activation pathways.

The second NF-κB pathway, called alternative NF-κB pathway (or non-canonical), is induced by a subset of TNFL family members as well as by some viral proteins.[61] This pathway is dependent on the stabilisation and activation of the kinase NIK. The half-life of this particular kinase is negatively controlled by TRAF2, TRAF3, c-IAP-1 and c-IAP-2.[62,63] Upon

activation of receptors like CD40, BAFF or LTβR, the inhibitory function of TRAF2 and TRAF3 is alleviated. Then, stabilised NIK activates IKKα leading to the processing of p100 into p52 (Figure 4).[48,49,64] The latter, in association with its main partner Rel-B, fulfils non-redundant biological functions such as secondary lymphoid organ (SLO) development and induction of specific chemokines involved in adaptative immunity.[61]

4. NF-κB alternative pathways as a therapeutic target

There is no doubt that cytokines inducing or produced by the NF-κB alternative pathway are involved in inflammatory disorders. LTβR was demonstrated as a master receptor involved in the development of secondary lymphoid organ (SLO), and molecular mechanisms controlling tertiary lymphoid organ (TLO) formation required LTβR as well.[61] TLO are organized lymphocytic aggregates (B cell and T cell areas) forming at sites of chronic inflammation.[65,66] Unlike SLO, TLO are not connected to afferent lymph vessels and are not encapsulated, which implies that they are directly exposed to stimulating antigens and pro-inflammatory cytokines. TLO arises typically in non-lymphoid locations but the identity of stromal cells initiating their development is unknown. Nevertheless, TLO formation was observed in several mouse models of chronic inflammatory pathologies but also in transgenic mice by ectopic expression of inducers or target genes of the alternative pathway.[66] For instance, constitutive tissue specific expression of LTβ, BLC (B lymphocyte chemoattractant) or ELC (Epstein-Barr virus induced molecule 1 ligand chemokine) into pancreatic islets or kidney is sufficient to generate TLO.[66] It is noteworthy that TLO has been detected in a significant percentage of patients suffering from several chronic

inflammatory diseases like RA, but also Sjogren's syndrome, multiple sclerosis, ulcerative colitis or chronic hepatitis C.[65] Thus, inhibition of LTβR function in SLO and/or TLO could be beneficial for the treatment of chronic inflammatory pathologies. Actually, administration of LTβR-Ig fusion proteins (acting as a decoy receptor for LTα1β2 and LIGHT) has been successfully used in a rodent disease model of collagen-induced arthritis or inflammatory bowel disease. This approach is under clinical investigation.[67]

Besides TLO formation, another hallmark of most autoimmune diseases is the exacerbated expression of the prosurvival BAFF. In the synovial fluid of patients with RA, a high concentration of this cytokine is observed and these conditions allow the survival of unwanted autoantibody producing B cells.[68] Tremendous efforts have been accomplished for the development of biological antagonists of BAFF, such as anti-BAFF antibody or decoy receptors for BAFF.[69] The rational of using specific inhibitors of NF-κB alternative pathway would be their property to inhibit simultaneously several TNFR mediating pathologic conditions, like LTβR and BAFFR. As NIK has been shown to be critical for antigen-mediated induction of bone erosion in several mouse models,[70] this kinase certainly represents an attractive candidate. Thus, inactivation of NIK with chemical compounds could have the advantage to spread the inhibition at levels of multiple effectors of chronic inflammation.[61]

As the NF-κB transcriptional activation is associated with essential cell functions, aberrant NF-κB regulation is also observed in many cancers.[71] Various mouse models in which IKK/NF-κB activation has been blocked by molecular biology highlighted the key role of NF-κB as a crucial promoter of inflammation linked cancers.[72-74] One of the most documented functions of NF-κB is its ability to promote cell survival through the induction of

target genes, the products of which inhibit the apoptotic machinery in both normal and malignant cells.[75,76] NF-κB also prevent programmed necrosis by inducing genes encoding antioxidant proteins.[76] As tumour cells frequently use NF-κB to achieve resistance to anticancer drugs and radiation therapy, inhibition of NF-κB activation emerge as a promising option to improve the efficacy of conventional anticancer therapies.[71] Although, in this work, we focused on NF-κB related inflammatory disorders and the potential interest of NIK as therapeutic target.

5. NF-κB inducing kinase

First described in 1997, NIK (or MAP3K14) is a serine/threonine kinase belonging to the MAP3K family. 947 amino acids constitute this protein which contains a 256 residues kinase domain (from 400 to 655 - Figure 5).[77]

Upstream in the NF-κB activation cascade, members of the TRAF family interact with NIK as negative regulators (TRAF2 and TRAF3).[78] Interactions of the N-terminal domain of NIK with TRAF3 induce constitutive degradation of NIK by 19S proteasome, keeping alternative activation pathway under control.[63] On the other side, interactions between NIK et IKKα was demonstrated. It occurs with the C-terminal domain of NIK (residues 735 to 947) and induces IKKα phosphorylation on serine 176 (Figure 5).[79]

Little information is reported in the literature concerning the ATP binding site of this kinase. Only three residues are described as essential for the activity of NIK: KK429-430 and T559 (Figure 5). On one hand, as the double mutant KK429-430AA disabled NIK, it was presumed that at least

one lysine induces the stabilisation of the phosphate transfer in the kinase pocket.[77] On the other hand, T559, belonging to the activation loop of NIK, is reported as a phosphorylation site. As the phosphorylation of T559 induces the amplification of the kinase activity of NIK, the T559A mutant reduces the IKKα phosphorylation by NIK.[80]

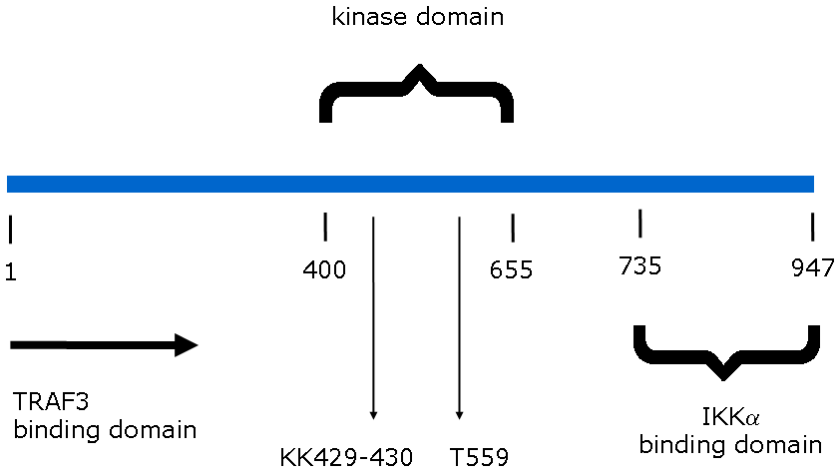

Figure 5: Primary structure of NIK

From a structural point of view, no data of the 3D-structure of NIK are available, as well as the molecular mechanism or the potential interactions of its kinase domain with ATP or IKKα.

6. Kinase ATP binding site

Protein kinases catalyse the transfer of the distal phosphate group from adenosine triphosphate (ATP) to the hydroxyl group of a serine, a threonine or a tyrosine residue of the kinase itself or another protein substrate. Phosphorylation can create new recognition sites for protein

binding or may alter the conformation of the phosphorylated enzyme and modify its activation state or function.[81-83] Protein kinase enzymes play pivotal roles in signal transduction from the cell membrane to the nucleus and in the cell-cycle control.[84]

High structural similarities of kinase ATP binding sites lend itself to a description of key regions and interactions observed across the kinome (Figure 6). Most of them have a common fold consisting of two lobes. The N-terminus lobe consists of five antiparallel β-strands and one α-helix. Conversely, the C-terminus lobe is highly helical (Figure 6).

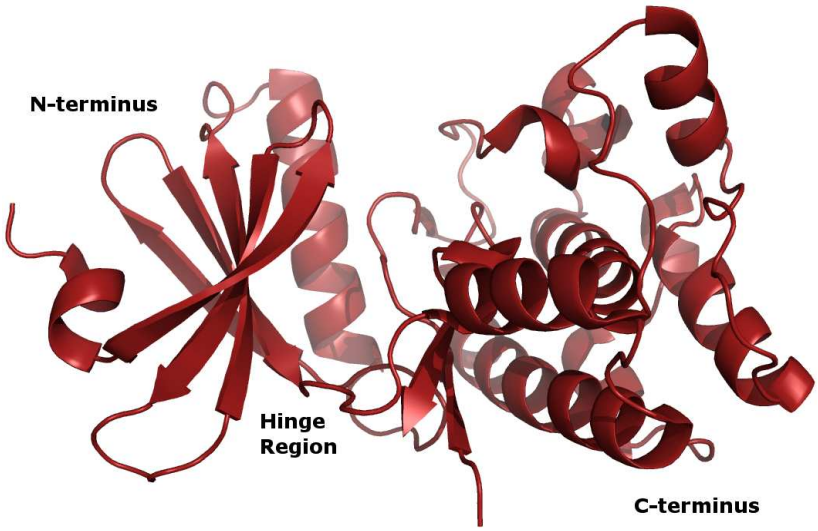

Figure 6: 3D structure of a kinase domain [85]

The ATP binding site is a narrow hydrophobic pocket located between the two lobes which are linked by a flexible hinge region (Figures 6 & 7). The top of the ATP binding site is formed by the G-loop, known as the glycine-rich loop for its highly conserved GXGXXG motif (Figure 7).

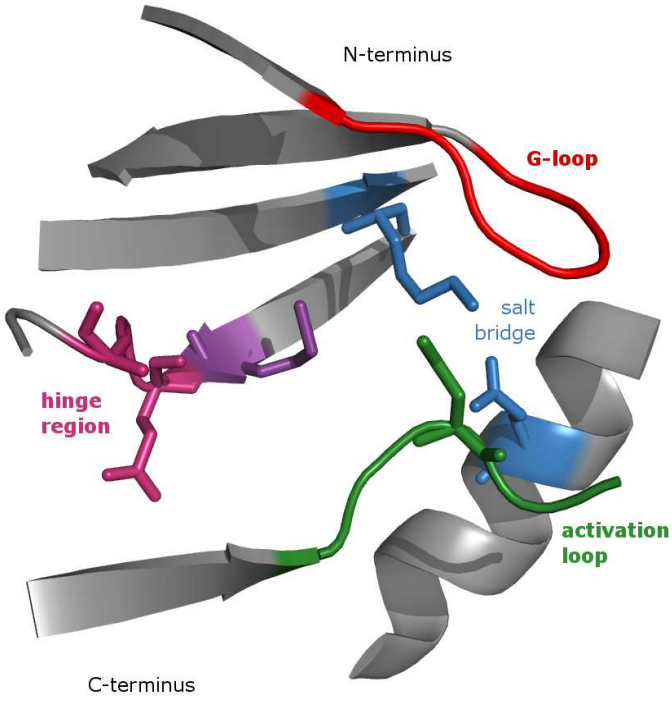

Figure 7: 3D ATP-binding site with G-loop (red), hinge region (pink), gatekeeper (magenta), activation loop (green) and salt bridge (blue)

Kinases have a second loop (called activation loop, figures 7 & 8) containing serine, threonine, or tyrosine residues, which may be phosphorylated. The N-terminal side of the activation loop is a highly conserved DFG triplet. The aspartate residue (D) is catalytically involved in the phosphate transfer, and typically engaged in a salt bridge interaction with a conserved lysine residue and an aspartate/glutamate residue (Figure 8). This activation loop occupies a part of the ATP binding site when these residues are not phosphorylated. Most of ATP-competitive inhibitors recognise the so-called "active conformation" of the kinase.[86] But targeting this site with ligand-protein interactions is not the only way to enhance inhibitor selectivity. When the catalytic aspartate of the DFG triplet is in a rotated-out conformation (known as DFG-out), it rotates out of the ATP

binding pocket, and it is accompanied by a corresponding rotation of the adjacent phenylalanine (F) and glycine (G) residues.[87] The phenylalanine movement reveals a large hydrophobic pocket which may be filled by complementary groups of the ligand. The marketed drug imatinib targets this DFG-out conformation, emphasising the potential importance of this conformational state in ligand design.[88,89]

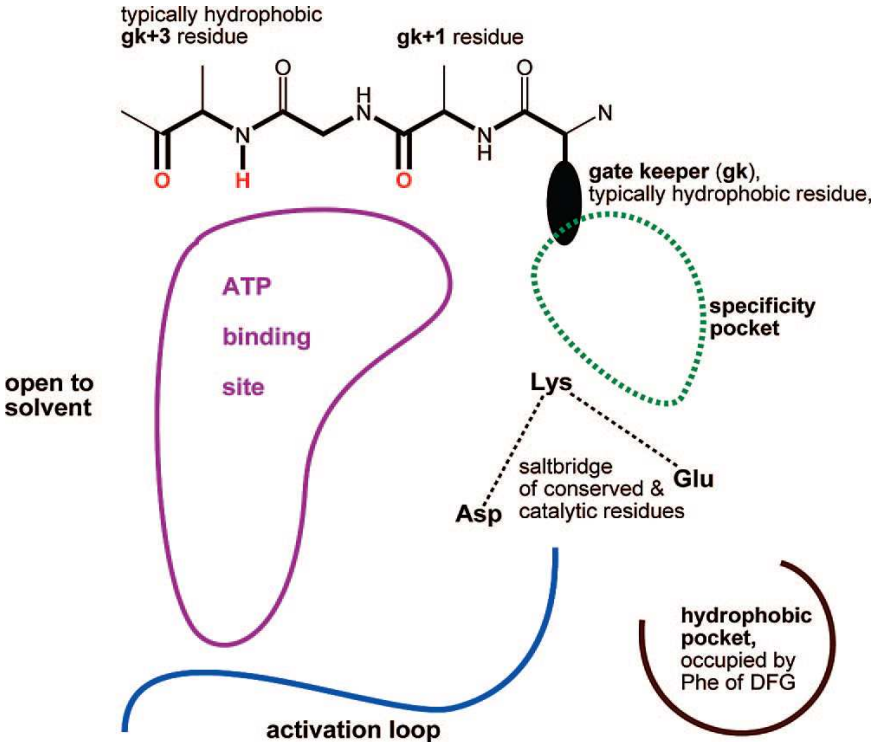

Figure 8: 2D representation of a typical kinase ATP-binding site.[90]

The gatekeeper (gk) is another important amino acid of the ATP binding site (Figure 8). The size and the volume of the side chain of this residue dictate the access to the hydrophobic pocket located behind the gatekeeper, thereby defining a potential inhibitor selectivity of the ATP site. The peptide bonds forming the key hydrogen bond acceptor motifs in the

hinge region are thusly referenced as gk+1 and gk+3,[90] relative to the position of the gatekeeper:

hinge residues = gk + 1 and gk + 3

Usually, the hinge region has one hydrogen as donor flanked by two oxygen regarded as acceptors. Interestingly, these atoms derived from the protein backbone and not from the side-chains of the residues gk+1 and gk+3. These residues recognise the ATP-purine moiety and stabilise the nucleotide into the pocket by two or three critical H-bonds. This region is also known to be targeted for the design of ATP-competitive inhibitors.[90]

Kinases are at the crossroad of controversies regarding their status as drug targets. As the cellular concentration of ATP is high, typically 1–5 mM,[91,92] it was thought that a high concentration of ATP-competitive inhibitor would be needed, bringing potential toxicity. Another concern is that all protein kinases share a common cofactor and a similar three-dimensional structure of the catalytic site. These features increase the difficulties for the design of adequate and selective kinase inhibitors. But it can be seen that these have been successfully challenged. Currently, ten approved kinase inhibitors binding in the ATP binding site are marketed for the treatment of various diseases (Table 1).[84,86,93]

Being firstly discovered as a product of the bacterium *Streptomyces hygroscopicus*, the mTOR (mammalian target of rapamycin) inhibitors rapamycin (also known as sirolimus) and temsirolimus are macrolides with a high molecular weight (914 g/mole and 1030 g/mole respectively).[94] They are not reported in table 1. The eight others inhibitors present ordinary structures and are indicated in the reported diseases (Table 1):

Table 1: Chemical structure and known kinase targets for clinically approved kinase inhibitors.[93,94]

Structure	Name	Known targets	Indication
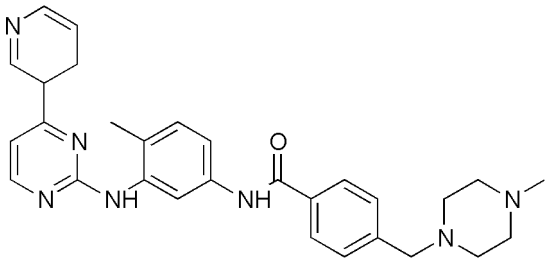	Imatinib (Glivec; Novartis)	Bcr-Abl, c- Abl, PDGFR, c-KIT, DDR1	CML, GIST, HS
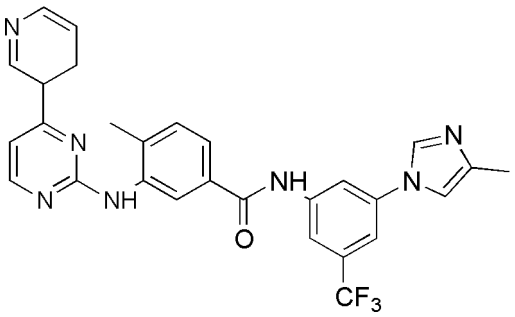	Nilotinib (Tasigna; Novartis)	Bcr-Abl, c- Abl, PDGFR, c-KIT, DDR1	Imatinib-resistant CML
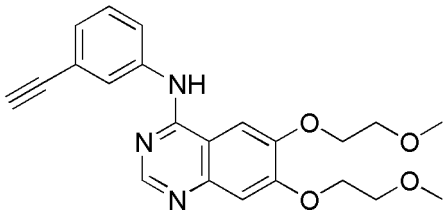	Erlotinib (Tarceva; OSIPharma /Genentech /Roche)	EGFR, HER2	NSCLC, pancreas cancer
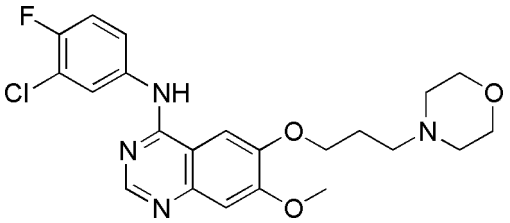	Gefitinib (Iressa; Astra Zeneca)	EGFR, HER2, HER4	NSCLC
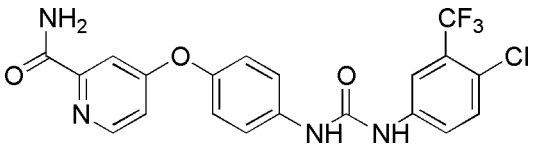	Sorafenib (Nexavar; Bayer /Onyx)	c-KIT, PDGFR, VEGFR (b-raf)	Renal cancer

Structure	Name	Known targets	Indication
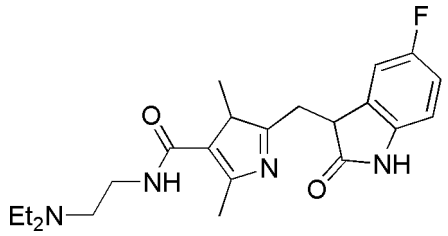	Sunitinib (Sutent; Pfizer)	c-KIT, PDGFR, VEGFR	Renal cancer, imatinib-refractory GIST
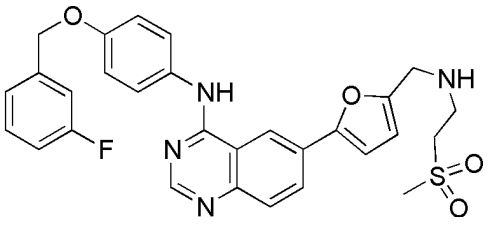	Lapatinib (Tykerb; GSK)	HER2	Breast cancer
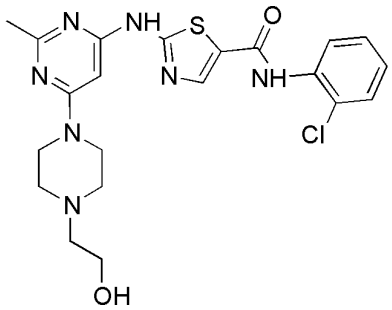	Dasatinib (Sprycel; Bristol-Myers Squibb)	Bcr-Abl, SRC family, Tec family	Imatinib-resistant CML

CML, chronic myelogenous leukaemia; DDR1, discoidin domain receptor tyrosine kinase 1;EGFR, epidermal growth-factor receptor; GIST, gastrointestinal stromal tumours; HES, hypereosinophilic syndrome; NSCLC, non-small cell lung cancer; PDGFR, platelet-derived growth-factor receptor; VEGFR, vascular endothelial growth-factor receptor.

Interestingly, while the initial research focused largely on the discovery of monospecific or highly selective kinase inhibitors for therapeutic use, the clinical experience, and a growing understanding of kinase biology show that molecules with a broader pattern of inhibitory activities can be even more effective.[95-97]

7. NIK inhibitors

Surprisingly, despite a demonstrated high interest for the NF-κB alternative pathway, and particularly for NIK inhibition, only three series of molecules are described as NIK inhibitors in the literature: kaurenes **1-3**, alkynyl alcohols **4** and pyrazolo[4,3-*c*]isoquinolines **5**:

7.1 Kaurenes

Kaurenes are tetracyclic diterpenes (Figure 9). These asymmetric hydroxylated molecules derived from the *ent*-kaurenoic acid (KA), isolated from plants like *Viguiera robusta*. In 2001, NIK was reported by Castrillo *et al*. as one of the potential target of compounds **1-3**.[98]

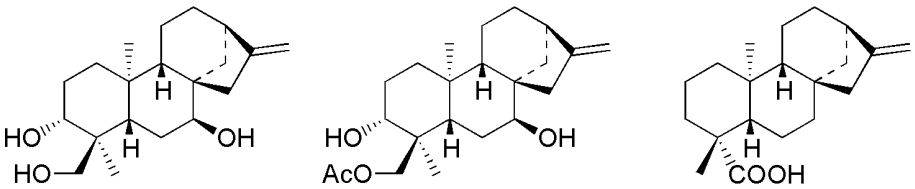

1 **2** **3**

Figure 9 : Kaurene reported as potential NIK inhibitors

In the published results, the authors reported various assays based on LPS-activated cells treated with kaurene diterpenes. Unfortunately, as the alternative activation pathway was not yet described, the authors did not consider the two pathways distinctly. Their results suggest that kaurenes inhibit a step preceding IKKβ activation. Briefly, cells were then transfected with a Myc-NIK expression vector which, after overexpression, triggers IKKβ activation *per se*.[77,99] In these conditions, the authors indicated that kaurenes inhibited the Myc-NIK-dependent activation of IKKβ in the absence of LPS stimulation. Although, some observations suggested that

IKKβ and NIK are involved in two distinct pathways.[61] Anyway, NIK and IKKβ interdependence remains unclear.[100] These conclusions are therefore not obvious and an enzymatic assay would clarify their assumptions. No further data on this series have been published.

7.2 Patents on alkynyl-alcohols and pyrazolo[4,3-*c*]isoquinolines

On december 2009, a new series was published as NIK inhibitor. The corresponding patent was based on the alkynyl-alcohol **4** moiety (Figure 10).[101] Unfortunately, neither biological data nor structure-activity relationships related to this series were described in the original patent.

Up to 2009, the pyrazolo[4,3-*c*]isoquinoline template **5** was the only scaffold reported and claimed as NIK inhibitor (Figure 10). This series was submitted in 2002 and then published in 2005 by Aventis as a patent.[102,103] This patent reports: *(...) pyrazoloisoquinolines derivatives are strong and very specific inhibitors of NIK (...).* It is also claimed: *a method of treating a disease condition associated with the increase activity of NIK comprising administering to a patient suffering from said disease condition a therapeutically effective amount of a compound of the formula* **5** (Figure 10) *or a stereoisomeric form or a pharmaceutically acceptable salt of this compound* **5**.

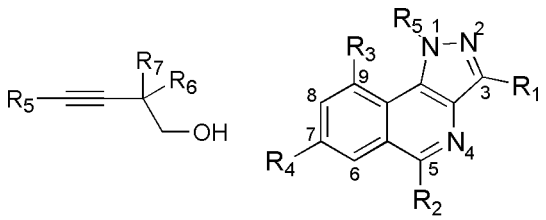

4 **5**

Figure 10: Alkynyl-alcohol **4** and pyrazolo[4,3-*c*]isoquinolinyl **5** scaffolds

8. Objectives

As the intracellular signal transduction responsible for the survival of immunity cells is identified and associated with the early development of RA, it might be valuable to design a novel class of inhibitors targeting kinases at the crossroad of multiple pathways relevant to this pathology. As NIK definitely represents an attractive target, we aim, on one hand, to understand and characterise this protein and, on the other hand, to discover, design and synthesise new inhibitors. Being the strongest starting point to identify new inhibitors of NIK, we decided to clarify the inhibitory mechanism of pyrazolo[4,3-*c*]isoquinolines. The study of the interactions of these pyrazolo[4,3-*c*]isoquinolines with NIK was one of our main goals. To reach it, we will proceed according to the following steps:

1. Molecular modelling and mutagenesis will be performed to study the kinase domain of NIK.
2. The only scaffold described as NIK inhibitor, the pyrazolo[4,3-*c*]isoquinoline scaffold **5** will be considered in a 3D-model of NIK to identify the main potential interactions between these inhibitors and their target.
3. Novel pyrazolo[4,3-*c*]isoquinolines will be synthesised and their inhibitory potency and specificity will be evaluated on isolated NIK and in a cellular test.
4. A virtual screening of molecular databases will be developed to identify an original scaffold for the design of NIK inhibitors.
5. Various analogues of the most promising compounds will be synthesised to start a new and original series of NIK inhibitors.

Results

1. Molecular modelling

To learn more about the ATP-binding site of NIK and to understand the enzymatic mechanism, a molecular modelling study was initiated in collaboration with the CBS laboratory of Professor J. Wouters. This study enabled to identify the nature of amino acids located into the catalytic cavity and to understand the potential interactions that could exist between those residues and NIK ligands. Molecular modelling is then a tool to interpret activity results, to rationalise structure-activity relationships and to improve the affinity and selectivity of target modulators. Finally, molecular modelling is very helpful for designing novel structures and may therefore cooperate closely with organic synthesis. Since no crystal structure or 3D-model of NIK was available, we started to build a 3D model of NIK.

1.1 Sequence homology

The first step of a homology modelling is the identification of a protein used as template. The 3D-structure of the template has to be available and its amino acids sequence must be as close as possible to the sequence of NIK. Such research is possible by means of a sequence alignment software (BLASTP) dealing with every protein available in the Protein DataBank (PDB).[104,105] On the day of this experiment (October 9th, 2006), the closest accessible crystallised kinase was PAK1 (p21 activated kinase 1; PDB code: 1YHW-A), the first reported protein of the aligned sequences list (Figure 11) :

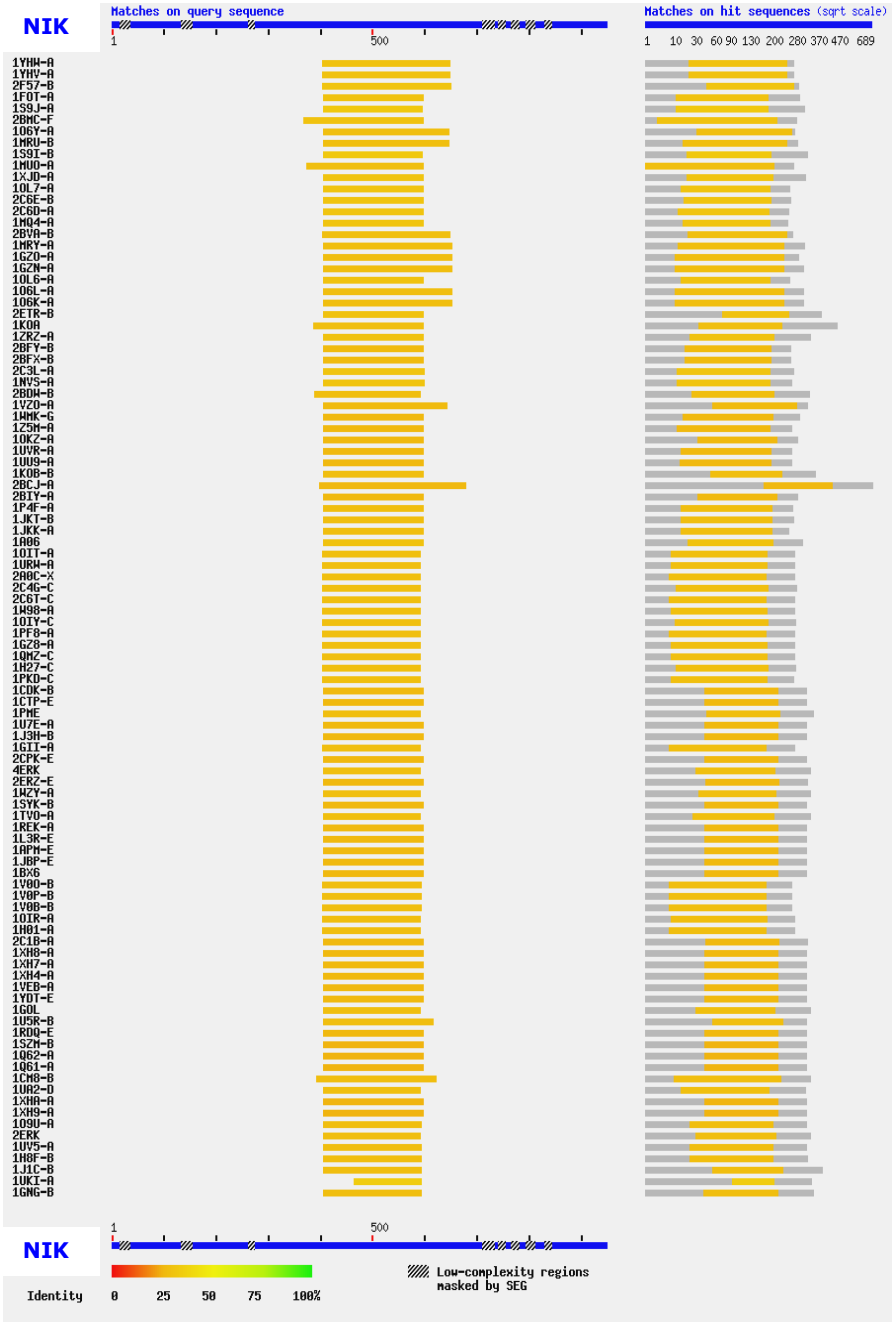

Figure 11: Sequences alignment to NIK performed by BLASTP software. PAK1 is represented by the code 1YHW-A. A colour code represents the identity level of each aligned sequence and NIK.

PAK1 shares 30% sequence identity and up to 48% sequence homology (similar residues) with NIK (Figures 12 and 13). As this value is satisfying enough to build a model, PAK1 was then chosen to be the pattern structure (template) to build the 3D kinase domain of NIK.

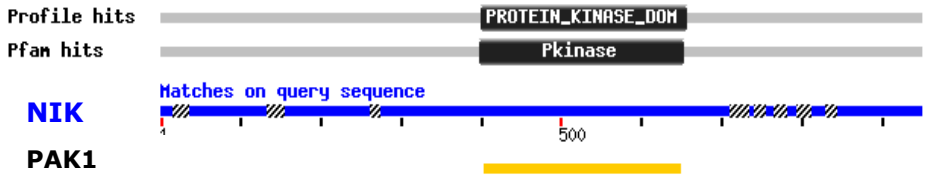

Figure 12 : Unidimentional alignment of NIK (blue) and PAK1 (yellow, kinase domain only)

The proper alignment of PAK1 and NIK sequences by BLASTP is reported below (Figure 13):

```
pdb  1YHW-A  Chain A, Crystal Structure Of Pak1 Kinase Domain With One Point
     1YHW    Mutations (K299r)
             pdb|1F3M|D Chain D, Crystal Structure Of Human SerineTHREONINE KINASE PAK1
             pdb|1F3M|C Chain C, Crystal Structure Of Human SerineTHREONINE KINASE PAK1 (PAK1_HUMAN, Q13153)

 Score =  104 bits (259), Expect = 1e-22
 Identities = 76/248 (30%), Positives = 121/248 (48%), Gaps = 12/248 (4%)

Query: 405 RLGRGSFGEVHRMEDKQTGFQCAVKKVRLEVFRAEELMACAGLT-----SPRIVPLYGAV 459
           ++G+G+ G V+    D  TG + A++++ L+    +EL+    L      +P IV    +
Sbjct: 27  KIGQGASGTVYTAMDVATGQEVAIRQMNLQQQPKKELIINEILVMRENKNPNIVNYLDSY 86

Query: 460 REGPWVNIFMELLEGGSLGQLVKEQGCLPEDRALYYLGQALEGLEYLHSRRILHGDVKAD 519
             G  + + ME L GGSL  +V E  C+ E +      + L+ LE+LHS +++H D+K+D
Sbjct: 87  LVGDELWVVMEYLAGGSLTDVVTET-CMDEGQIAAVCRECLQALEFLHSNQVIHRDIKSD 145

Query: 520 NVLLSSDGSHAALCDFGHAVCLQPDGLGKSLLTGDYIPGTETHMAPEVVLGRSCDAKVDV 579
           N+LL  DGS   L DFG    + P+   +S +      GT   MAPEVV  ++   KVD+
Sbjct: 146 NILLGMDGS-VKLTDFGFCAQITPEQSKRSTMV-----GTPYWMAPEVVTRKAYGPKVDI 199

Query: 580 WSSCCMMLHMLNGCHPWTQFFRGPLCLKIASEPPPVREIPPSCAPLTAQAIQEGLRKEPI 639
           WS   M + M+ G  P+           IA+   P  + P   + +    +   L  +
Sbjct: 200 WSLGIMAIEMIEGEPPYLNENPLRALYLIATNGTPELQNPEKLSAIFRDFLNRCLDMDVE 259

Query: 640 HRVSAAEL 647
            R SA EL
Sbjct: 260 KRGSAKEL 267
```

Figure 13: Sequence aligning of NIK (Query) and PAK1 (Subject) by BLASTP

1.2 3D-model building

As the target/template alignment step is known to be critical for the quality of a model, we used the automated homology program *ESyPred3D*.[106] This performs a consensus alignment between the sequences of the target and the template. Then *MODELLER* generates the 3D coordinates.[107] The final 3D model of NIK shows a classical kinase structure with the N-terminus side constituted by five anti-parallel β-strands, the C-terminus side rich in α-helixes, and a cavity, in the middle of the protein, bordered by a flexible hinge region (Figure 14).

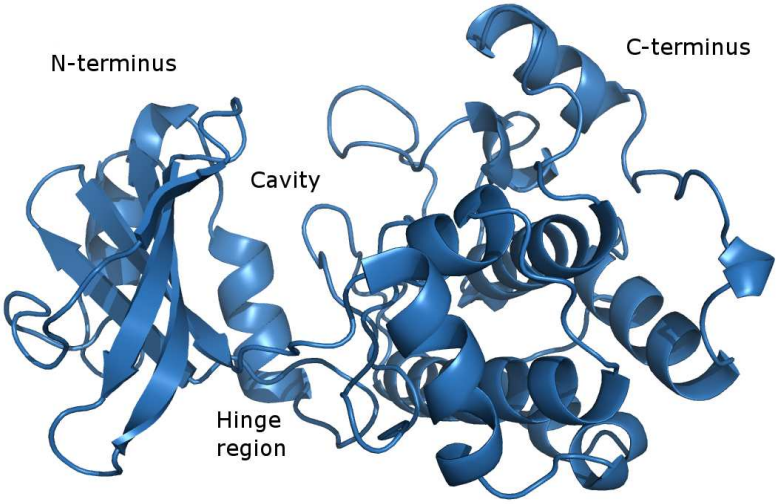

Figure 14: 3D-model of NIK (kinase domain)

The catalytic pocket of NIK was refined by minimisation to take into account the protein flexibility. The position of the side-chains of the residues located 20 Å around L472 (the gk+3 hinge residue)[a] were minimised by means of the *MINIMIZE* module, as implemented in *SYBYL 8.0*.[108]

[a] Hinge residues, named gk+1 and gk+3 relatively to the gatekeeper position, are fundamental amino acids in kinase-ATP recognition and phosphorylation activity. L472 was identified as the gk+3 residue and was therefore considered as central in the ATP-binding site of NIK. More details about the hinge region of NIK are reported further in this chapter.

1.3 Validation and critics of the model

1.3.1. *Ramachandran plot*

Ramachandran developed a plotting approach to summarise φ and ψ values of every amino acid residues in the protein structure (Figure 15).[109]

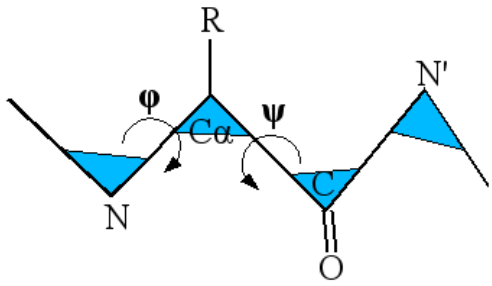

Figure 15: φ and ψ dihedral angles of amino acid residues in the protein structure (where R is the side chain)

The plot shows the possible conformations of φ and ψ angles for the polypeptide main chain (Figure 16). In the reported plot, red areas represent the most favourable angles values:

- area A represents angles corresponding to an α–helix;
- area B represents angles corresponding to a β–sheet;
- area L represents angles corresponding to left-handed helix.

Yellow, beige, and white areas represent additionally authorised, generously authorised and forbidden values for torsion angle respectively (Figure 16). Ramachandran plot of the model of NIK proved to be very satisfactory with 90.2% residues located in the most favoured regions, 7.3% in the allowed regions, only four residues (1.6%) in the generously allowed regions (φ and ψ torsion angles slightly larger than usual) and two residues in the disallowed regions (unfavourable φ and ψ torsion angles). It must be noticed that these six residues (Q484, T401,

Y391, E395, D544 and S572) are located far from the active site and the hinge region. The torsion angles distribution is summarised in table 2.

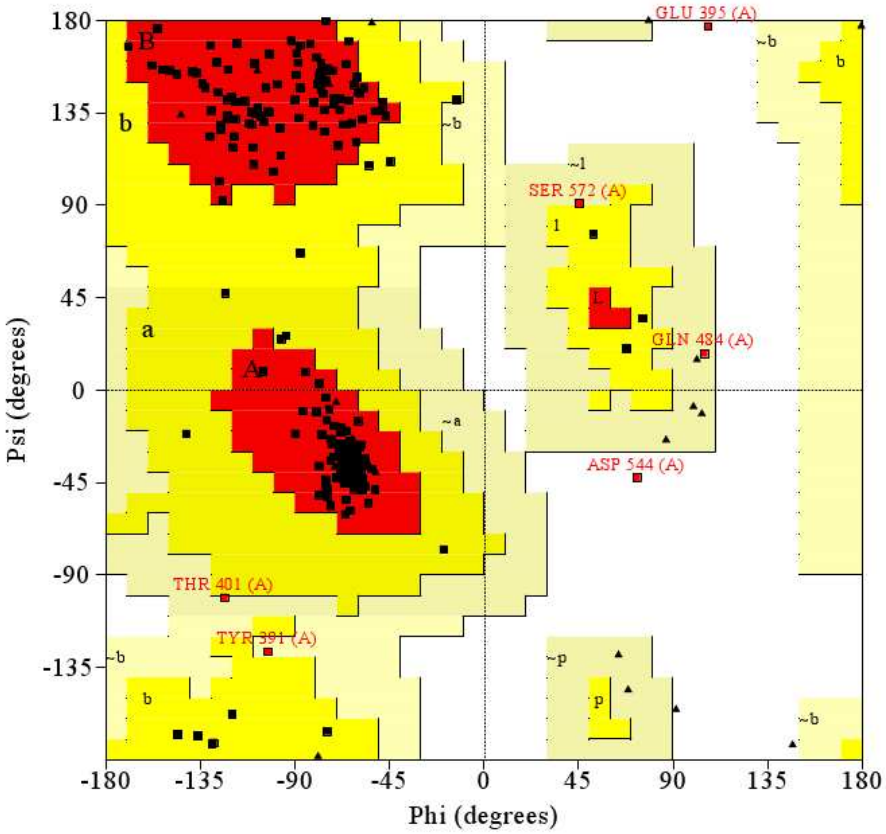

Figure 16: Ramachandran plot of the model of NIK

Table 2: Summary of the Ramachandran plot distribution

Color	Area	Residues	Residue %
red	most favourable	221	90.2%
yellow	additionally authorised	18	7.3%
beige	generously authorised	4	1.6%
white	forbidden	2	0.8%

This Ramachandran plot is the first validation of our newly developed homology model.

1.3.2. *K430 orientation*

Once the model was built, the residues reported as essentials for the kinase activity of NIK were analysed in a second validation study. Literature reports that the double mutant KK429-430AA of NIK is inactive.[77] Nevertheless, an interaction between K430 and ATP (or any ligand in this pocket) was unfavourable. In the proposed model, the side-chain of K430 points out of the cavity (Figure 17). Conversely, K429 is oriented to the pocket. This is in agreement with the previously published result (Figure 17). To confirm these positions, and as these mutations have always been studied simultaneously,[77] the design of the single mutants K429A and K430A would be very helpful. By this way, the specific role of each lysine could be clarified. If K430 is not essential for the kinase activity (or if the activity of the K430A mutant is preserved in comparison to NIK wild type), the orientation of this side chain will be validated in the model of NIK. These results will be reported further (section II.2).

Finally, T559 is located on the C-terminus side of the cavity at the end of the activation loop. The orientation of its side-chain allows a phosphate transfer on its hydroxyl function (Figure 17).

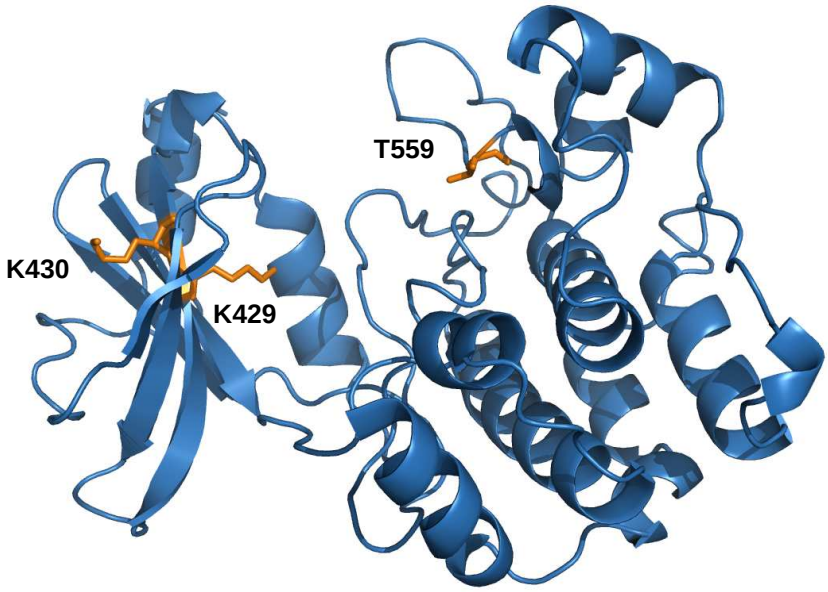

Figure 17: Model of NIK with residues KK430-429 and T559 (from left to right and underlined in orange)

1.3.3 *Identification of the key residues of NIK*

The 3D-structures of the kinase domains of NIK and PAK1 were then superimposed. As expected, the overall folding pattern (β-sheets, α-helixes and main loops) was shown to be logically preserved (Figure 18). The ATP-binding sites superimposition was analysed and the active site residues common to majority of kinases were recognised.

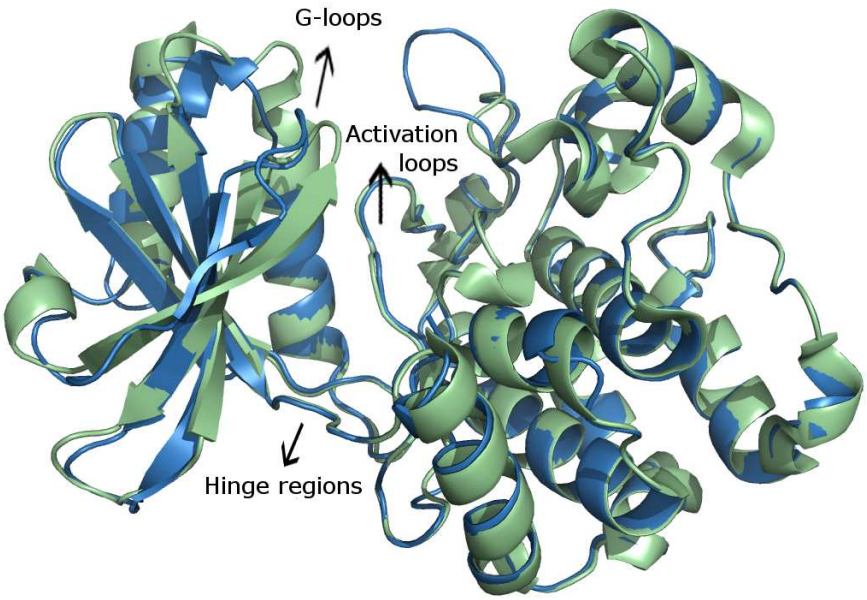

Figure 18: General view of the superimposition of PAK1 (green) and NIK (blue)

First, in the NIK structure, M469, which corresponds to M344 in PAK1, was identified as the gatekeeper (gk) residue. Then, residues E470 (gk+1) and L472 (gk+3) were logically located in the hinge region. As explained in the introduction, gk+1 and gk+3 residues are responsible for the stabilisation of the adenine moiety of the ATP. In PAK1, hinge residues gk+1 and gk+3 correspond to E345 and L347 respectively. In a co-crystal structure where 3-hydroxystaurosporine is soaked into PAK1 (PDB code: 2HY8), both residues are involved in the stabilisation of the aromatic ring of 3-hydroxystaurosporine (Figure 19). This observation assumes the key role of this region in the ATP-binding site, as explained previously. Finally, in the back of the NIK active site cavity, a salt bridge between residues K429 and E440, corresponding to the salt bridge between R299 and E315 in PAK1, is also preserved (Figure 20).

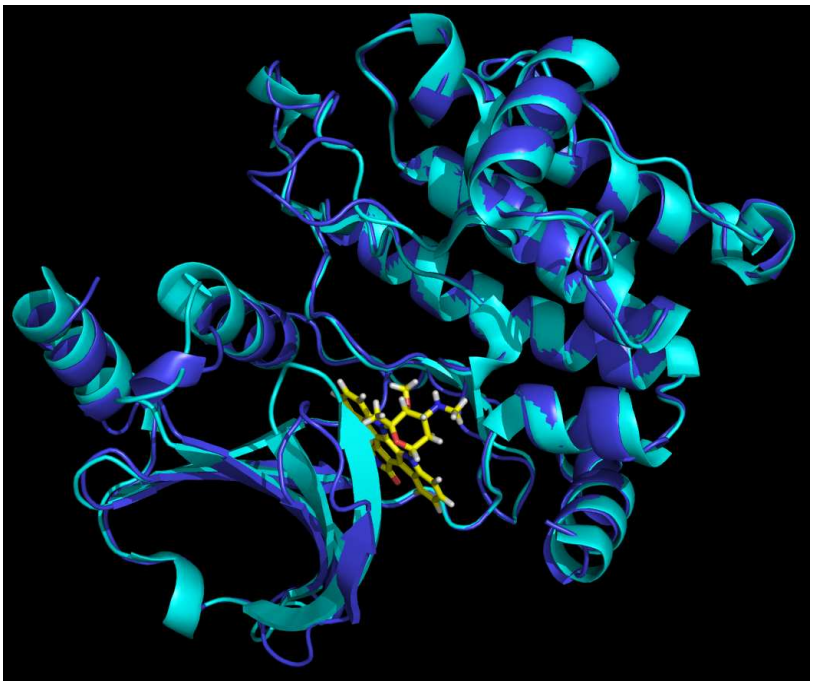

Figure 19: Superimposition of NIK and PAK1 with co-crystallised 3-hydroxystaurosporine

Close to this ionic interaction, the highly conserved triplet DFG of the activation loop is found in the model of NIK from residue 534 to 536 (Figure 20). This loop is very well overlaid on the template structure, and the triplet corresponds exactly to residues from D407 to G409 in PAK1.

Finally, the G-loop of PAK1 contains the amino acids 277 to 282 with the sequence GQGASG. In this loop, the residues G277, Q278 and G279 belong to the β-sheet preceding the flexible loop. This G-loop, linking the anti-parallel β-sheets, is then shortened. This observation explains why this region is not perfectly superimposed to the model of NIK. In fact, none of the residues from 407 to 412 belonging to NIK are included into any β-sheet in the model. Then, these residues form a longer and more flexible loop than in PAK1.

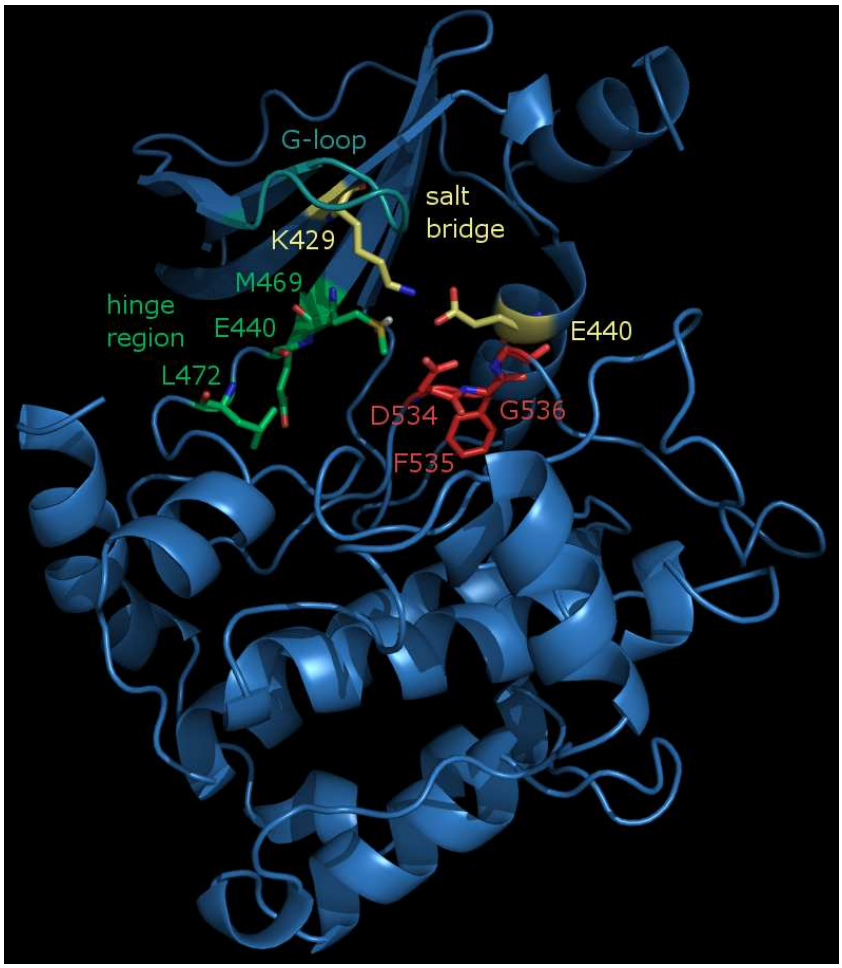

Figure 20: Main residues identified in the ATP-binding site of NIK

Each key residue of the ATP-binding site is reported in table 3:

Table 3 : Main residues of the ATP-binding site of NIK and PAK1

Region	**PAK1**	**NIK**
gatekeeper	M344	M469
hinge region	E345 and L347	E470 and L472
salt bridge	R299 and E315	K429 and E440
activation loop triad	407-DFG-409	534-DFG-536
G-loop	277-GQGASG-282	407-GRGSFG-412

In conclusion, a 3D-model of NIK was build, validated and studied with a rational approach.[110] This tool is now available to reach various goals. In a first step, the kinase domain of NIK will be investigated deeper with the help of a mutagenesis study. Then, various docking studies and virtual screening will be performed with this model in order to understand the required interactions for NIK inhibition and to identify new scaffolds.

2. Mutagenesis

To study into detail the kinase domain of NIK, the activity of various single mutants was considered. This study is directly derived from the molecular modelling. In this second step, the model of NIK can be validated or improved, residues interacting with ATP will be acknowledged and key regions for NIK inhibition will be identified. This study started with the selection of residues to be mutated.

2.1 Selection of key amino acid residues

To select the most interesting residues from the ATP-binding site of NIK, three filters were applied on the 253 residues kinase domain of NIK (Figure 21) as following: (i) a sequence alignment imitating the natural selection, (ii) an elimination based on the nature of the side chain, and (iii) an evaluation of the 3D situation.

```
405 RLGRGSFGEVHRMEDKQTGFQCAVKKVRLEVFRAEELMACAGLTSPRIVPLYGAVREGPW 464
465 VNIFMELLEGGSLGQLVKEQGCLPEDRALYYLGQALEGLEYLHSRRILHGDVKADNVLLS 524
525 SDGSHAALCDFGHAVCLQPDGLGKSLLTGDYIPGTETHMAPEVVLGRSCDAKVDVWSSCC 584
580 MMLHMLNGCHPWTQFFRGPLCLKIASEPPPVREIPPSCAPLTAQAIQEGLRKEPIHRVSA 644
645 AEL 647
```

Figure 21: Kinase domain sequence of NIK (residues from 405 to 647)

First step - This first filter, similar to a natural selection, was applied as following: an alignment of the kinase domain sequence of NIK was performed with the ten closest homologous proteins kinases reported in the literature so far (September 2007) by means of *BLASTP*.[104] Every biological species were taken together and the considered sequences shared until 32% of homology with the sequence of NIK. Then, each residue of NIK not

found each alignment was eliminated. Amino acids recovered in each sequences and selected are reported in figure 22:

```
405 RLG.GSFGEV...ED..T....A.K.V.L..F...EL...A......I..LYG.V..GP. 464
465 V.I.ME..E...L.Q.V.....L.E...L......L..LEYL..R.ILH..V...NVL.. 524
525 .......L.DFG.A..L...G............GTE.HMAPEV........K.DVWS..C 584
585 ..LHM..G..PW.Q.F.....L.I..E.PPV.EI...C.....Q..Q..L.K.P..R..A 644
645 .EL 647
```

Figure 22: Remaining residues after the first selection (natural selection)

Second step - Then, the aliphatic residues were removed (G, A, V, L, and I). Side chains of such amino acids contribute to the structure, but gives weak interactions (<0.7 kcal/mole) with ligands in comparison to residues forming H-bond (<6 kcal/mole) or ionic interactions (<10 kcal/mol). After this second filtration, 53 residues were remaining (Figure 23):

```
405 R....SF.E....ED..T......K......F...E..............Y.....GP. 464
465 ....ME..E.....Q.........E.............EY...R...H......N.... 524
525 .........DF.......................TE.HM.PE.........K.D.WS..C 584
585 ...HM.....PW.Q.F..........E.PP..E....C.....Q..Q....K.P..R... 644
645 .E. 647
```

Figure 23: Remaining residues after the second filtration step (aliphatic side chains)

Third step - The previously described model of NIK finally stepped in as the third filter. In this final selection, each of the 53 remaining residues was located into the 3D structure. By doing so, residues out of the ATP-binding site were discarded. Only 9 of the 253 initial amino acids remained as potential points of mutations (Figure 24):

```
405 ......F.................K......F...E..................... 464
465 ..........................................................  524
525 .........DF.....................TE.H.....................  584
585 ..........................................................  644
645 ... 647
```

Figure 24: Remaining residues after the third filtration step (3D location)

Interestingly, T559, the phosphorylation site, and K429, forming the salt bridge with E440, are recovered in this selection. D534 and F535, forming the highly conserved DFG triplet, were selected as well. In return, K430 was eliminated in the first phase. As explained below, the involvement of this lysine in the mechanism of the phosphate transfer remains unclear. K430A was then evaluated anyway with the eight following single mutants: K429A, D534A, F535A , F411A, F436A, H562A, E440A and E560A.

2.2 Site directed mutations

The study of the NF-κB alternative activation pathway and the protein NIK is the result of a fruitful collaboration with the laboratory of Virology and Immunology (GIGA, University of Liège). Each single mutant and measurement of its residual activity was entirely performed by this team. The selected residues were then mutated one by one and the mutants were evaluated for their ability to induce the alternative pathway. Each selected residue was changed to alanine by site-directed mutagenesis from an expression vector encoding wild-type NIK. The ability of each mutant to activate the NF-κB alternative pathway was evaluated by transient transfection assays in HEK293T cells (human embryonic kidney 293T cells). High expression of NIK induced a constitutive p100 processing in the

alternative pathway (see Introduction, Figure 4). Cells were then lysed 40 hours after transfection and the processing of p100 into p52 was analysed by Western-blot.[111] Any loss of ability to activate this cascade would be detected by an increase of p100 concentration and a decrease of p52 concentration when compared to the processing induced by NIK wild type (wt, Figure 25).

First, K430A undoubtedly induces the processing of p100 into p52 (Figure 25). This mutation does not affect the ability of NIK to induce the alternative pathway. Therefore, K430 is not fundamental for the kinase activity of NIK and the orientation of its side-chain outside the cavity is confirmed. Conversely, the mutation K429A was unable to induce the same processing. It was consequently demonstrated that K429 is the unique lysine interacting with ATP during the phosphate transfer. Moreover, this result is completely in agreement with the proposed model of NIK.

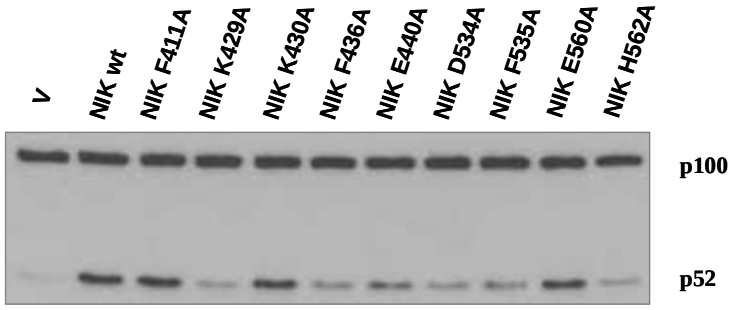

Figure 25: NIK activity of each single mutant was measured by western-blotting subunits p100 and p52 (v = blank ; wt = wild type)

As previously suggested, the ammonium of K429 is forming an ionic interaction with the carbonate side chain of E440, in the model of NIK. The mutant E440A prevents also the processing of p100, indicating the major

part of this salt bridge into the kinase mechanism (Figure 25). This result also confirms the proposed 3D model of NIK.

The D534A mutant displays an important activity defeat. Belonging to the activation loop motif DFG, this aspartate is most probably involved in the phosphate transfer. Similarly, the F535A mutation affecting the DFG triad strongly reduces the processing of p100 into p52. This result indicates a significant inhibition of NIK as well (Figure 25).

On the C-terminus side of NIK, H562 is a residue close to the phosphorylation site T559. The H562A mutant was also unable to induce the alternative pathway activation (Figure 25). This result can be explained by the vicinity of this histidine and T559. The imidazole scaffold of H562 is therefore expected to stabilise the transferred phosphate or the phosphorylated threonine.

Then, F436, located just above the ATP-binding site and the salt bridge formed by K429 and E440, seems also to play a decisive role in the activity of NIK since the mutant F436A does not induce the p100/p52 processing (Figure 25). This result can be explained by the localisation of F436 on top of the specificity pocket, a central point of the ATP-binding site.

Finally, no variation of activity is observed with mutations F411A and E560A, indicating these residues are less important for the kinase activity (Figure 25). This information is interesting in the frame of a better understanding of NIK's mechanism. In fact, F411 could be suspected as a key residue for NIK as it belongs to the G-loop located on the roof of the enzymatic pocket. Equally, E560, which is just nearby the phosphorylation site T559, could also be involved in the phosphate transfer. These experiments proved that it is not the case.

In conclusion, the mutagenesis results show that six of nine selected residues play a critical role into NIK activity: F436, E440, D534, F535, H562 and obviously K429.[112] So, the filtration strategy seems clearly relevant, as well as the model of NIK which proved to be reliable. This mutagenesis study validates the 3D-structure of NIK built by homology modelling. This model will be considered as the starting point for the molecular docking and virtual screening detailed further.

3. Docking

To appraise the reliability of our model, the binding of the previously reported pyrazolo[4,3-*c*]isoquinolines claimed as NIK inhibitors was studied within the active site. Staurosporine, reported as a pankinase inhibitor including NIK,[113] was also investigated in our model. Pyrazolo[4,3-*c*]isoquinolines **5a-s** and staurosporine (Table 4) were docked inside the ATP-binding site of NIK using the automated *GOLD* program.[114] For each molecule, 20 conformations were generated and evaluated following two parameters:

1. the number of different orientations (NDO) adopted by one molecule inside the NIK binding cleft;
2. the number of different orientations where the compound is found to be stabilised with at least one H-bond with the residue L472 in the hinge region (NDO L472).

As explained in the introduction, the hinge residues gk+1 and gk+3 develop key interactions with adenine from ATP in the kinase pocket. The backbone of this region is clearly identified as the highest common region targeted by each ATP-competitive inhibitor. More precisely, the NH of gk+3, the central H-bond donor of the hinge region, is stabilising each known ATP-competitive kinase inhibitor. That is the reason why this residue was selected to study the ligand interactions.

Table 4: Structure and number of conformations adopted by pyrazolo[4,3-*c*]isoquinolines **5a-s**. **NDO** is the number of different orientations observed after 20 dockings for 1 molecule; **NDO L472** is the number of different orientations observed with an H-bond interaction with residue L472

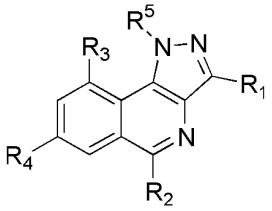

pyrazolo[4,3-*c*]isoquinolines **5**

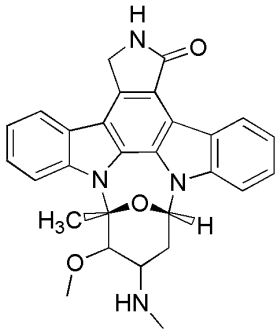

staurosporine

Cpd	R_1	R_2	R_3	R_4	R_5	Docking	
						NDO	NDO L472
Staurosporine						1	1
5a	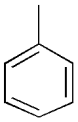	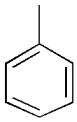	H	H	H	4	1
5b	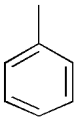	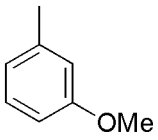	H	H	H	6	2
5c	Me	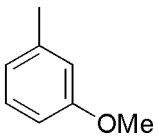	H	H	H	2	0
5d	Me	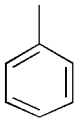	H	H	H	2	0
5e	Me	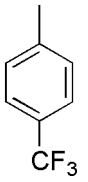	H	H	H	3	0

Cpd	R_1	R_2	R_3	R_4	R_5	Docking	
						NDO	NDO L472
5f	Me	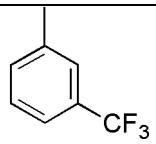	H	H	Me	1	0
5g	CF_3	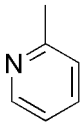	H	H	H	2	0
5h	Me	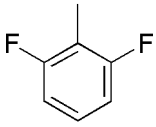	H	H	Me	2	1
5i	Me	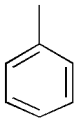	H	CO_2Me	H	4	2
5j	Me	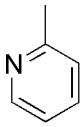	H	CO_2Me	H	3	2
5k	Me	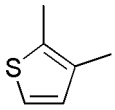	H	H	Me	3	0
5l	Me	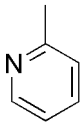	H	NMe_2	H	2	0
5m	Me	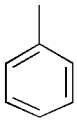	CF_3	H	H	2	1
5n	Me	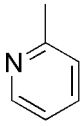	CF_3	H	H	4	2

Cpd	R_1	R_2	R_3	R_4	R_5	Docking	
						NDO	NDO L472
5o	Me	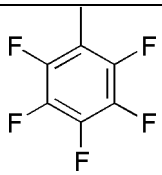	H	H	H	4	1
5p	Me	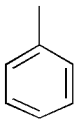	H	NMe_2	H	3	2
5q	Me	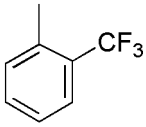	H	H	H	4	1
5r	Me	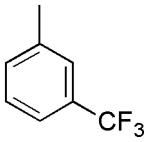	H	H	H	1	0
5s	Me	CH_2OMe	H	H	H	5	1

Interestingly, the staurosporine moiety fits perfectly the catalytic pocket of NIK (Figure 26), adopting a similar binding orientation as observed for 3-OH-staurosporine in PAK1 (Figure 19).

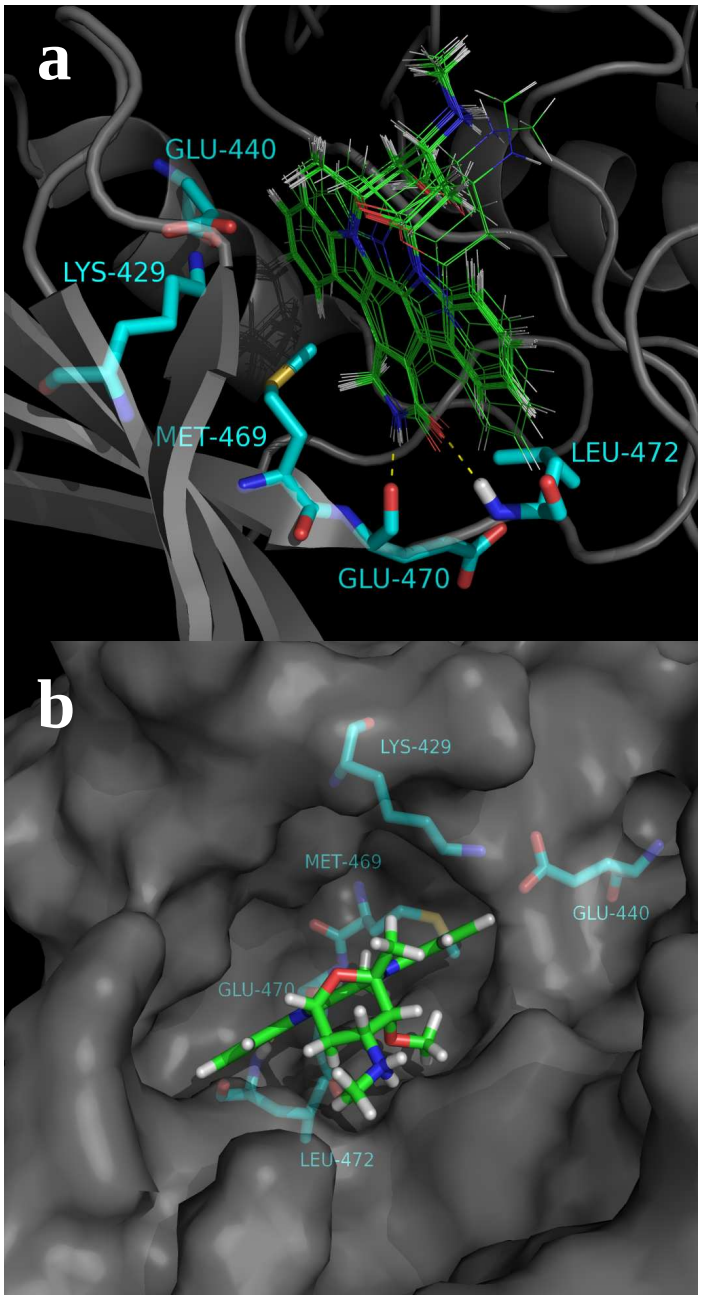

Figure 26: (a) All of the 20 conformations obtained for staurosporine into the modelled active site cavity of NIK and (b) view of staurosporine in the active site cavity NIK illustrated with the Connolly surface.

All of the 20 conformations generated lie in a unique orientation with two H-bonds between the lactam ring of staurosporine and the NH and CO moieties of L472 and E470, respectively, stabilising the ligand (Figure 26). In addition, hydrophobic interactions with aliphatic residues L406, V414, A427, L522 and C533 also contribute to the stabilisation on both sides of the aromatic plane. Conversely, when pyrazolo[4,3-*c*]isoquinolines **5a-s** are docked inside the ATP-binding site of NIK, several different orientations (2 to 6) are observed for each compound (Table 4), except **5f** and **5r** for which a unique binding orientation of the pyrazolo[4,3-*c*]isoquinoline motif is found. But these two compounds do not interact with L472 through an H-bound as requested. In addition, other pyrazolo[4,3-*c*]isoquinolines (**5c-5e, 5g, 5k, 5l**) are not stabilised through H-bond interaction with the hinge region residue L472.

To see if a unique orientation of the pyrazolo[4,3-*c*]isoquinoline series **5** could be highlighted, another docking was considered. In this new study, compounds **5a-s** were docked again inside the NIK binding cleft imposing a H-bond between the NH of L472 and one acceptor atom of the ligand. By doing so, still two orientations were found, and are illustrated using compound **5d** (Figure 27 for orientation 1, and figure 28 for orientation 2). In both orientations, the pyrazolo[4,3-*c*]isoquinoline scaffold is stabilised by two H-bonds in the hinge region, as expected following a constraint docking. But none of these two orientations seems more plausible than the other, or would allow a better understanding of the structure-activity relationships in this series. Thus, this docking study does unfortunately not allow to highlight a unique, obvious orientation of compounds **5a-s** into the NIK binding cavity.

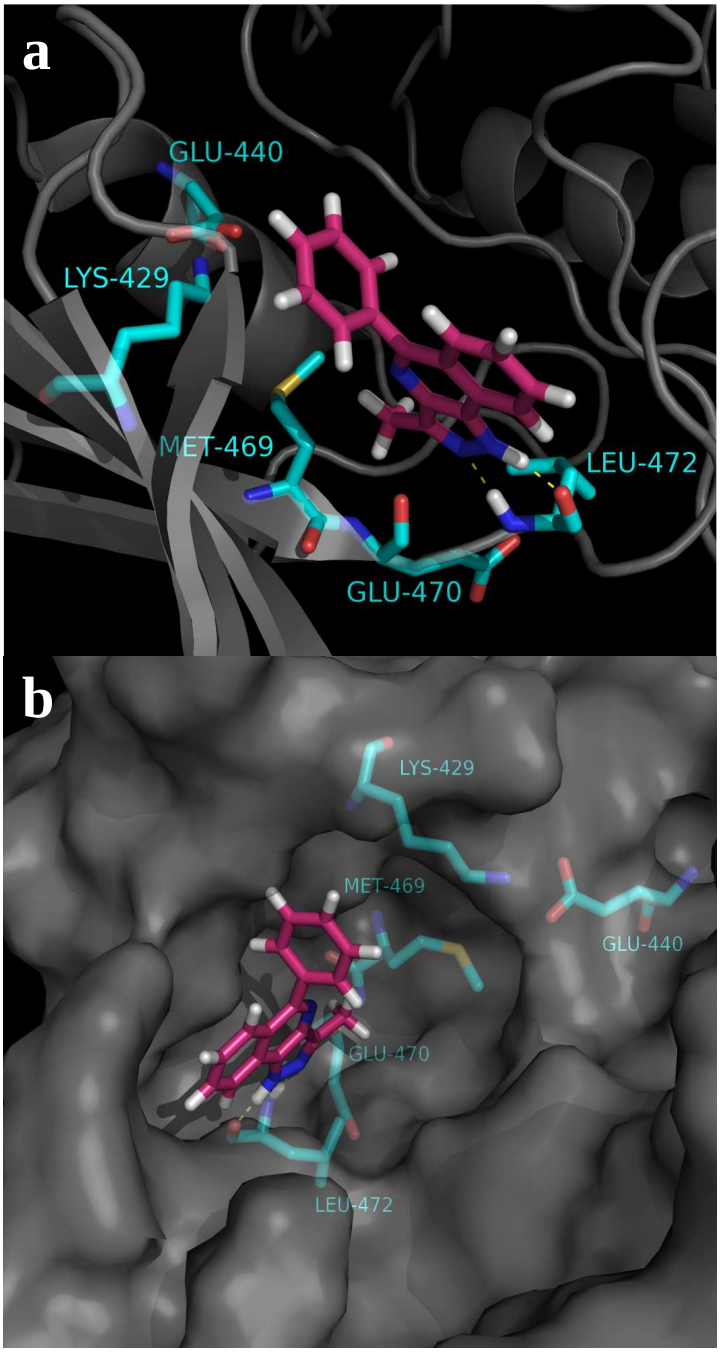

Figure 27: Orientation 1 of compound **5d** docked in the modelled ATP-binding site of NIK when imposing a H-bond between the NH of L472. View without (a) or with (b) Connolly surface.

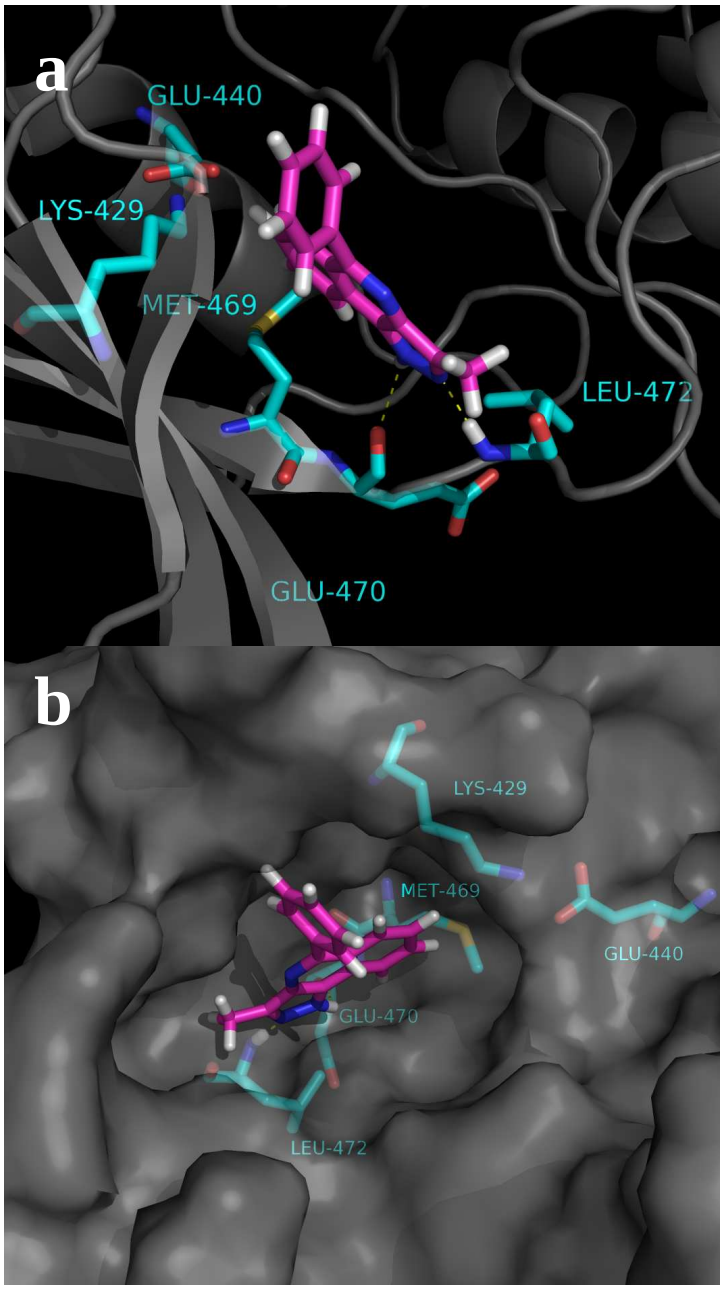

Figure 28: Orientation 2 of compound **5d** docked in the modelled ATP-binding site of NIK when imposing a H-bond between the NH of L472. View without (a) or with (b) Connolly surface.

These two docking studies led to the conclusion that no particular affinity can be predicted for the pyrazolo[4,3-*c*]isoquinoline series.[110] Actually, since this molecular template was claimed as potent and selective inhibitors of NIK,[102,103] a main and obvious docking mode was expected. On the contrary, neither affinity or relationship activity can be explained, even when a H-bond is imposed between the ligand and the key residure L472. Based on these observations, different hypothesis could be suggested:

1. although staurosporine, a confirmed NIK inhibitor, fits perfectly its active site, the 3D-model of NIK is not reliable;

2. the pyrazolo[4,3-*c*]isoquinolines **5a-s** are effectively NIK inhibitors but through a different mechanism of inhibition, for instance through interactions with an allosteric site;

3. the pyrazolo[4,3-*c*]isoquinolines **5a-s** are not NIK inhibitors.

To assess one of these assumptions, some pyrazolo[4,3-*c*]isoquinolines (**5a-d**) and analogous pyrazolo[3,4-*c*]isoquinolines were synthesised simultaneously with this docking study. Their NIK inhibitory potency was evaluated on isolated human recombinant enzyme as well as on Hela cells where the NF-κB alternative pathway was induced.

4. Organic synthesis and commercial compounds

In parallel to the docking study, pyrazolo[4,3-*c*]isoquinolines, plus some molecular analogs, were synthesised to evaluate their effective inhibition potency against NIK. Also, the purchase of commercially available molecules is reported. Finally, all of these molecules were assayed on the enzyme NIK to evaluate their inhibitory potency.

4.1 Synthesis of pyrazolo[4,3-*c*]isoquinoline

The pyrazolo[4,3-*c*]isoquinolines **5a-d** are synthesised in four steps (Scheme 1).

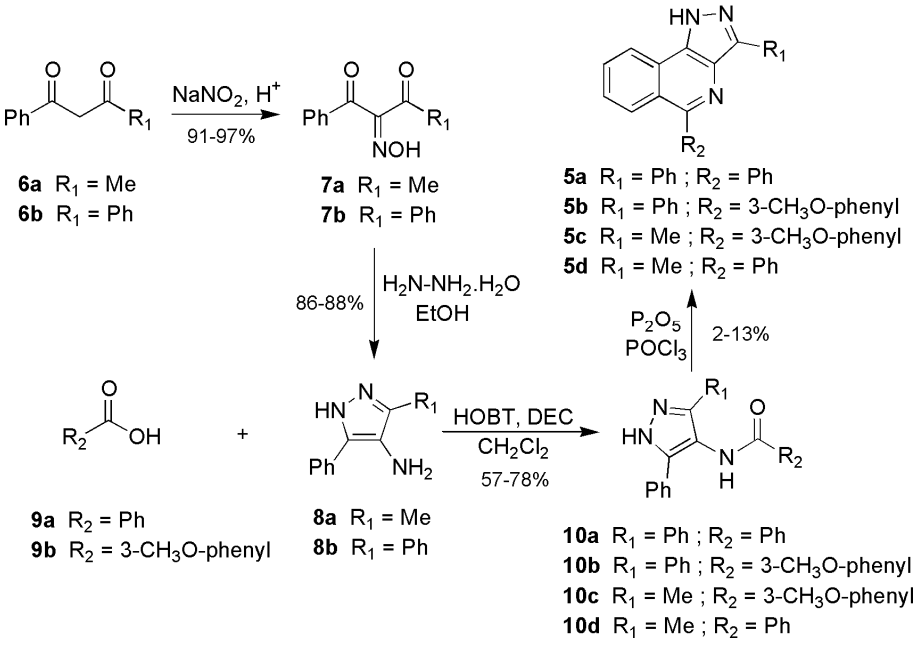

Scheme 1: Synthesis of pyrazolo[4,3-*c*]isoquinolines

Starting from the commercially available diketones **6a-b**, oximes **7a-b** are prepared with a high yield (91-97%) by reaction of sodium nitrite in

acidic conditions.[115] Oximes **7a-b** further react with hydrazine hydrate to form pyrazoles **8a-b**.[116] Then, benzoic acids **9a-b** activated by HOBT/DEC are condensed on pyrazoles **8a-b** to form the corresponding amides **10a-d**. Finally, the desired pyrazolo[4,3-*c*]isoquinolines **5a-d** (Table 5) are obtained according to the Pictet-Gams reaction in poor yields (2-13%).[117] Chemical yield of this last step is very low due to the formation of several side products and a delicate purification (Scheme 1).

4.2 Pyrazolo[3,4-*c*]isoquinolines synthesis

As poor yields and difficult purification were curbing the pyrazolo[4,3-*c*]isoquinolines synthesis, an analogous scaffold has been considered. By choosing more reachable molecules, a largest series can be synthesised, leading to more interesting potential structure-activity relationships. In the meantime, this new series is a way to step out of the Aventis patent. For all those reasons, the pyrazolo[3,4-*c*]isoquinoline scaffold was chosen. This molecular structure, very close to pyrazolo[4,3-*c*]isoquinolines was previously patented by Exelixis as ALK (anaplastic lymphoma kinase) inhibitors.[118] Pyrazolo[3,4-*c*]isoquinolines **11a-l** are then synthesised in three steps, each of it being an opportunity to introduce new structural variations at the R_6, R_7 and R_8 positions (Scheme 2).

The esters **13a-c** and benzylcyanide **12** react in basic conditions to form the nitrile derivatives **14a-c** with various R_6 substituents. These nitriles react further with R_7-substituted hydrazines to form the aminopyrazoles **15a-h**. Finally, the benzoyl derivatives **16a-c** react with the aminopyrazoles **15a-h** in acidic conditions to form the required pyrazolo[3,4-*c*]isoquinolines **11a-l** with a wide range of yield (1-60%).

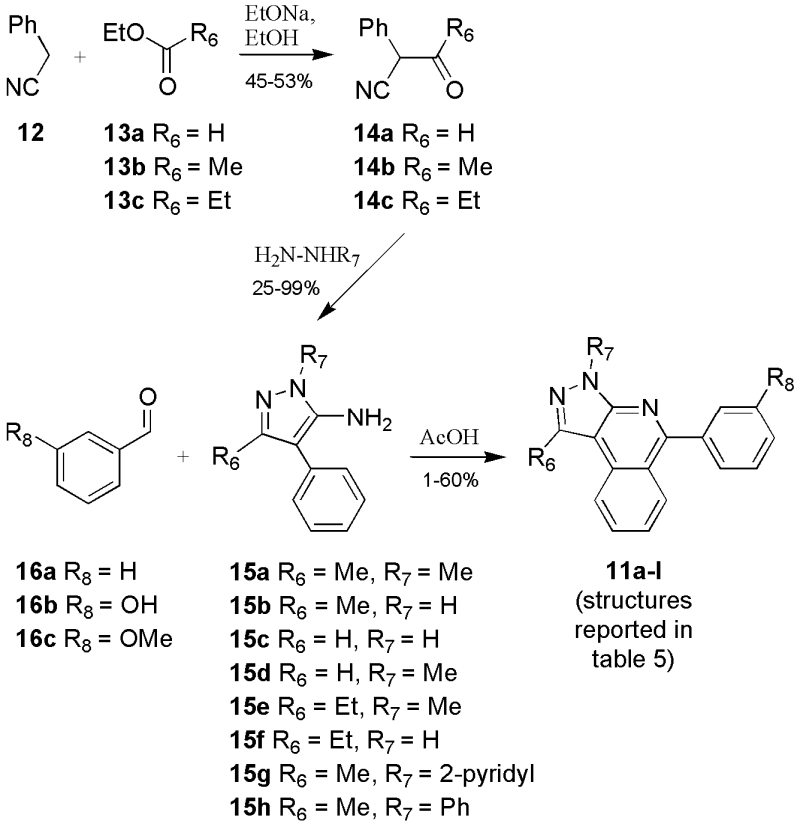

Scheme 2: Synthesis of pyrazolo[3,4-*c*]isoquinolines.

In comparison to the synthesis of pyrazolo[4,3-*c*]isoquinolines, the cyclisation step generating pyrazolo[3,4-*c*]isoquinolines is a cleaner process which does not involve the same purification issues.

Thirteen pyrazolo[3,4-*c*]isoquinolines were synthesised following this pathway (Table 5).

Table 5: Synthesised pyrazolo[3,4-*c*]isoquinolines structures

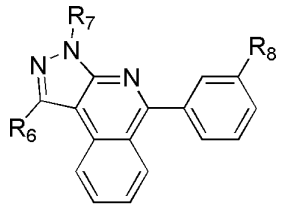

11a-l

Compound	**R_6**	**R_7**	**R_8**
11a	Me	Me	H
11b	Me	H	H
11c	H	H	H
11d	Me	Me	OH
11e	H	Me	H
11f	Me	H	OH
11g	H	H	OH
11h	Et	Me	H
11i	Et	H	H
11j	Me	H	OMe
11k	Me	2-pyridinyl	H
11l	Me	Ph	H

4.3 Commercial compounds

Finally, a panel of commercially available kinase inhibitors or molecules closely related to the structure of pyrazolo[4,3-c]isoquinolines was selected.

4.3.1 *Fragments of pyrazolo[4,3-c]isoquinolines*

To identify other pyrazoloisoquinolines as potential NIK inhibitors and with a view to develop SAR in this series, the pyrazolo[4,3-*c*]isoquinolines scaffold was searched for into the ZINC database.[119]

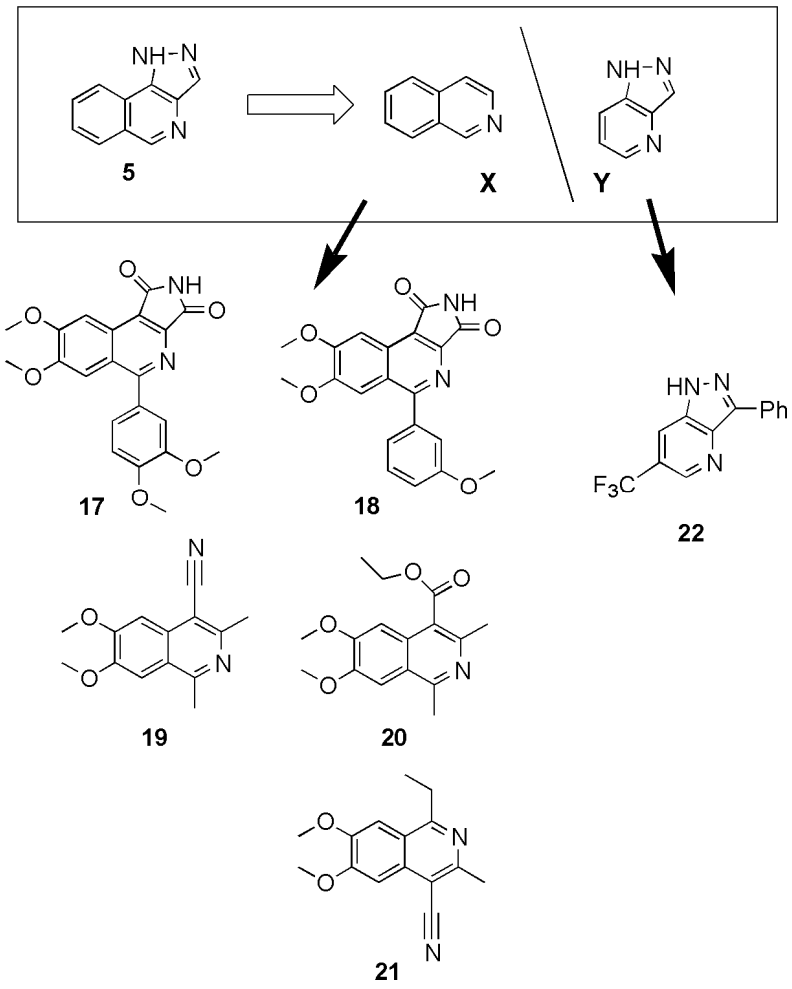

Figure 29: Commercial molecules structurally related to the molecular template **5**

On 2,700,000 commercially available compounds, no pyrazolo[4,3-*c*]iso-quinolines was regained in the database. Then the scaffold was splitted into pyrazolopyridine (**Y**) and isoquinoline (**X**) as starting structures to identify structurally related molecules. The compounds **17** to **22** were identified as commercially available and bought (Figure 29).

4.3.2 *Kinase inhibitors*

Another strategy to identify potential and novel NIK inhibitors was to search for molecules described as inhibitors of kinases structurally related to NIK. As mentioned previously, NIK belongs to the MAP kinase family. Considering this approach, the following compounds were investigated (Figure 30):

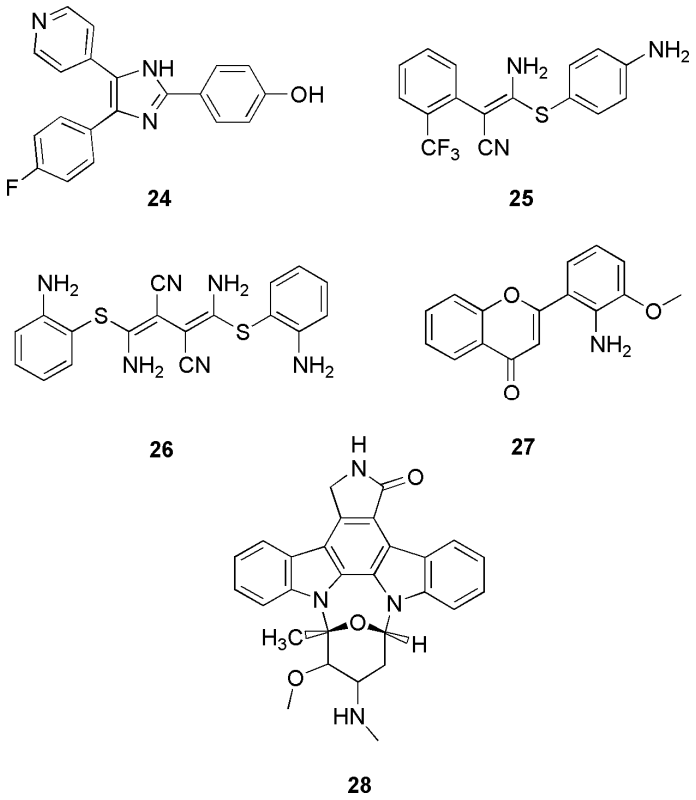

Figure 30: Commercial molecules reported as kinase inhibitors in the literature.

Compound **24** is a selective p38 MAP kinase inhibitor with an ATP-competitive mechanism.[99,120] Compounds **25**, **26** and **27** are MEK inhibitors,[121-126] and staurosporine **28** is a multi-kinase inhibitor previously mentioned in the molecular modelling and docking studies.[113,127] This molecule is the reference inhibitor for each enzymatic and cellular assay.

At this point, we own a diversified collection of chemical compounds formed by pyrazolo[4,3-*c*]isoquinolines **5a-d** claimed in a patent as NIK inhibitors,[110] analogous pyrazolo[3,4-*c*]isoquinolines **11a-l**, fragments like pyrazolopyridine **Y** or isoquinolines **X**, and inhibitors of kinases described in the literature as active on kinase structurally close to NIK. A biological evaluation of all these molecules is now considered and the results are reported in the following section.

5. Biological evaluation

5.1 Human recombinant NIK inhibition

A radiometric protein kinase assay, performed by ProQinase GmbH, Freiburg, Germany, measured the activity of NIK in presence of the potential inhibitors, at a single concentration of 10 µM. Briefly, NIK was expressed in Sf9 insect cells as human recombinant GST-fusion protein and purified by affinity chromatography using GSH-agarose. The substrate, a recombinant protein kinase (RBER-CHKtide) was expressed in *E.coli*. The assay cocktail was incubated at 30°C for 60 minutes with [γ-^{33}P]-ATP (1 µM, pH 7.5). Incorporation of ^{33}P was measured with a microplate scintillation counter. Staurosporine was chosen as reference.[113,127]

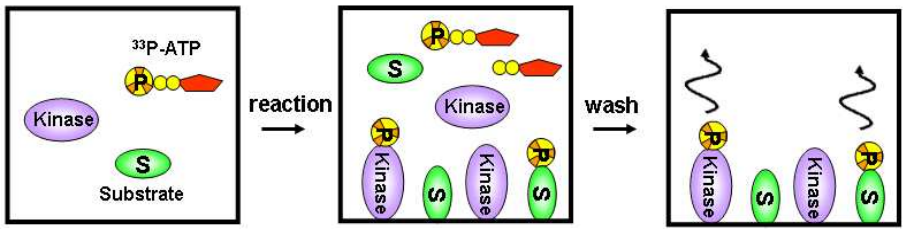

Figure 31: ProQinase *in vitro* enzymatic assay

Inhibitory potency of each previously described molecule was then evaluated (Table 6).

Table 6: Inhibition of NIK in presence of pyrazoloisoquinolines **5a-d** and **11a-l** (10µM). Mean + SD (n = 3).

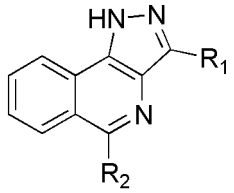

5

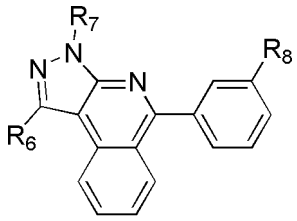

11

Molecule	R_1	R_2	R_6	R_7	R_8	NIK inhibition (10µM)
Staurosporine **28**						**72%**
5a	Ph	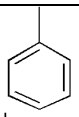	-	-	-	6%
5b	Ph	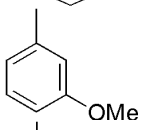	-	-	-	0%
5c	Me	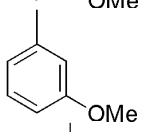	-	-	-	18%
5d	Me	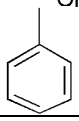	-	-	-	2%
11a	-	-	Me	Me	H	2%
11b	-	-	Me	H	H	0%
11c	-	-	H	H	H	4%
11d	-	-	Me	Me	OH	8%
11e	-	-	H	Me	H	2%
11f	-	-	Me	H	OH	0%
11g	-	-	H	H	OH	0%
11h	-	-	Et	Me	H	0%
11i	-	-	Et	H	H	0%
11j	-	-	Me	H	OMe	0%
11k	-	-	Me	2-pyridyl	H	9%
1ll	-	-	Me	Ph	H	0%

Although the inhibition of NIK in the presence of staurosporine was confirmed, none of the pyrazoloisoquinolines (10µM) significantly reduced the NIK activity (Table 6). This corroborates the modelling study and demonstrates that the pyrazolo[4,3-*c*]isoquinolines **5a-d** are not NIK inhibitors. Moreover, the pyrazolo[3,4-*c*]isoquinolines **11a-l** do not inhibit NIK. Except staurosporine **28**, none of the commercial molecules structurally close to pyrazolo[4,3-*c*]isoquinolines **17-22** or reported as kinase inhibitors **24-28** blocked the kinase activity of NIK.

At this point, the pyrazolo[4,3-*c*]isoquinoline scaffold patented by Aventis can not be considered as NIK inhibitor. To confirm this scaffold can not inhibit other proteins of the NF-κB alternative pathway, their inhibition property was then investigated in a cellular assay where this alternative pathway was solely involved.

5.2 NF-κB alternative pathway inhibition

The cellular assays regarding the alternative pathway were performed by Caroline Remouchamps and Corinne Ganeff under the supervision of Emmanuel Dejardin from the laboratory of Virology and Immunology (GIGA, University of Liège). Briefly, pyrazolo[4,3-*c*]isoquinolines **5a-d** were assayed using carcinoma Hela cells expressing LTβR. The NF-κB alternative pathway was induced or not by an LTβR agonist antibody. After induction, NIK was overexpressed and the processing of p100 into p52 was triggered by phosphorylation of IKKα (Figure 32). Then, the p100/p52 ratio was finally analysed by Western blot, as reported on figure 33.

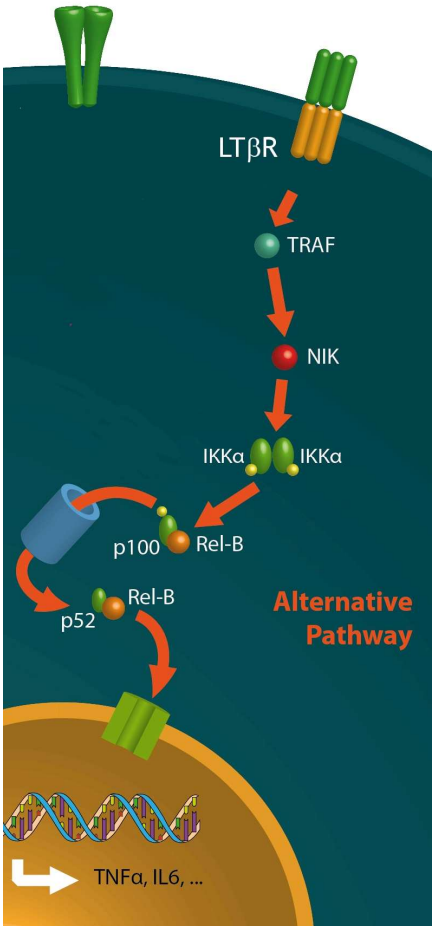

Figure 32: Alternative pathway activation assay

Staurosporine, which strongly inhibit isolated human recombinant NIK, also clearly blocks the p100/p52 processing (Figure 33). Here again, none of the pyrazolo[4,3-*c*]isoquinolines **5a-d** inhibited the NF-κB alternative pathway. In fact, the processing of p100 into p52 was observed in the presence (+) and in the absence (-) of **5a-d** whatever the concentration of the inhibitor (10, 20 or 50 µM). On the contrary to the claims of the original patent, the pyrazolo[4,3-*c*]isoquinolines **5a-d** cannot be considered neither as NIK inhibitor nor as blocker of the NF-κB alternative pathway.

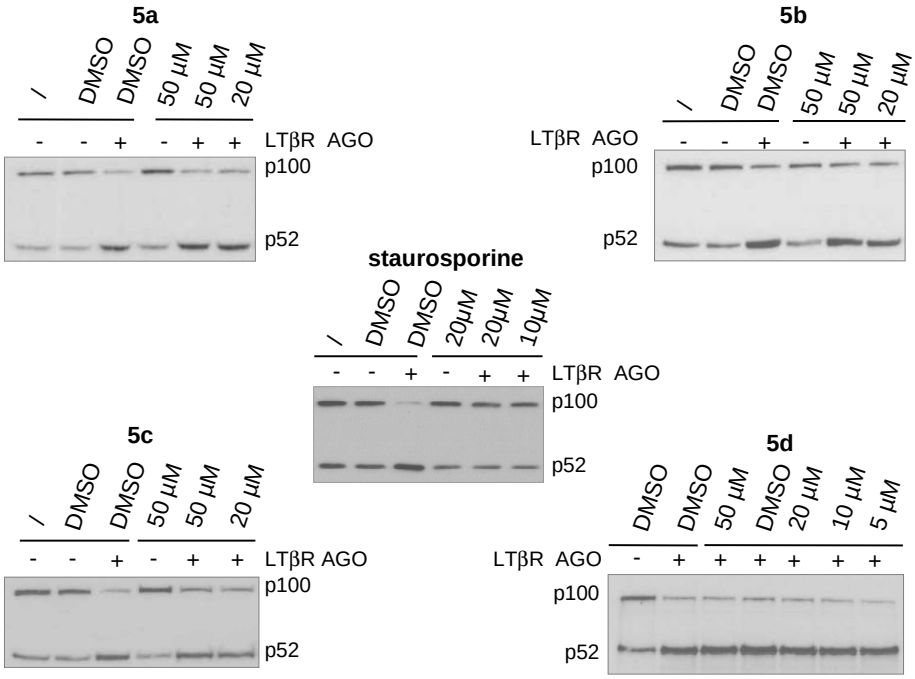

Figure 33: Processing of p100 into p52 from Hela cells expressing LTβR stimulated by an LTβR agonist antibody (AGO). Cells were incubated in absence or in presence of pyrazolo[4,3-*c*]isoquinolines **5a-d** or with staurosporine. DMSO used as cosolvent has no effect.

5.3 Multikinase Assay

With the aim of identifying the putative target of the pyrazolo[4,3-*c*]isoquinolines and pyrazolo[3,4-*c*]isoquinolines, a multikinase screening assay was performed. One compound of each series (**5d** and **11f**) was selected to carry out this study. Their inhibitory protency (10 µM) was evaluated on a panel of 263 kinases (Millipore KinaseProfiler™, Table of results in the Appendix).

As a result, the inhibition of at least 50% was observed for 92 and 98 kinases over the 263 assayed in presence of **5d** or **11f**, respectively. Both scaffolds are clearly good kinase inhibitor templates. However, no kinase groups or families seems to be more affected than others. Both pyrazolo-isoquinolines inhibit indiscriminately more than a third of our kinase panel. Nevertheless, among these, **5d** particularly decreased (70%) the activity of TAK1, a TGF-β–activated kinase involved in the classical NF-κB pathway (see Introduction, figure 4). To confirm this interesting result, an enzymatic assay on TAK1 was immediately performed with pyrazolo[4,3-*c*]isoquinolines **5a-d**.

5.4 TAK1 inhibition

The TAK1 dose-inhibitory potency of compounds **5a-d** was evaluated using a Lanthascreen® Eu Kinase Binding Assay (performed by Invitrogen Limited, Paisley, Scotland, United Kingdom). Briefly, this assay is based on the detection of the binding of a "tracer" to a kinase by addition of a Eu-labeled anti-tag antibody. The binding to a kinase of both tracer and antibody results in a high degree of FRET, whereas displacement of the tracer with a kinase inhibitor results in a loss of FRET (Figure 34). The results are reported in Table 7:

Table 7: IC_{50} of pyrazolo[4,3-*c*]isoquinolines **5a-d** against TAK1.

Cpd	TAK1 IC_{50} (μM)
staurosporine	0.021
5a	NI (at 10μM)
5b	NI (at 150μM)
5c	0.58
5d	2.1

NI = no inhibition at the reported maximum concentration

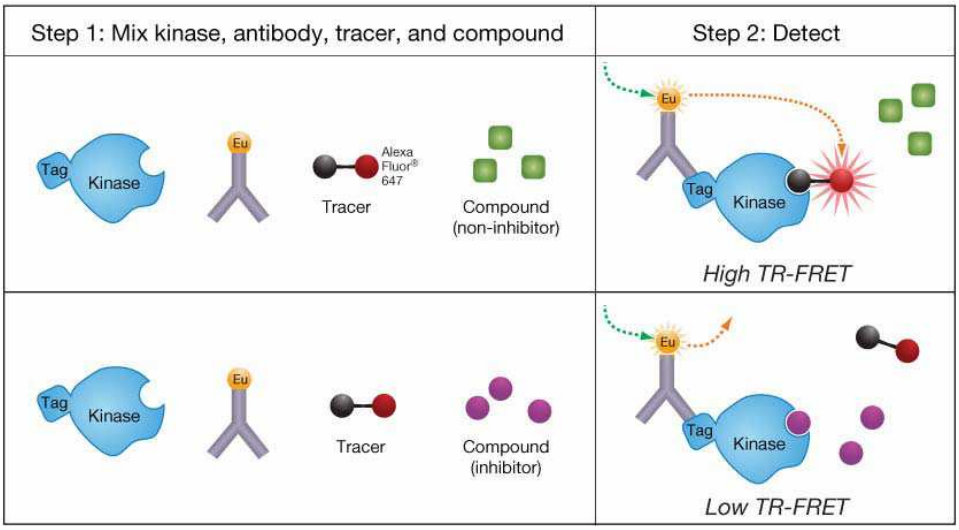

Figure 34: Schematic of LanthaScreenTM Eu Kinase Binding Assay

As expected, staurosporine **28**, the reference inhibitor in this assay, strongly inhibits TAK1 with an IC_{50} of 0.021 µM. From the four compounds analysed, **5c** and **5d**, effectively inhibit TAK1 with an IC_{50} value of 0.58 and 2.1 µM respectively, whereas no inhibition was observed at 10µM and 150µM for **5a** and **5b** respectively.

5.5 NF-κB classical pathway inhibition

To access the effective inhibition of TAK1 in the canonical activation pathway of NIK, a last assay was performed using Hela cells. Briefly, **5c** (50 µM), the best TAK1 inhibitor (IC_{50} = 0.58 µM), was assayed on carcinoma Hela cells where the NF-κB classical pathway was induced by TNFα (100 U/mL). As readout, the TNFα and IL-6 mRNA levels were quantified (in presence or in absence of **5c**) and normalised with respect to control conditions. As expected, TNFα doubles the relative TNFα mRNA-level 1 h (x2.2) and 2 h (x1.9) following induction, whereas the induction in

presence of **5c** is only x0.77 and x0.65 respectively (Figure 35). TNFα strongly increases the relative IL-6 mRNA-level 1 hour (x3.7) and 2 hours (x3.8) after induction. Conversely, the addition of **5c** prevents an increase of the normalised IL-6 mRNA-levels which are x0.5 and x0.7 when measured 1h and 2h after induction respectively.

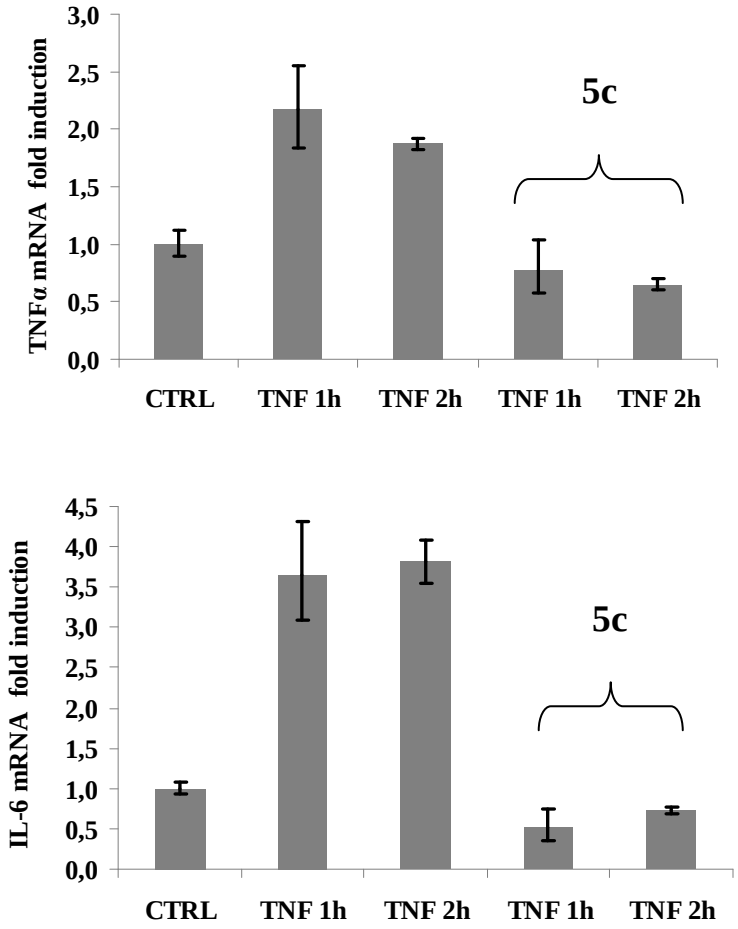

Figure 35: Normalised TNFα and IL-6 mRNA levels induced by TNFα (100 U/ml) in absence or in presence of TAK1 inhibitor **5c** (50 µM). Measurements were conducted 1h and 2h following TNFα addition. TNFα and IL-6 mRNA levels prior to TNFα addition (CTRL) are considered as 1. Mean ± sd.

5.6 Docking of pyrazolo[4,3-*c*]isoquinoline into TAK1

As the 3D-coordinates of TAK1 are available (PDB code 2EVA),[128] molecular interactions stabilising **5c** and **5d** inside the TAK1 cavity were analysed with a view to identify the structural elements required for their inhibitory potency. When **5c** or **5d** are docked inside the TAK1 binding cleft, all of the 20 conformations adopt a unique orientation corresponding to a deep insertion in the cavity of the pyrazolo[4,3-*c*]isoquinoline. The R_1-methyl points towards the entrance of the active site (Figure 36a). Both compounds are stabilised by:

1. two H-bonds with residues E105 and A107 in the hinge region;
2. hydrophobic interactions with residues V50, A61 and L163.

So, **5c** and **5d** fit perfectly the TAK1 ATP-binding site (Figure 36).

Interestingly, the inactivity of compounds **5a** and **5b** might be explained by a steric clash between the phenyl group in position R_1 of the pyrazolo[4,3-*c*]isoquinoline ring and the residue Y106 of TAK1 (Figure 36c).

Thus, this study highlights the molecular interactions of pyrazolo[4,3-*c*]isoquinolines **5c-d** with TAK1. When the R_1-methyl is replaced by bulkier group such as a phenyl (**5a-b**), the steric hindrance certainly prevents its binding to TAK1 and suppresses their inhibitory potency against this kinase.

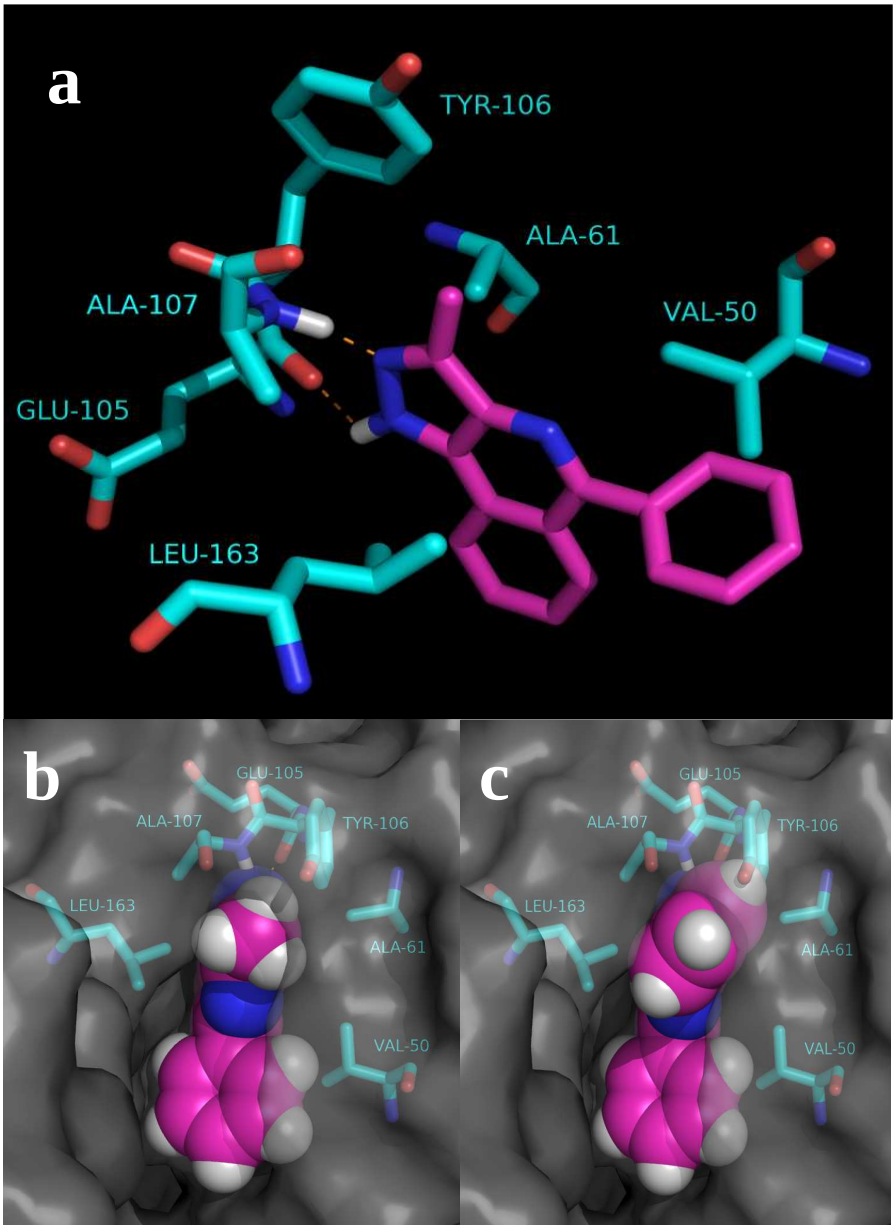

Figure 36: Molecular interactions between TAK1 and (a) **5d** (stick representation), (b) **5d** and (c) **5a** with sphere representation in the hinge region of TAK1. Pictures made using PYMOL.[129]

5.7 TAK1 inhibition as a perspective

In conclusion, a multikinase screen revealed a good inhibitory potency of **5d** for TAK1, a kinase involved in the classical NF-κB activation pathway. Then, a dose-response assay confirmed the inhibitory potency of **5c-d** against TAK1 with an IC_{50} of 0.58 and 2.1 µM respectively. Finally, a docking study of both compounds brought to light the molecular interactions of pyrazolo[4,3-*c*]isoquinolines **5c-d** with TAK1.[110]

Regarding the interest for TAK1 inhibition, Tang *et al.* showed on one hand that conditional deletion of TAK1 in knockout mice leads to multiple organ defects, during development, and to death, after 8-10 days,[130,131] suggesting that TAK1 is essential for the development. On the other hand, a patent published in December 2009 described the interest of TAK1 inhibitors in the cancer treatment.[132] In this context, the pyrazolo[4,3-*c*]isoquinoline **5c** appears clearly as a novel interesting TAK1 inhibitor.[110]

Molecular modelling can be used once more to develop stronger and more specific TAK1 inhibitors based on the pyrazolo[4,3-*c*]isoquinoline scaffold. Orientation of the chemical structure **5d** in the ATP-bonding site of TAK1 is illustrated in figure 37:

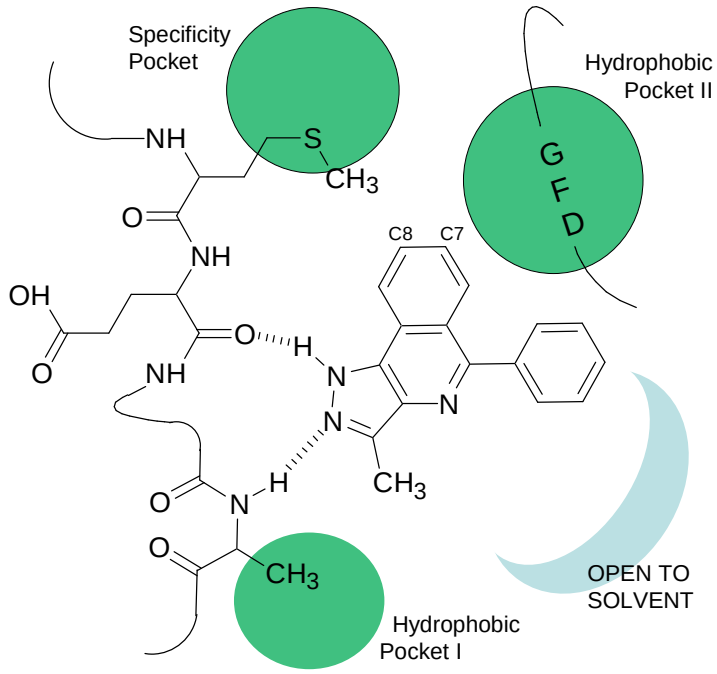

Figure 37: 2D representation of the pyrazolo[4,3-*c*]isoquinoline **5d** in the ATP binding site of TAK1.

To improve the drug-enzyme interactions, the specificity pocket,[90] or hydrophobic pocket II,[86] located behind the gatekeeper (M104) could be targeted by adding a hydrophobic substituent on C8 of the pyrazoloisoquinoline (Figure 37). But the steric hindrance of the methionine side-chain is not propitious to favour the access to this pocket. To enhance inhibitor specificity, another substitution on C7 could be an interesting proposal to target the DFG-out conformation of the ATP-binding site, an inactive kinase conformation (Figure 37).[86] This strategy has to consider a H-bond donor/acceptor link and an hydrophobic functional group targeting an allosteric site. For instance, imatinib is the most famous example considering this inhibition type.[133] Another hydrophobic region is also often targeted in kinase inhibition. Called hydrophobic pocket I (Figure 37), this

site is smaller than the previous ones and is located just above the gk+3 residue (A107). The methyl group of the pyrazole moiety is pointing right to this site. Substitution by ethyl, propyl or isopropyl could therefore be of interest. Finally, as far as a nucleophilic cysteine residue is found in the cavity, a covalent type inhibition could be considered. An electrophilic group on the scaffold could react with C174, at the lip of the ATP-binding site. Therefore, irreversible covalent bound is then a third way to target TAK1. These suggestions emerge as perspectives of this work.

5.7 Conclusions

The initial goal of this work was to build a 3D-model of NIK and study a series of known pyrazolo[4,3-*c*]isoquinolines, claimed as NIK inhibitors,[103] with a view to elucidate the required structural elements for NIK inhibition. In the absence of any experimental structural data on this enzyme, we built a 3D-model of NIK by using comparative modelling techniques. The binding of pyrazolo[4,3-*c*]isoquinolines claimed as NIK inhibitors was directly analysed in the putative active site. Surprisingly, this study revealed a poor binding orientation of the template inside the ATP-binding pocket of NIK. This suggested either a poor inhibitory potency or an alternative mechanism of inhibition. Based on the modelling results, we synthesised some pyrazolo[4,3-*c*]isoquinolines (**5a-d**) and studied their inhibitory potency in two tests involving NIK: (i) an isolated enzyme assay using human recombinant NIK, and (ii) a cellular assay where the alternative NF-κB pathway is only involved. As a result, all synthesised molecules were completely deprived of any significant inhibition on both assays. On the contrary to the original patent, this confirmed these compounds were neither inhibitor of NIK, nor of the alternative NF-κB activation pathway.

By performing a multikinase screen using **5d** as example, the effective target of these pyrazolo[4,3-*c*]isoquinolines in the NF-κB activation was elucidated.

In the original patent,[103] the NIK inhibitory potency claimed by Flohr *et al.* was based on the ability of pyrazolo[4,3-*c*]isoquinolines **5** to prevent TNFα and IL-6 release from human peripheral blood lymphocytes after stimulation by LPS or IL-1β. Such readout is inappropriate to discriminate the alternative from the classical activation pathway. On the contrary, the present study demonstrated that pyrazolo[4,3-*c*]isoquinolines are not NIK inhibitors but are likely modulators of the classical NF-κB pathway through TAK1 inhibition. Then, these results allow to re-assess the inhibition mechanism in this series.[110]

As we aimed at designing inhibitors of the NF-κB alternative activation pathway, we focused again our efforts on NIK. By demonstrating a lack of inhibition potency of pyrazolo[4,3-*c*]isoquinolines against NIK, we validated our model, which predicted a poor affinity in this series. To identify novel inhibitors of this enzyme, two different virtual screenings (VS) based on this 3D-structure were performed and are reported in the next section.

6. Virtual Screenings

Virtual (database) screening (VS) is an increasingly important component of the computer-based search for novel lead compounds. Two fundamental different approaches are described in the literature. The first one is based on a VS by docking ligands into the enzymatic active site. This requires knowledge of the 3D-structure of the targeted protein binding site to filter chemical structures by their likelihood to bind to the target. A second approach is a VS where no data about the protein structure are necessary/available. In this case, one or more pharmacophores that are known to bind to the target are used as a structural query.[134] Both screening procedures extract potential ligands from one or several databases according to appropriate criteria, in order to screen an ended number of relevant structures.

In the previous chapters, several results based on the 3D model of NIK were presented, including a mutagenesis study and a docking of molecules reported as NIK inhibitors. As all these investigations led to the validation of the 3D-model, we started a VS study based on a docking of compounds extracted from databases to discover potent NIK inhibitors.

6.1 Fragment database screening

6.1.1 *Fragment database*

Various chemical libraries can be used to perform VS. In this work, the VS focused on small-size molecules. Various reasons triggered this choice:

1. Chemical space can be more efficiently probed by screening collections of small chemical entities rather than large molecules libraries.[135]

2. Small molecules usually present a high ligand efficiency (LE).[b,136,137]

3. This approach increases the chance of hit discovery which can be presumably readily optimisable in further development. Such strategy offers an original and unique possibility to design new leads by fragment evolution or linking.[138]

A VS was then performed with an approach using a fragment chemical library. There is no single definition that can categorically distinguish between fragments and non-fragments, but there are general rules of thumb:[139]

1. Fragments are smaller than drug-like molecules, whether it is defined by MW or the number of heavy atoms (HA).

2. Fragments are less complex than drug-like molecules.

3. Fragments should be highly soluble.

4. Fragments should be devoid of undesirable chemical functionality, facilitating rapid development to more potent molecules.

The exact nature of a fragment library is very much depending on the screening protocol. In this study, the fragment database, built by Dr Raphaël Frederick,[140] was based on molecular fragments belonging to a wide variety of pharmaceuticals. It contains approximately 400 fragments and all the combinations of these pieces can reconstitute 99% of the commercially available drugs.[141,142]

---

[b] **The ligand efficiency** (LE) is the ratio of the binding free energy (ΔG) for a ligand and its molecular size measured by the number of heavy atoms (HA):

$$\mathbf{LE = \Delta G^0/HA \approx -RT\ ln(IC_{50})/HA \approx\ -0.592\ ln(IC_{50})/HA = LE_{exp}}$$

LE is a useful metric for measuring the impact on activity of the addition of more molecular bulk. Molecules that achieve a given potency with fewer heavy atoms (HA) are by definition more efficient.

6.1.1 *Fragments screening*

The selection of the fragments was performed in two steps, following the flowchart reported in figure 38:

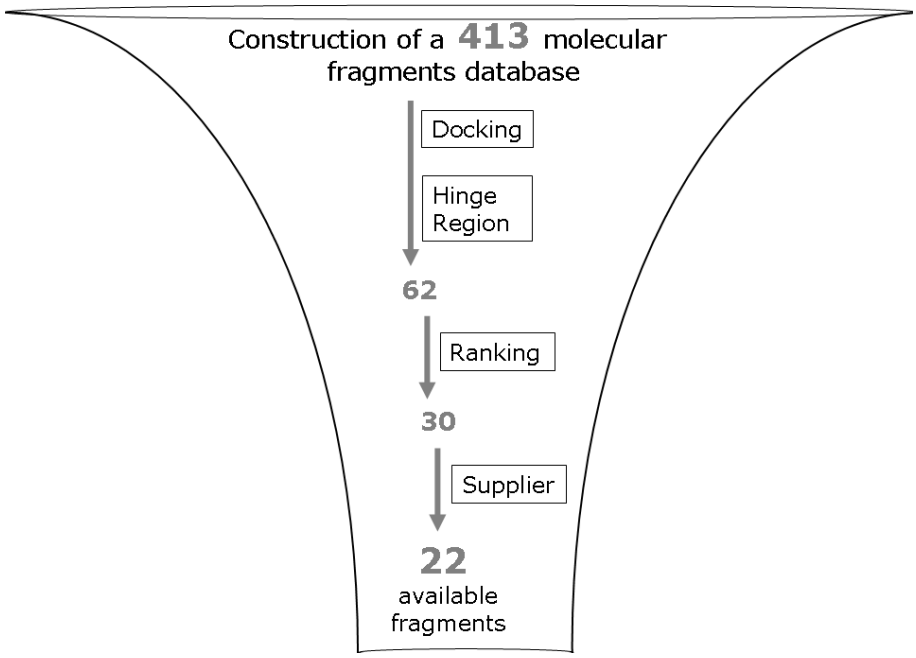

Figure 38: Fragments screening flowchart

First step: Using the automated software *GOLD*,[114] each fragment was docked 3 times in the modelled ATP-binding site of NIK. All these structures were then visually analysed inside the NIK binding cleft. Only fragments interacting with hinge region were selected (Figure 38). From the resulting 413 docked small-size molecules, 62 structures effectively displayed the critical H-bond interaction with the backbone NH of L472.

Second step: The 62 fragments interacting with the hinge region were ranked following three different scoring functions: *GOLDSCORE*, *CHEMSCORE* and *Astex Scoring Potential (ASP)*. The *GOLDSCORE* fitness function is made up of protein-ligand hydrogen bond energy, protein-

ligand van der Waals (vdw) energy, ligand internal vdw energy and ligand torsional strain energy.[114] *CHEMSCORE* estimates the total free energy change that occurs on ligand binding.[143,144] And the *ASP* scoring function is based on force fields or on regression, where parameters are derived from a set of experimental binding affinities and structures.[145] For each score, a theoretical ligand efficiency index ($LE_{goldscore}$, $LE_{chemscore}$ and LE_{asp})[c] was calculated.[137,146] Subsequently, a consensus LE index (LE_{total}) was obtained by meaning the three individual LE components. The 30 fragments possessing the best LE_{total} were selected. Finally, the 22 compounds appearing as commercially available were purchased and evaluated for their NIK inhibitory potency (Figure 39).

6.1.2 *NIK inhibition by fragments*

Typically, fragments bind to a target with an affinity (K_D) ranging from 100 to 10 mM. Detecting such a weak binding is a challenge for most biochemical and binding assays and routine fragment screening has relied on the development of a range of biophysical methods.[147] Testing the 22 molecular fragments in the same radioactive enzymatic assays was the only option at our disposal. The residual activity of NIK was measured in presence of the 22 fragments at a single concentration of 100 µM. Briefly, NIK, expressed in Sf9 insect cells as human recombinant GST-fusion protein, was purified by affinity chromatography using GSH-agarose. The substrate, a recombinant protein kinase (RBER-CHKtide) was also expressed in *E.coli*. The assay cocktails were incubated at 30°C for 60 minutes with [γ-^{33}P]-ATP (1 µM, pH = 7.5) and incorporation of ^{33}P was measured with a microplate scintillation counter. The NIK inhibitory potency of the fragment library was assayed at 100µM (Figure 40).

[c] **The theoretical ligand efficiency** (LE_{score}) is obtained by dividing the affinity score value by the MW of the compound (LE_{score} = score / MW).

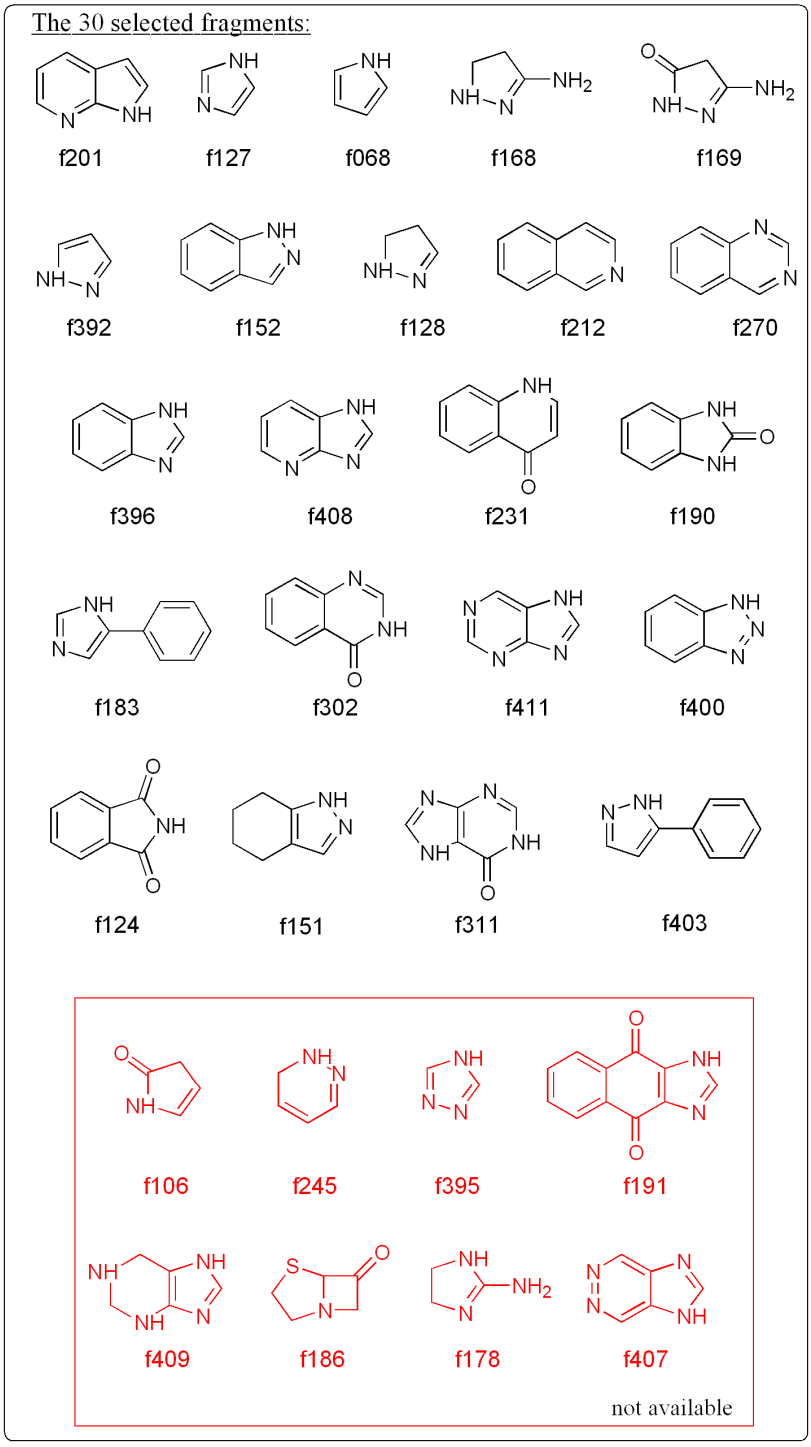

Figure 39: Molecular fragment commercially available (black) or not (red) selected by virtual screening

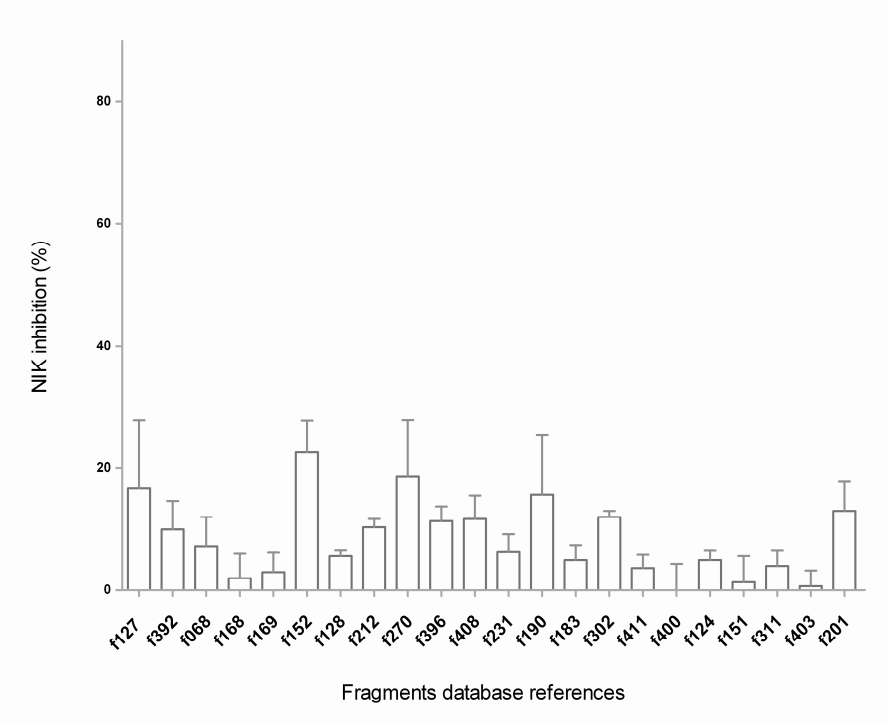

Figure 40: Human recombinant NIK inhibition level by the selected 22 fragments (100 µM). Mean ± SD (n = 3).

At this concentration, fragment F152 was the only chemical entity with an inhibitory potency against NIK over 20%. These results were considered as not strong enough to base the whole inhibitor design on them. It turned out that systems providing more sensitive and accurate binding measurements should have been complementarily used to succeed in this fragment screening. For example, the surface plasmon resonance or the nuclear magnetic resonance-based screening would be very appropriate to detect this fragments binding.[148,149] Regrettably, both techniques require pure recombinant NIK availability. The production and purification of the kinase was considered in this project by collaborators from the University of Liège (ULg) with a view to crystallise it and work out enzymatic assays. But this

work was not achieved during this project, because of big stability issues with this kinase.

Nevertheless, it is interesting to observe that, by this fragment-based screening strategy, we selected molecules structurally related to the adenine. Adenine is the molecular moiety which interacts with the hinge region of the enzymatic pocket, this observation validates our VS approach.

6.2 Commercial compound database screening

A second VS approach based on commercial compounds was carried on. Various chemical libraries like the NCI database (National Cancer Institute), the ACD (Available Chemical Directory) or ZINC library (over 8 million commercially-available compounds)[119] are available to perform VS. The latter, ZINC, was chosen, since it is free, web-accessible, offers ligands in a ready-to-dock 3D-format, and hits are purchasable for confirmatory evaluation. Using the same strategy than used for the fragment based design, this VS focused on small-size molecules. The VS flowchart is depicted in figure 41.

First step: Lipinski-style rules typical for fragments were first applied to the ZINC library.[150,151] The selected descriptors were molecular weight ($150 < MW < 250$), the hydrophobicity ($logP \leq 2.5$) and the number of H-bond donors ($DH \leq 2$) and acceptors ($HA \leq 4$) as the first filter. Then, all of the qualifying structures were downloaded from the ZINC website and transformed into a *UNITY* hit list file (*SYBYL*)[108] for compatibility with our modelling system. This resulted in a fragment-like library of roughly 67,500 structures (Figure 41).

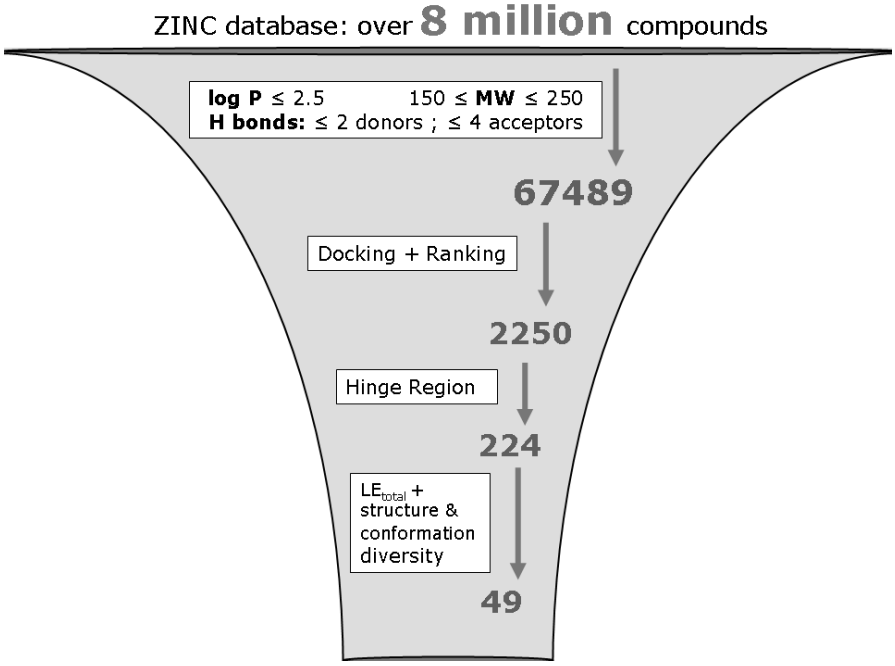

Figure 41: Virtual screening flowchart

Second step: The resulting molecules were then docked in the ATP-binding site of NIK using the automated *GOLD* program with parameters especially designed for a large database screening (7-8 fold acceleration).[114] The ATP binding site of NIK was delimited by a 10Å-sphere around staurosporine **28**, chosen as reference. As previously described, three docking positions were generated for each compound. Their affinity with NIK was then assessed using the same scoring functions as previously described, namely *GOLDSCORE*, *CHEMSCORE* and *ASP*. For each score, a theoretical ligand efficiency index (LE_{score}) was calculated.[137,146] Afterwards, the consensus LE index (LE_{total}) was as well obtained by means of the three individual LE components. Then, 2000 compounds possessing the best LE_{total} value as well as the 100 highest

compounds in each individual LE_{score} were selected. This led to a set of 2250 structures predicted to tightly bind NIK.

Third step: All these structures were at this time visually analysed inside the NIK binding cleft, and those that did not interact in the hinge region were discarded (Figure 41). From the resulting 1019 compounds, 324 structures effectively displayed the critical H-bond interaction with the backbone NH of L472, but only 224 of them were commercially available.

Fourth step: From this last set, 49 compounds were chosen because of their structural diversity and their appropriate conformation inside the NIK binding cleft (Appendix 2 & 3). Briefly, the type of interaction of each of the 224 structures in the hinge region was analysed, and at least one structure per conformation was selected. Additional compounds were also chosen on the basis of their high LE_{total} index. Compounds were ordered from different retailers (Chembridge, Enamine, ASDI, IBScreen, Maybridge, Vitas M, Alfa-Aesar, Key Organics, Oakwood, Acros, Sigma-Aldrich, Specs, Asinex and Apollo).

6.3 NIK inhibition by screened commercial compounds

6.3.1 *Enzymatic evaluation*

The NIK inhibitory potency of the 49 selected compounds was first evaluated using the same radiometric protein kinase assay than used for the molecular fragments. The residual activity of NIK was measured in presence of each molecule at a single concentration of 50 µM. From the 49 structures

identified by VS, two molecules (**29** and **30**) displayed an interesting NIK inhibitory potency with around 60% NIK inhibition at 50 µM (Figure 42).

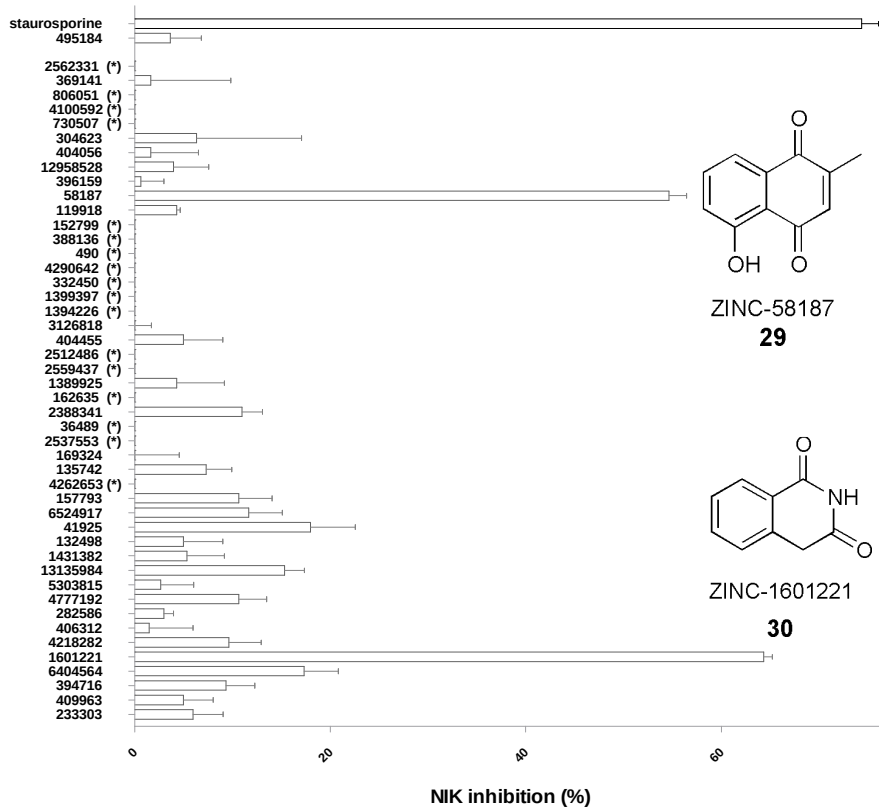

Figure 42: Human recombinant NIK inhibition level by the selected 49 compounds (50 µM) reported with ZINC codes. Molecules **29** and **30** are the two best inhibitors and (*) denotes NIK inhibition < 0 %. Staurosporine was used as reference. Mean ± SD (n = 3).

At this stage, this corresponds to an enrichment rate of about 4%, still an excellent result taking into account the use of a homology model instead of experimental 3D-coordinates of NIK. The present study therefore highlights the excellent potential of VS for the discovery of novel hits.

Compound **29** (Figure 42) is a 1,4-naphthoquinone substituted in the 2- and 5-position by a methyl and a hydroxyl moiety, respectively. However, quinones are Michael acceptors and known as DNA-alkylating agents. They are also highly redox active molecules and can potentially lead to the formation of reactive oxygen species including superoxide, hydrogen peroxide and hydroxyl radicals. These species in turn can lead to oxidative stress and the formation of oxidised cellular macromolecules.[152] So, despite the observed NIK inhibiton, **29** does not represent an interesting scaffold for future drug development.

On the contrary, compound **30**, an 4*H*-isoquinoline-1,3-dione, represents an interesting hit for the discovery of new potent NIK inhibitors.

6.3.2 *Validation and optimisation of the 4H-isoquinoline-1,3-dione* **30** *as NIK inhibitor*

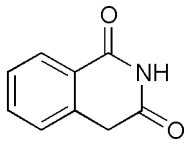

ZINC-1601221

30

Figure 43: Structure of 4H-isoquinoline-1,3-dione **30**

To validate the interest of the scaffold **30** against NIK (Figure 43), we started a research for molecules structurally related to this hit. Sixteen commercially available analogs of **30** were found and bought from retailers (Figure 44).[153] Their NIK inhibitory potency was then determined at 50 µM (Figure 45).

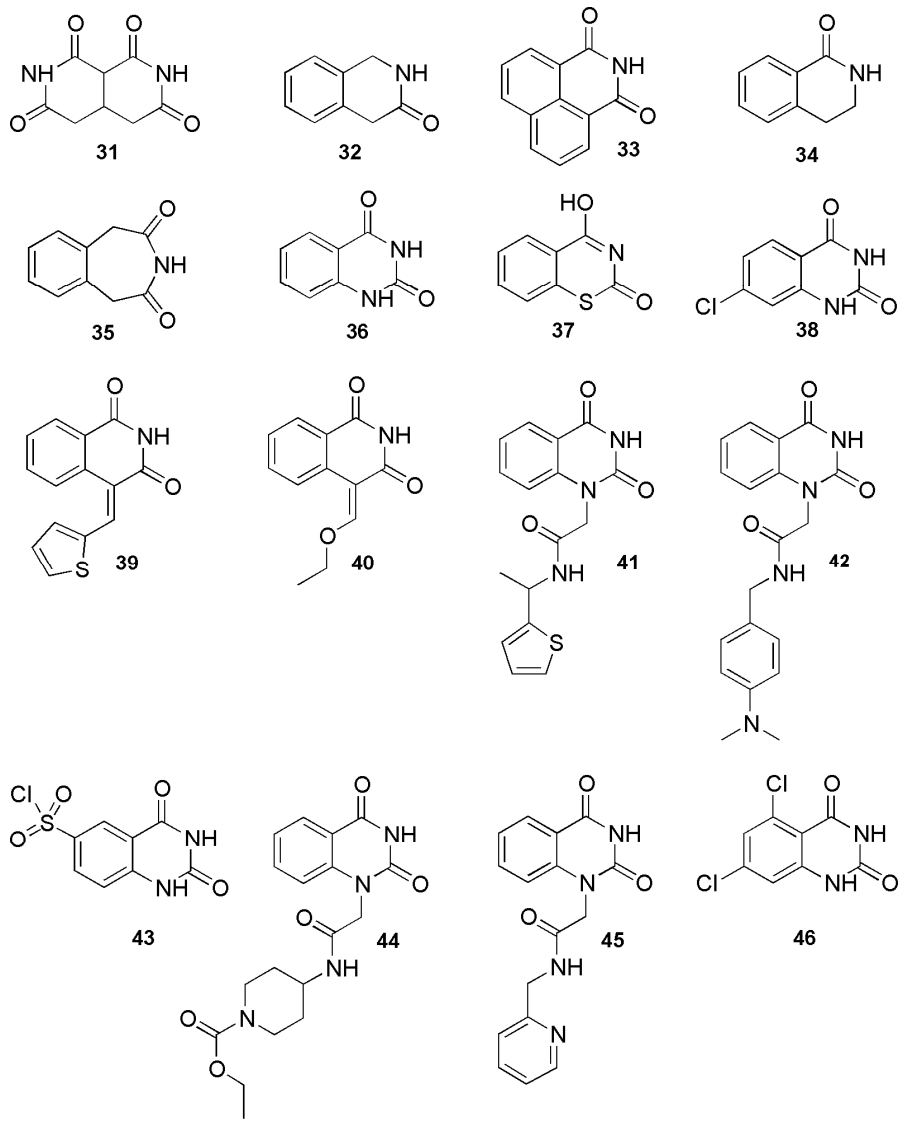

Figure 44: Isoquinolinedione analogs **31 - 46**

At 50 µM, five analogs **31, 32, 39, 40** and **46** were found to significantly inhibit NIK (>20% inhibition, Figure 45). Among them, **31** (53% inhibition at 50 µM) and **40** (44% inhibition at 50 µM) are the most potent compounds. Compound **31**, a 2H,4H,5H,7H-2,7-naphthyridine-

1,3,6,8-tetrone scaffold, is structurally different from the original isoquinoline-1,3-dione template of **30** and therefore could constitute a novel interesting scaffold for the development of novel NIK inhibitor.

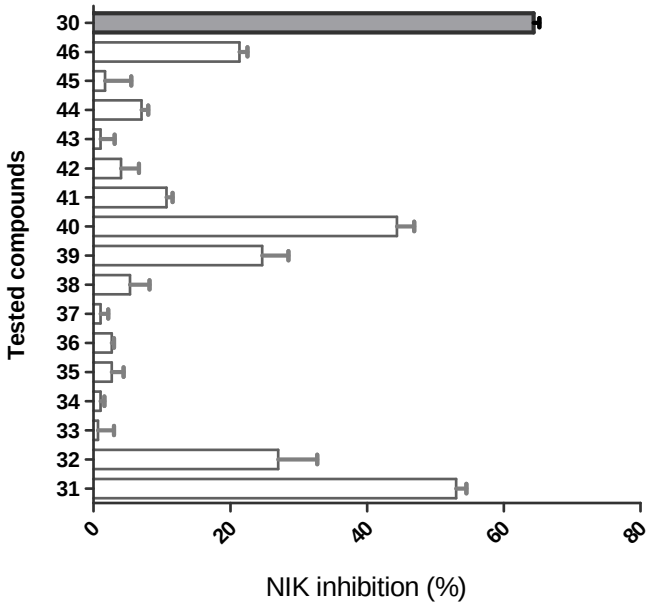

Figure 45: Inhibitory potency of isoquinolinedione **30** and analogous compounds (50 µM). Mean + SD (n = 3).

Compound **40** is an isoquinoline-1,3-dione ring substituted in the 4-position by an ethoxymethylene group. Is it interesting to note that the substitution in this position seems tolerated but only with a rather small group. In fact, except compound **39** (25% inhibition at 50µM) substituted by a thiophenylmethylene moiety in this position, molecules **41, 42, 44** and **45,** bearing a bulkier group, are completely inactive on NIK (inhibition <15% at 50 µM, figure 45). Another hypothesis to explain the activity of **40-41** is the presence of a Michael acceptor exocyclic double bond which is not present in **41, 42, 44** and **45** (Figures 44 et 45). This reactive Michael acceptor might play a role in the binding of these derivatives.

The dose-response inhibitory potency of the most potent compounds was performed. The required concentration (IC_{50}) to reduce of 50% the NIK activity was evaluated for compounds **30**, **31, 32, 39, 40** as well as **46**, and compared to that of staurosporine **28**, chosen as reference (Table 8). Although less potent than staurosporine, **30** remains the most interesting NIK inhibitor with an IC_{50} value of 51 µM. The 2,7-naphthyridine-1,3,6,8-tetrone **31** is less potent with an IC_{50} of 90 µM. Compounds **32, 39, 40** and **46** exhibit IC_{50} values >100µM.

As a parameter for assay quality, the Z´-factor was used for the low and high controls of each assay plate.[154] Our criterion for repetition of an assayed plate is a Z´-factor lower than 0.4.[155] In this experiment, Z´-factors did not drop below 0.77, indicating an excellent assay quality. As an additional control, a 1 % DMSO plate was included as an indicator for putative washing and/or pipetting variations. The calculated coefficient of variation was 5.01 %.

Interestingly, compounds **30** and **31** are characterised by a high ligand efficiency index (LE_{exp})[d136] of 0.42 and 0.39, respectively whereas the LE_{exp} of staurosporine is 0.22 only. So, the LE_{exp} of **30** and **31** is above 0.3 which is usually described as a minimum for further development,[138] and thus corroborates their potency as novel NIK inhibitory scaffolds (Table 8).

[d] **The experimental ligand efficiency index** (LE_{exp}) is the ratio of the coefficient RT ln(IC_{50}) and the number of heavy atoms (HA) of the compound:

$$\mathbf{LE_{exp} = -0.592\ ln(IC_{50})/HA}$$

Table 8 : Concentration reducing of 50% of the NIK activity (IC_{50}) and ligand efficiency index (LE_{exp}) calculated from the IC_{50} and the number of HA

Compound	**IC_{50} (µM)**	**HA**	**LE_{exp} = -0.592 ln(IC_{50})/ HA**
Staurosporine **28**	2.3	35	0.22
30	51	14	0.42
31	90	14	0.39
32	>100	11	ND
39	>100	18	ND
40	>100	16	ND
46	>100	14	ND

HA = heavy atoms, LE = ligand efficiency, ND = not determined.

6.3.3 *Molecular docking of* **30** *and* **31**

To understand how these two compounds **30** and **31** achieve their potency, we deeply investigated their binding conformation inside the NIK cavity. Both molecules were docked inside the NIK-binding site as previously described. In order to take into account the protein flexibility, the best conformation was further refined using the *MINIMIZE* module implemented in *SYBYL 8.0* (Tripos force field and Gasteiger-Hückel charges). Key interactions stabilising the compounds **30** and **31** are depicted in figure 46.

Both inhibitors are deeply inserted in the NIK cavity. As expected, for each compound, one H-bond acceptor atom, *i.e.* the oxygen atom from the carbonyl in position 1, onto the ligand is H-bonded to the L472 backbone NH located in the NIK hinge region (ATP-binding site). Additionally, both compounds are also stabilised through a supplementary H-bond between one H-bond donor atom, *i.e.* the nitrogen atom in position 2, onto the ligand and

the L472 CO backbone. Except these two H-bonds, the NIK inhibitory potency could be attributed mainly to the close shape complementarities and van der Waals contacts between these two inhibitors and the NIK active site (Figure 46).

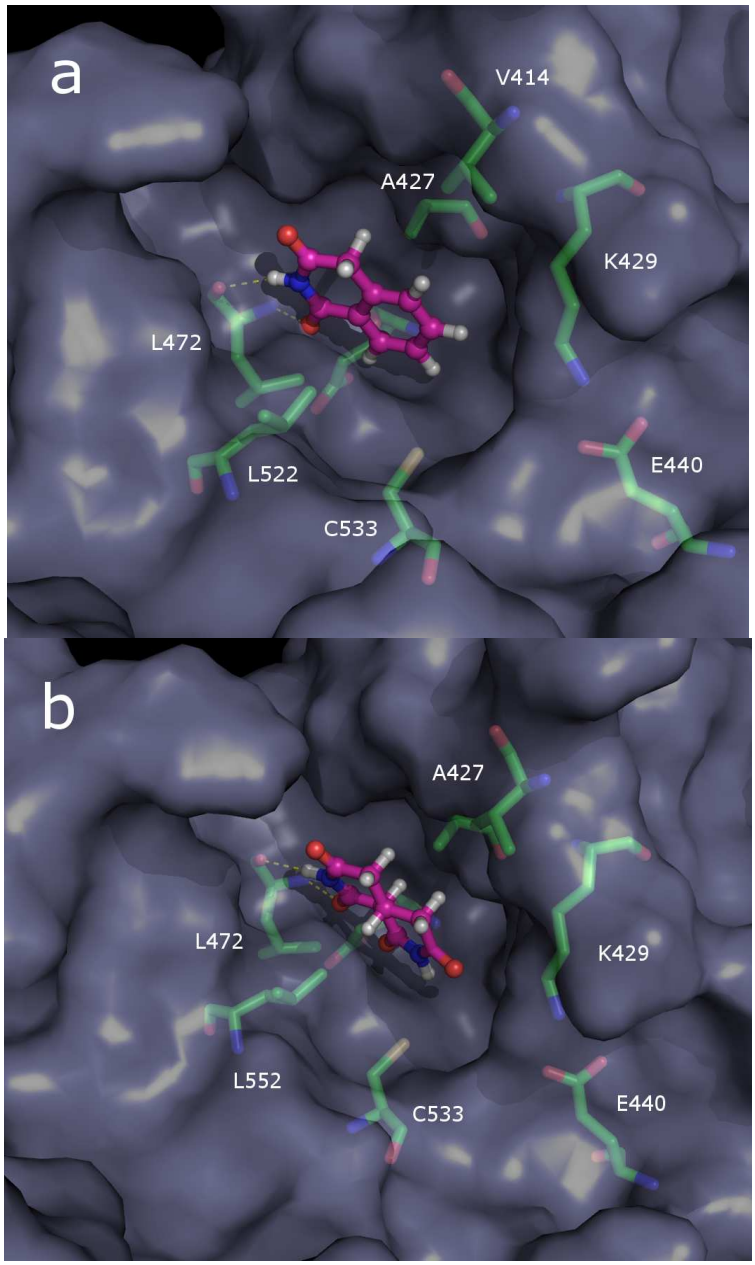

Figure 46: Compounds **30** (a) and **31** (b) docked in the ATP binding site of NIK

6.4 NF-κB alternative pathway inhibition by screened commercial compounds

6.4.1 *Biological evaluation*

In parallel, the inhibitory potency of the 49 selected compounds was evaluated in the NF-κB alternative pathway. These experiments were also performed at the ULg (GIGA) by the group of Dr E. Dejardin. Briefly, each compound was assayed using carcinoma Hela cells expressing LTβR. The NF-κB alternative pathway was induced (or not) by an LTβR agonist antibody. After induction, NIK was overexpressed and the processing of p100 into p52 was triggered by phosphorylation of IKKα. Then, the p100/p52 ratio was finally analysed by Western blot and staurosporine **28** was used as reference.

Up to 50 µM, the compound **30** did not inhibit the alternative pathway. The Michael acceptor **29** displayed a strong cytotoxicity at 50µM and 10 µM. This is in accordance with the previously discussed properties of this quinone scaffold and its potential toxicity.[152] No inhibition was therefore observed for **29**.

However, an interesting result was observed with compound **47** that partially inhibited the alternative pathway at 50µM and 100µM (Figure 47). This inhibitory potency of **47** was unexpected, since no inhibition was observed with this compound in the radiometric assay, as previously reported (Figure 42,). To elucidate the inhibitory potency of the NF-κB alternative pathway, the biological properties of the pyrazole **47** were further investigated.

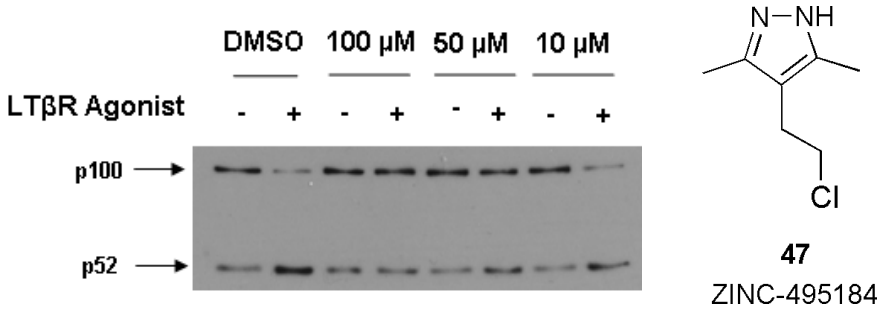

Figure 47: Processing of p100 into p52 from Hela cells expressing LTβR stimulated by an LTβR agonist antibody. Cells were incubated in absence or in presence of **47** at 10, 50 and 100 µM. DMSO, used as cosolvent, has no effect.

A cell viability assay estimating the ATP production was performed using a CellTiter-Glo® luminescent cell viability assay (Figure 48). Whatever the concentration applied, **47** did not impair the ATP production of the cultured Hela cells incubated for 6 hours. The inhibition of the p100/p52 processing observed in the assay involving the alternative pathway is therefore not caused by toxicity issues.

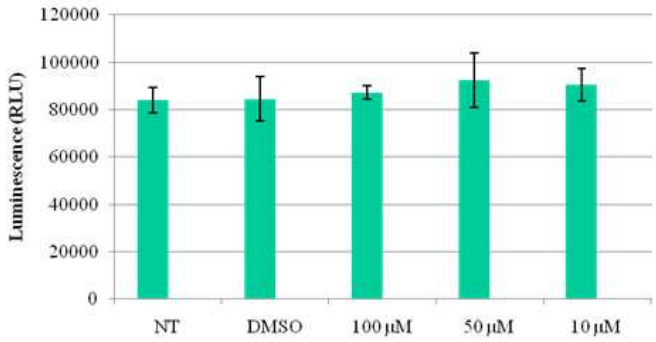

Figure 48: Hela cells ATP production in presence of compound **47** incubated for 6 hours at 10, 50 and 100µM. NT = not treated; DMSO was used as cosolvent

The inhibitory selectivity of **47** between both classical and alternative NF-κB activation pathways was also evaluated. In this assay, the

classical NF-κB activation pathway only was activated by TNFα (Figure 49). To bear out an inhibition of this pathway by **47**, the degradation of IκBα was analysed.

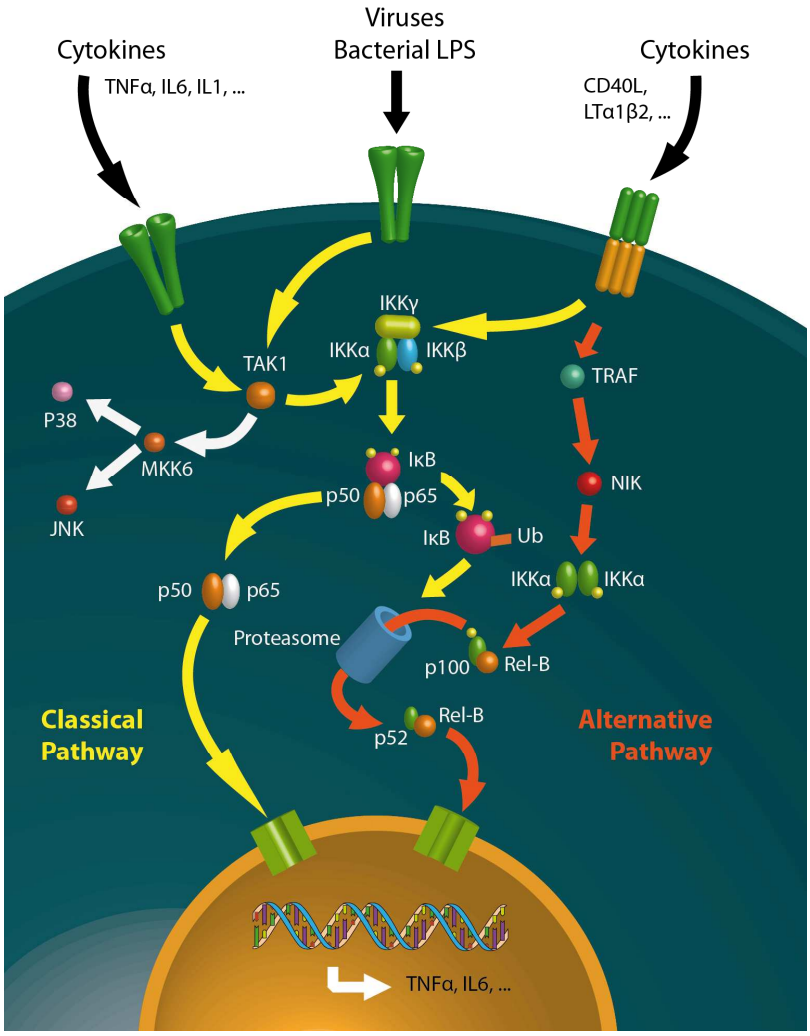

Figure 49: Classical (yellow) and alternative (orange) NF-κB activation pathways

By this assay, it was demonstrated that the pyrazole **47** is not an inhibitor of the classical NF-κB activation pathway. As reported in figure 50,

when the classical pathway is activated by the agonist TNFα, the degradation of IκBα is complete with compound **47** (50µM) or without (DMSO). Conversely, when only the alternative pathway is activated by a LTβR agonist with the same incubation delays, **47** inhibits significantly the processing of p100 into p52 (Figure 50).

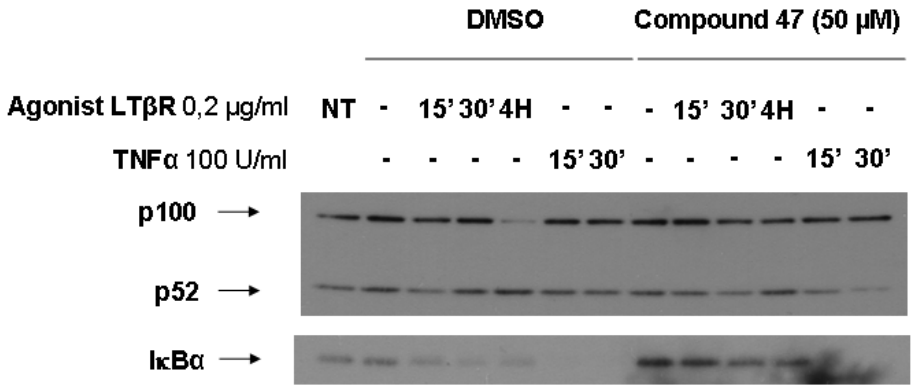

Figure 50: NF-κB activation pathway selectivity for compound **47**. NT = not treated; DMSO was used as cosolvent

Taking into account these results, a new hit displaying a significant and selective inhibition of the NF-κB alternative activation pathway was identified. Similarly to the previous scaffold **30**, also discovered by VS, a validation and optimisation of this pyrazole **47** was considered.

6.4.2 *Validation of the 4-(2-chloroethyl)-3,5-dimethyl-1H-pyrazole* **47** *as inhibitor of the NF-κB the alternative pathway*

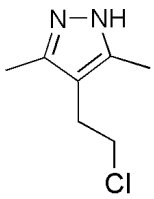

47
ZINC-495184

Figure 51: Structure of 4-(2-chloroethyl)-3,5-dimethyl-1H-pyrazole **47**

With a 2-chloroethyl function, the 3,5-dimethyl-1H-pyrazole **47** appears as a potential alkylating agent (Figure 51). Such molecules are reported to be DNA cross-linking and may therefore be toxic for cells.[156] Their mode of action is characterised by an alkylation of a DNA base,[157] stopping the mitosis in the late G1 or S phase because of a destroyed DNA.[156] Such mechanism being extremely unspecific, it seemed necessary to measure the relative importance of the halogen function in **47**. For this reason, but also with a view to establish the first structure-activity relationships (SAR), various analogs of **47** were synthesised or purchased.

First, the 3,5-dimethyl-4-propyl-1H-pyrazole **48** was synthesised in order to evaluate the inhibition potency of the closest structure without any potential alkylating properties. This compound was prepared in two steps from the pentane-2,4-dione **49**. The acid 3-position of the dione **49** was deprotonated by the 1,8-diazabicyclo[5.4.0]undec-7-ene (DBU) and reacted with the iodopropane to form the 3-propyl-pentane-2,4-dione **50**. Without intermediate purification, the dione **50** reacted with hydrazine hydrate to form the pyrazole **48** (Scheme 3).

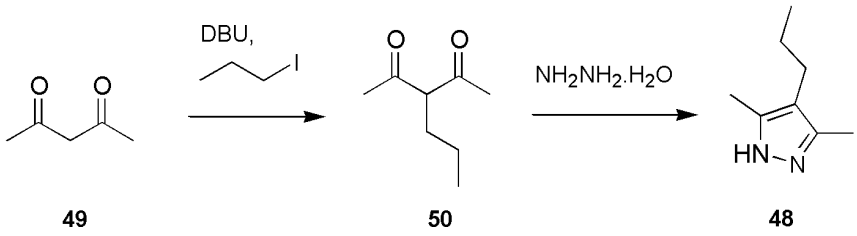

49 50 48

Scheme 3 : Synthesis of 3,5-dimethyl-4-propyl-1H-pyrazole **48**

In parallel, various structurally related compounds were searched in commercial databases. Eleven available molecules displaying a common 4-(2-ethyl)-3,5-dimethyl-1H-pyrazole moiety were purchased. Every analogs were then evaluated in the NF-κB alternative activation pathway (Figure 51).

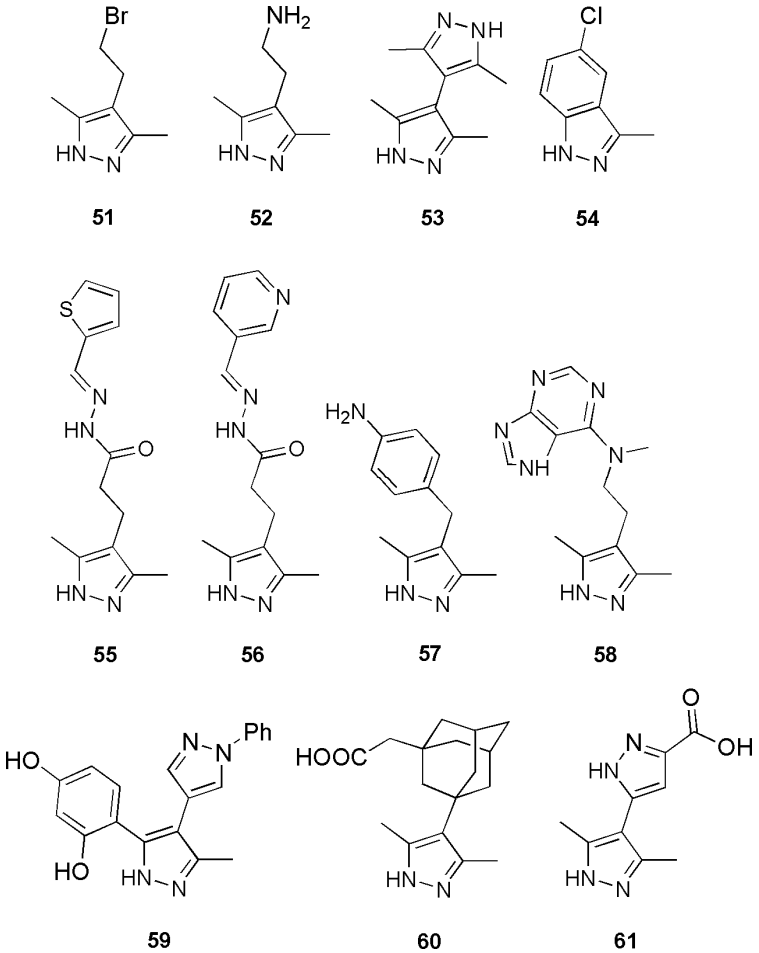

51 52 53 54

55 56 57 58

59 60 61

Figure 51: Commercial compounds structurally related to **47**

First, compound **59** displayed an interesting inhibitory potency against the alternative pathway. Unfortunately, this inhibition is explained by an important toxicity for compound **59**, expressed as a reduced cells ATP-production (Figures 52).

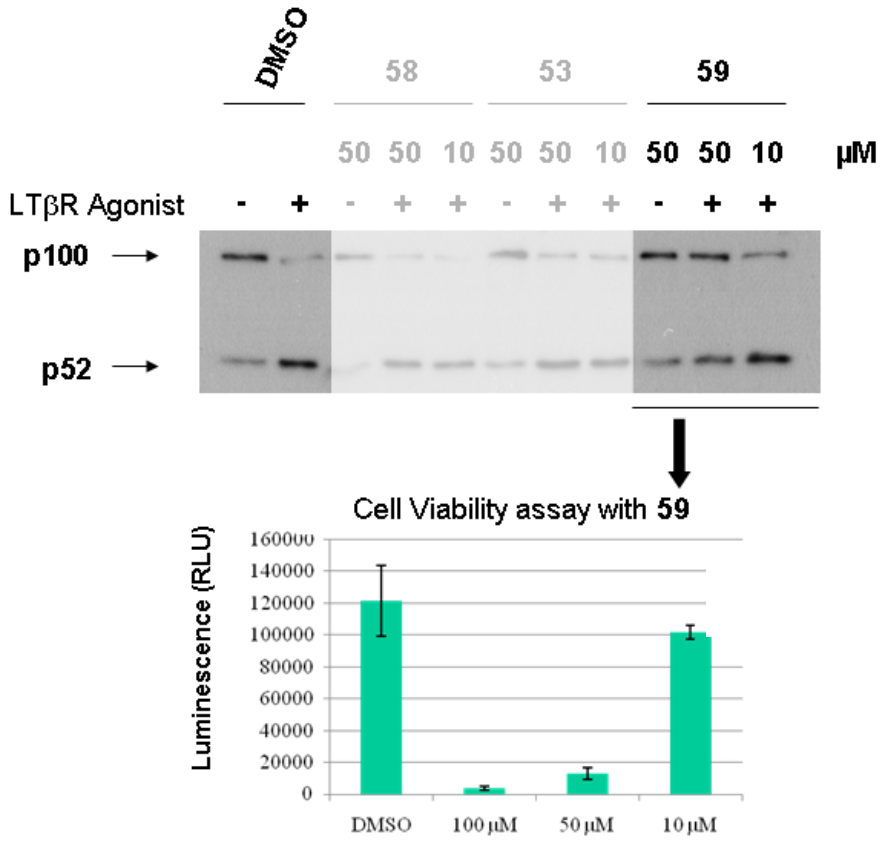

Figure 52: Processing of p100 into p52 from Hela cells expressing LTβR stimulated by an LTβR agonist antibody (LIGHT). Cells were incubated in absence or in presence of compounds **58, 53** and **59** at 10µM and 50 µM. Only **59** displays a partial inhibitory potency at 50 µM. A cell viability assay, expressed as ATP production, shows an important toxicity for compound **59** at 100µM and 50µM. DMSO was used as cosolvent.

Conversely, analogs **51** and **52** inhibit the processing of p100, as reported in figure 53:

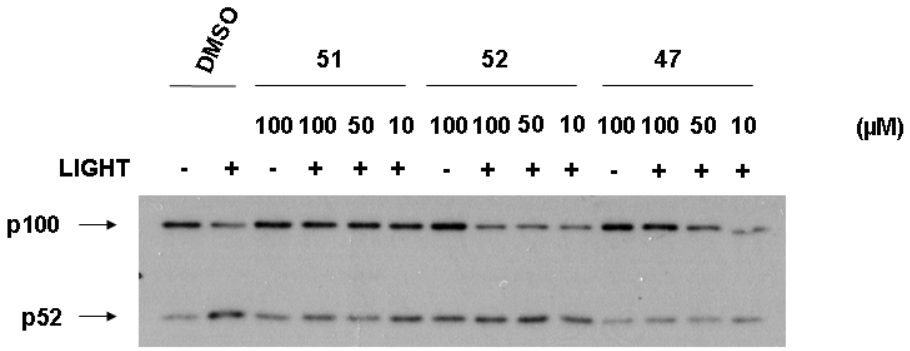

Figure 53: Processing of p100 into p52 from Hela cells expressing LTβR stimulated by an LTβR agonist antibody (LIGHT). Cells were incubated in absence or in presence of compounds **47, 51** and **52** at 10µM, 50 µM and 100 µM.

In comparison to the previously discovered fragment **47**, 4-(2-bromoethyl)-3,5-dimethyl-1H-pyrazole **51** is significantly more potent and inhibits partly the alternative pathway even at 10 µM (Figure 53). The inhibitory potency of the 4-(2-amino-ethyl)-3,5-dimethyl-1H-pyrazole **52** is however less interesting with a partial inhibition of the p100 processing only at 100µM. Cell viability assays was also performed to assess that the observed inhibition is not induced by toxicity issues. As a result, **51** impairs the ATP production at 100 µM only (Figure 54).

51

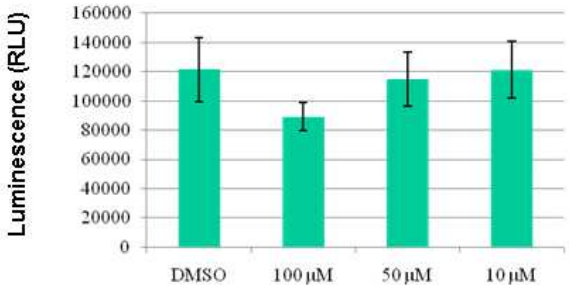

52

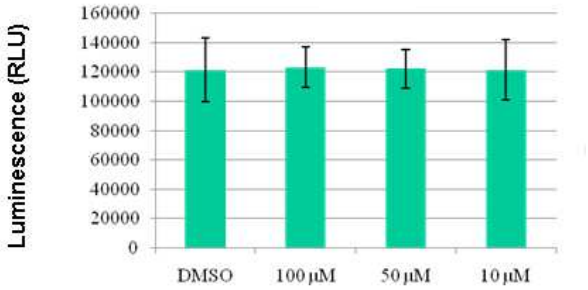

Figure 54: Cell viability assays, expressed as ATP production, for compounds **51** and **52** at 100, 50 and 10 µM. DMSO was used as cosolvent.

Finally, in this series, two compounds displaying a good inhibitory potency against the alternative pathway were identified. Unfortunately, these two compounds **47** and **51** are both potential alkylating agents and this inhibition mechanism can not be excluded. So, potential side-effects due to a lack of specificity are underlying any further development of this series. Nevertheless, it remains essential to assess its inhibition mechanism as well as its effective target in this pathway. To our knowledge, 4-(2-halogeno-ethyl)-3,5-dimethyl-1H-pyrazoles are the first selective inhibitors of the NF-κB alternative activation pathway.

6.5 Conclusion

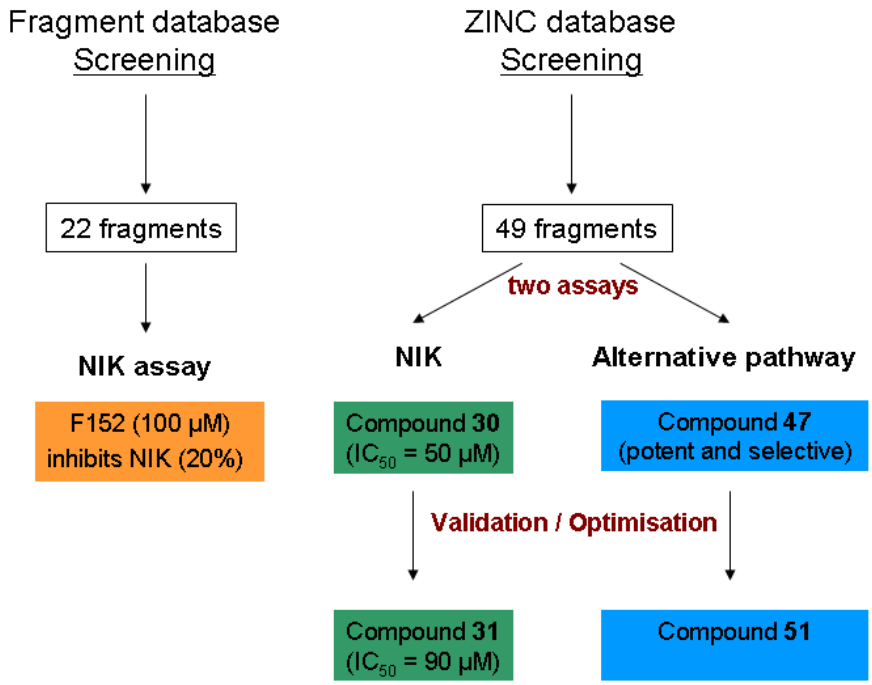

Figure 55: VS summary

At the end, it is interesting to turn back to the first reported structures identified by fragment screening. Even if the detection techniques were inappropriate for low affinities due to small molecules, the compounds selection was actually very coherent. Most of these fragments, reported in the figure 39, are structurally very close to at least one of these three scaffolds:

1. adenine, the natural substrate of kinases (f201, f127, f152, f270, f396, f408, f190, f183, f302, f411, f400, f407, f409 and f311);

2. isoquinolinedione **30**, identified by VS as a putative NIK inhibitor (f212, f270, f231, f190, f302, f124, f311, and f106);

3. pyrazole, as highlighted by VS with the series of compounds **47** and **51** and inhibiting the alternative pathway (f068, f168, f169, f128, f392, f151, f403, f395 and f409).

So, even in absence of outstanding results, the 3D-model used for high-throughput docking is undoubtedly validated.

Thus, this VS study led to the discovery of two series of inhibitors (Figure 55). First, the 4*H*-isoquinoline-1,3-dione **30** exhibited an IC_{50} of 51µM against NIK. As this hit was validated, it corresponds to an enrichment rate of about 2%. Although enrichment rates in the range of 10% to 30 % were previously reported by VS using experimentally determined 3D structures, this is still an interesting rate taking into account (i) the use of an homology model but not experimental 3D-coordinates of NIK for the VS, and (ii) that the hit rate usually obtained by high-throughput screening is only 0.02% in most cases.[158] The present study is therefore another example highlighting the potential of VS for the discovery of novel hits. Thanks to a structural research, the 2H,4H,5H,7H-2,7-naphtyridine-1,3,6,8-tetrone **31** was also evaluated and displayed an IC_{50} of 90 µM. Both inhibitors **30** and **31** displayed good LE_{exp} comparing to staurosporine **28**.[159]

The binding modes of both molecules within NIK were finally evaluated, and revealed essential features responsible for their NIK inhibition potency. Particularly, these compounds interact with the hinge region of NIK *via* a lactam moiety, similarly to staurosporine which is known to be an ATP-competitive pan-kinase inhibitor. Based on this observation, it could be hypothesised that these molecules inhibit NIK with a similar mechanism.

The isoquinolinyl scaffold of **30** was recently reported as a cyclin-dependent kinase 4 (CDK4) inhibitor.[160,161] So, the screening of a selection

of commercial compounds in the 3D-model of NIK led to the discovery of potent inhibitors previously validated on a structurally related target (CDK4), corroborating the relevance of our strategy as well as our tools. Moreover, despite a common structural moiety with this CDK4-inhibitor series, the fragment based approach allows us to avoid specificity issues. It remains therefore to develop these scaffolds **30** and **31** which are, to the best of our knowledge, the first validated NIK inhibitors (with the recently patented alkynyl-alcohol).[101,110]

Secondly, 4-(2-halogenoethyl)-3,5-dimethyl-1H-pyrazoles like compounds **47** and **51** were identified as NF-κB alternative activation pathway inhibitors. Their mechanism of action remains to be clarified and, being potential alkylating agents, the specificity issues of this series must be considered in the scaffold optimisation. Fortunately, a first cell viability assay performed revealed the absence of cytotoxicity for molecular fragments **47** (at 100, 50 and 10 µM) and **51** (at 50 and 10 µM). On this account, these molecules are very promising in the field of the alternative pathway investigation.

Conclusion and perspectives

In the field of inflammation, our research focused on the inhibition of the NF-κB alternative activation pathway, a new promising therapeutic strategy against pathologies like RA. In this protein cascade, NIK was considered as a promising target for drug design. The number of known inhibitors for this kinase being very limited, we studied this enzyme on different levels.

In the absence of any experimental structural data on NIK, we built and validated the first 3D-model of NIK using comparative modelling methods. The ATP-binding site of NIK was then investigated deeper by means of a mutagenesis study leading to the identification of key amino acids. On one hand, some highly recovered residues were by this way recognised and located in the 3D-structure (K429 and T559). Their role in the phosphate transfer mechanism was confirmed by the effective inability of their mutant to activate the corresponding pathway. On the other hand, new residues identified by a four filters selection were also acknowledged as essential for the enzymatic activity of NIK (F436, D534, F535 and H562). In the meantime, K430 was also demonstrated to be unnecessary for its phosphorylation mechanism.

With a view to elucidate the required structural elements for NIK inhibition, we started a docking study of a series of pyrazolo[4,3-*c*]isoquinolines, claimed as NIK inhibitors.[103] The binding of these pyrazolo[4,3-*c*]isoquinolines was directly analysed in the putative active site of NIK, revealing a poor binding orientation of the template. Conversely, the docking of the pankinase inhibitor staurosporine **28** was consistent and reproducible. This suggested either a poor inhibitory potency or an alternative mechanism of inhibition for pyrazolo[4,3-*c*]isoquinolines (**5a-s**).

Based on this docking study, some pyrazolo[4,3-*c*]isoquinolines (**5a-d**) and some structurally related pyrazolo[3,4-*c*]isoquinolines (**11a-l**) were synthesised to evaluate their inhibitory potency in two different assays involving NIK. The first *in vitro* assay was performed with human recombinant NIK. The second one was a cellular assay where the alternative NF-κB pathway only was induced by a LTβR agonist. As a result, all synthesised molecules were completely deprived of any significant inhibition on both systems. Nevertheless, staurosporine **28**, which was used as positive control, validated the tests. These compounds were then neither inhibitor of NIK, nor of the NF-κB alternative activation pathway, confirming the docking study and validating the 3D-model of NIK.

To elucidate the potential target of these pyrazolo[4,3-*c*]isoquinolines in the NF-κB activation, a multikinase screen was performed using **5d** as example**.** This screening revealed interesting inhibition properties of **5d** against TAK1, a kinase which is involved in the classical NF-κB activation pathway. This was further confirmed by the determination of the inhibitory potency (IC_{50}) of **5c-d** *vs.* TAK1. This study allowed then to re-assess the inhibition mechanism of this series and led to a reliable 3D-model of NIK, used to search for novel inhibitors by virtual screening (VS).

The last part of this work was based on two different VS strategies: a commercial compounds database screening and a molecular fragment database screening. Unfortunately, the fragments screening led to the identification of molecules with low affinities. It was due to the small-sized selected compounds and to experimental techniques being not adapted to detect such binding. Conversely, the commercial compounds database screening was successful. We proceeded to combine various filters including high-throughput docking, using the 3D-homology model and ranking through different scoring functions.

From the 49 selected and assayed final compounds, two molecules exhibiting a NIK inhibitory potency of about 50% at 50 µM were identified (**29** and **30**). One of them (**30**) was characterised by an IC_{50} of 51µM. Structural analogs of the isoquinolinedione **30** were then searched, leading to the identification of **31** endowed with an inhibitory potency (IC_{50}) around 90 µM. The binding modes of these two molecules within NIK were evaluated, revealing features responsible for their NIK inhibition potency. These two chemical fragments are characterised by excellent experimental ligand efficiency (LE_{exp}), thus making them very potent and interesting starting points for the development of new structures for NIK inhibition.

After the same VS study, compound **47** was identified as inhibitor of the NF-κB alternative activation pathway. Another compound (**51**), structurally close to **47**, effectively inhibits this pathway as well, confirming the interest of this 4-(2-halogenoethyl)-3,5-dimethyl-1H-pyrazole scaffold. Unfortunately, a halogeno-ethyl group seems to be necessary for the activity of these pyrazoles **47** and **51**. Though, such chemical structures are potential alkylating agents, leading to the fear of a lack of specificity in this series. Nevertheless, this scaffold remains very interesting for several reasons:

1. As far as we know, this is the only series effectively and selectively inhibiting the alternative pathway activation of NF-κB.

2. Up to now, the target remains uncertain and further developments could lead to the identification of (i) a new protagonist of the alternative pathway; (ii) a cytosolic form of NIK different from of the kinase expressed in insect cells as human recombinant GST-fusion protein (as used in the radiometric assay) or (iii) an non-competitive mechanism of inhibition of NIK, stabilising the phosphorylated form of the enzyme and leading to its degradation. These hypotheses could explain a lack of activity in the radiometric enzymatic assay with **47**.

3. Despite the potential alkylation mechanism of this series, this mode of action remains to be demonstrated. In case of inhibition of NIK (non-competitive or ATP-competitive inhibition, as suggested by the docking of **47** in the hinge region of NIK shown in figure 56) various pharmacomodulations around this scaffold could lead to bioisosteres of **47** and **51**. Such molecular analogs could then display the same (or better) inhibition properties without any potential alkylating group.

For all these reasons, the discovery of the 4-(2-halogenoethyl)-3,5-dimethyl-1H-pyrazole series by VS is a critical step in the study of the alternative pathway.

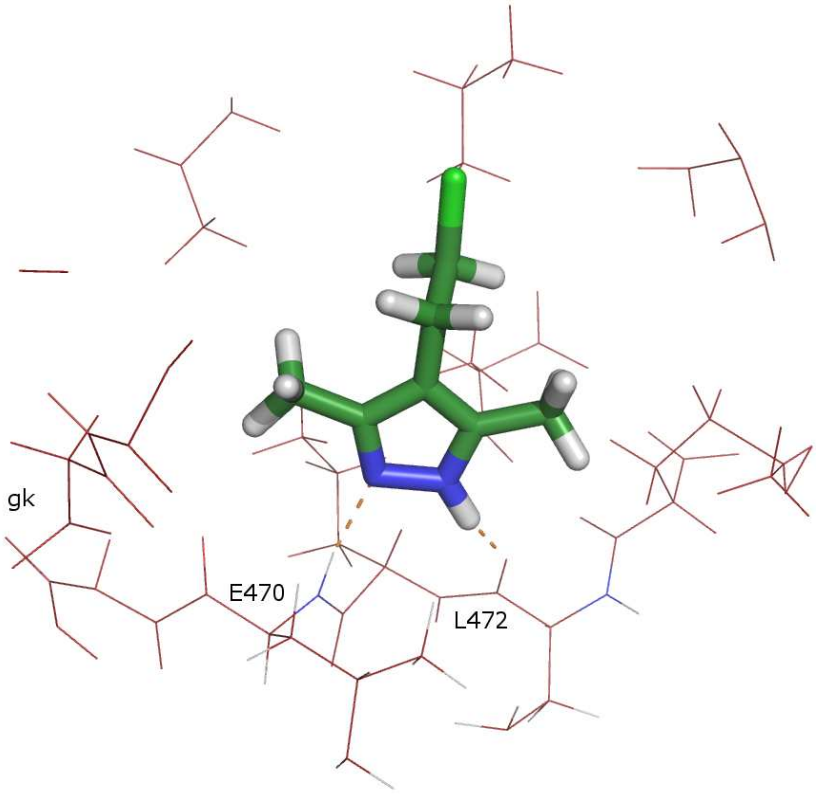

Figure 56: Docking of **47** on the ATP-binding cleft of NIK

We had chosen a strategy based on small molecules identification and offering possibilities of designing new hits by growing the lead chemical structure. As we identified two scaffolds endowed with good affinities with the hinge region of NIK, two possibilities exist to amplify rationally the potency of these series:

1. Linking: This first strategy identifies new fragments (by VS for example) endowed with high affinities with other regions of the ATP-binding site of NIK. Then every validated fragment is chemically linked to another to form a new original and specific inhibitor of NIK.

2. Evolution: This second strategy is based on a genetic algorithm working with a "trial and error approach" to increase the size and weight of the lead structure inside of the modeled binding cleft.

By building, validating and taking advantage of molecular modeling tools, we finally succeeded in discovering molecular fragments inhibiting NIK and the alternative pathway, both attractive targets for the treatment of RA.

Material and methods

1. Molecular modelling

1.1 Homology modelling

The human M3K14 (NIK) sequence was obtained from the Swiss-Prot database (primary accession number Q99558). Sequence alignment was performed using BLASTp,[104] through the Protein Data Bank (BLOSUM62 matrix).[105] The human PAK1 protein (PDB code 1YHW_A) was selected as the most appropriate template. Then, a consensus amino acid alignment and the 3D construction of the model was performed by *ESyPred3D*.[106] The quality of the model (including Ramachandran Plot) was analysed by means of PDBsum server.[162] To take into account protein flexibility, the resulting model was minimised using the *MINIMIZE* module included in *SYBYL 8.0* program.[108]

1.2 Docking simulations

Every compound evaluated in a docking study were built using the *SKETCH* module, as implemented in *SYBYL* (version 8.0),[108] and their geometry was optimised using *MINIMIZE* module. The minimisation process uses the *POWELL* method with the *TRIPOS* force field (dielectric constant 1*r*) to reach a final convergence of 0.01 kcal.mol^{-1}. Docking simulation was then performed (i) into the homology model of the human kinase NIK or (ii) into the 3D-structure of the kinase domain of TAK1,[128] with the automated *GOLD* program. Concerning NIK, the active site was defined including all residues in a volume of 7-10Å around 3-OH-staurosporine superimposed onto the model of NIK.

A similar procedure was used to dock **5c-d** inside the TAK1 binding cleft using the 3D-coordinates obtained from X-ray diffraction.[128] In the case of TAK1, the active site was defined by a sphere of 15Å around residue A107 in the active site.

2. Chemistry

Every reagents, products and solvents were purchased from ACROS ORGANICS, SIGMA-ALDRICH or MERCK EUROLAB.

^{1}H NMR spectra were recorded at 20°C in $CDCl_3$ or DMSO-d_6 on a 400 MHz Jeol Spectrometer (Jeol JNM EX-400). Chemical shifts are reported in δ ppm relative to tetramethylsilane (TMS) as a singlet at 0 ppm (δ). Thin-Layer Chromatography (TLC) was performed on aluminum supported 0.25 mm silica gel plates (Merck 5719, 250 meshes). TLC plates were visualized under 254 nm and 320 nm UV light. Elemental analyses (C, H, N) were performed on a Thermo Finnigan FlashEA 1112 apparatus. Mass spectra were recorded on an 1100 series MSD Trap spectrometer equipped with an electrospray ionisation (ESI) source. Flash chromatography purifications were performed on a Biotage SP1 Purification System using silica or C18 Biotage FLASH+® Cartridges. Microwave assisted reactions were performed using an Initiator 16 Single-mode Microwave system producing a 2.450 GHz controlled irradiation (Biotage AB, Uppsala). The temperature was measured with an IR sensor on the outside of the reaction vial.

Elemental micro analyses (C, H, N, S) were performed on a Thermo Finnigan FlashEA 1112 elemental analyser.

Purity of compounds **5a-d** was also confirmed by LC with an Agilent 1100 series system. System control, data collection and data processing were accomplished with the ChemStation software (Agilent Technologies, Santa Clara). The mobile phase contained acetonitrile and acetic acid (0.1%). Compounds were detected and their purity was calculated using a UV detector (wavelength λ = 240 nm). Two different methods were used to analyse the reported compounds. Method 1: injection volume = 3 µL in acetonitrile; gradient elution from 5% to 95% of acetonitrile over 2.4 min, then 95% acetonitrile until 3.6 min; analytical column C8 Zorbax Eclipse Plus (4.6 mm x 50 mm, 1.8 µm particle size); flow rate = 1.25 $mL.min^{-1}$; temperature = 40°C. Method 2: injection volume = 5 µL in acetonitrile; gradient elution from 5% to 95% of acetonitrile over 4.5 min, then 95% acetonitrile until 8.0 min; analytical column C18 Zorbax SB column (3.0 mm x 100 mm, 3.5 µm particle diameter); flow rate = 0.5 $mL.min^{-1}$; temperature = 40°C. Retention times were reported as Rt_1 and Rt_2 for these two methods respectively.

1-Phenylbutane-1,2,3-trione-2-oxime 7a - The titled compound is commercially available**.**

1,3-Diphenyl-propane-1,2,3-trione 2-oxime 7b - 240 mg (3.46 mmol) of sodium nitrite were dissolved in water (2 mL), and added dropwise to a solution of 130 mg (0.58 mmol) of dibenzoylmethane **6b** diluted into acetic acid (10 mL). At room temperature, the solution was stirred for 1 hour. The reaction mixture was extracted three times with diethyl ether (20 mL). The organic layers were combined and washed with a saturated aqueous solution of sodium bicarbonate (30 mL). Solvents were evaporated under reduced pressure, and the crude product purified by flash chromatography to give the title compound (Silica column; eluant AcOEt:cyclohexane with a gradient from 8% to 30% of AcOEt over 30 min; flow rate 40 mL/min). Yield: 81%.

^{1}H RMN ($CDCl_3$, 400 MHz): δ = 7.48-7.54 (m, 4H, H_{arom}), 7.63 (m, 2H, H_{arom}), 7.92 (d, *J* = 7.2 Hz, 2H, H_{arom}), 8.10 (d, *J* = 7.2 Hz, 2H, H_{arom}), 8.33 (s, 1H, OH). Anal. Calcul. for $C_{15}H_{11}NO_3$: C, 71.14; H, 4.38; N, 5.53. Found: C, 71.29; H, 4.62; N, 5.23. MS (ESI+) m/z 254.0 $[M+H]^+$, 276.1 $[M+Na]^+$

4-Amino-3-methyl-5-phenyl-1H-pyrazole 8a - At 0°C, hydrazine hydrate (0.18 mL, 3.70 mmol) was added dropwise to a solution of commercially available 1-phenylbutane-1,2,3-trione-2-oxime **7a** (0,37 mmol) in ethanol (4 mL). Then, the mixture was stirred for 7 hours at room temperature. Solvents were removed under reduced pressure and the crude product diluted in ethyl acetate (10 mL). The solution was acidified by HCl 3N (15 mL) and the organic layer discarded. The aqueous layer was neutralised by NaOH 1 N (50 mL) and extracted with ethyl acetate (3 x 20 mL). The organic layers were combined, dried on magnesium sulfate, and the solvent evaporated under reduced pressure. The crude product was purified by flash chromatography (Silica column; eluant: AcOEt:cyclohexane from 20% à 100% of AcOEt over 45 min; flow rate: 40 $mL.min^{-1}$). Yield: 86%. ^{1}H RMN ($CDCl_3$, 400 MHz): δ = 2.37 (s, 3H, CH_3), 7.31 (t, *J* = 7.6 Hz, 1H, H_{arom}), 7.42 (t, *J* = 7.6 Hz, 2H, H_{arom}), 7.61 (d, *J* = 7.6 Hz, 2H, H_{arom}). Anal. Calcul. for $C_{10}H_{11}N_3$: C, 69.34; H, 6.40; N, 24.26. Found: C, 69.30; H, 6.14; N, 23.56. MS (ESI+) m/z 174.1 $[M+H]^+$

4-Amino-3,5-diphenyl-1H-pyrazole 8b – The title compound was synthesised from 1,3-diphenyl-propane-1,2,3-trione 2-oxime **7b** and hydrazine hydrate with the same procedure than that used for **8a**. Yield: 88%. ^{1}H RMN ($CDCl_3$, 400 MHz): δ = 7.25 (t, *J* = 7.4 Hz, 2H, H_{arom}), 7.48 (t, *J* = 7.4 Hz, 4H, H_{arom}), 7.68 (d, *J* = 7.4 Hz, 4H, H_{arom}). Anal. Calcul. for $C_{15}H_{13}N_3$: C, 76.57; H, 5.57; N, 17.86. Found: C, 76.27; H, 5.65; N, 17.62. MS (ESI+) m/z 236.2 $[M+H]^+$

4-Benzamido-3,5-diphenyl-1H-pyrazole 10a - Benzoic acid **9a** (92.6 mmol), hydroxybenzotriazole (HOBt; 185 mmol) and *N*-(3-dimethylaminopropyl)-*N*'-ethylcarbodiimide (DEC; 79.5 mmol) were added to 4-amino-3,5-diphenyl-1H-pyrazole **8b** (92.6 mmol) diluted in dichloromethane (30 mL). Two drops of $BMimpF_6$ (1-butyl-3-methylimidazolium hexafluorophosphate) were added, and the mixture was heated in the microwave oven for 1 hour (70°C). Then, water (20 mL) was added and the mixture extracted by ethyl acetate (3 x 20 mL) The organic layers were combined, dried on magnesium sulfate, and the solvent evaporated under reduced pressure. The crude product was purified by flash chromatography (Silica column; Eluant: AcOEt:cyclohexane from 20% to 71% of AcOEt over 40 min; flowrate: 40 $mL.min^{-1}$). Yield: 60%.^{1}H RMN ($CDCl_3$, 400 MHz): δ = 7.28-7.46 (m, 6H, H_{arom}), 7.49 (t, *J* = 7.3 Hz, 2H, H_{arom}), 7.56 (t, *J* = 7.3 Hz, 1H, H_{arom}), 7.64 (d, *J* = 6.3 Hz, 2H, H_{arom}), 7.72 (d, *J* = 6.3 Hz, 2H, H_{arom}), 7.92 (d, *J* = 7.3 Hz, 2H, H_{arom}), 9.96 (s, 1H, HN_{amide}). Anal. Calcul. for $C_{22}H_{17}N_3O \cdot H_2O$: C, 73.93; H, 5.36; N, 11.76. Found: C, 74.03; H, 5.13; N, 11.42. MS (ESI+) m/z 340.2 $[M+H]^+$, 362.2 $[M+Na]^+$

4-(3-Methoxybenzamido)-3,5-diphenyl-1H-pyrazole 10b - The title compound was synthesised from 3-methoxybenzoic acid **9b** and 4-amino-3,5-diphenyl-1H-pyrazole **8b** as starting material, and according to the same procedure than that described for **10a.** Yield: 60%. ^{1}H RMN (DMSO- d_6, 400 MHz): δ = 3.77 (s, 3H, OCH_3), 7.12 (d, *J* = 8.2 Hz, 1H, H_{arom}), 7.26-7.45 (m, 8H, H_{arom}), 7.52 (d, *J* = 7.3 Hz, 1H, H_{arom}), 7.64 (d, *J* = 7.3 Hz, 2H, H_{arom}), 7.72 (d, *J* = 7.3 Hz, 2H, H_{arom}), 9.94 (s, 1H, HN). Anal. Calcul. for $C_{23}H_{17}N_3O$: C, 78.61; H, 4.88; N, 11.96; C, 78.04; H, 5.19; N, 11.58. MS (ESI+) m/z 369.2 $[M+H]^+$, 391.3 $[M+Na]^+$

4-(3-Methoxybenzamido)-3-methyl-5-phenyl-1H-pyrazole 10c - The title compound was synthesised from 3-methoxybenzoic acid **9b** and 4-amino-3-methyl-5-phenyl-1H-pyrazole **8a** as starting material, and according to the same procedure than that described for **10a.** Yield: 57%. ^{1}H RMN (DMSO-d_6, 400 MHz): δ = 2.08 (s, 3H, CH_3), 3.78 (s, 3H, OCH_3), 7.12 (d, *J* = 8.2 Hz, 1H, H_{arom}), 7.22-7.41 (m, 4H, H_{arom}), 7.49 (s, 1H, H_{arom}), 7.54 (d, *J* = 7.5 Hz, 1H, H_{arom}), 7.6-7.7 (m, 2H, H_{arom}), 9.69 (s, 1H, HN). Anal. Calcul. for $C_{18}H_{17}N_3O_2$: C, 70,34; H, 5,58; N, 13,67. Found: C, 70,51; H, 5,35; N, 13,36. MS (ESI+) m/z 308.2 $[M+H]^+$.

4-Benzamido-3-methyl-5-phenyl-1H-pyrazole 10d - The title compound was synthesised from benzoic acid **9a** and 4-amino-3-methyl-5-phenyl-1H-pyrazole **8a** as starting material, and according to the same procedure than that described for **10a.** Yield: 75%. ^{1}H RMN ($CDCl_3$, 400 MHz): δ = 2.26 (s, 3H, CH_3), 7.34-7.51 (m, 6H, H_{arom}), 7.61 (d, *J* = 8.2 Hz, 2H, H_{arom}), 7.71 (d, *J* = 7.5 Hz, 1H, H_{arom}), 7.83 (d, *J* = 8.2 Hz, 1H, H_{arom}). Anal. Calcul. for $C_{17}H_{15}N_3O \cdot 1/2\ H_2O$: C, 71.31; H, 5.63; N, 14.68. Found: C, 72.07; H, 5.33; N, 14.53. MS (ESI+) m/z 278.1 $[M+H]^+$

3,5-Diphenyl-1H-pyrazolo[4,3-*c*]isoquinoline 5a – 4-Benzamido-3,5-diphenyle-1H-pyrazole **10a** (0.36 mmol) and phosphorus pentoxyde (3.60 mmol) were suspended in dry chlorobenzene (10 mL) containing *N*,*N*-diethylaniline (0.36 mmol). Under argon atmosphere, the mixture was warmed up to 120°C and phosphorus oxychloride (0.54 mmol) was added dropwise. The temperature was maintained for 24 hours. At the end, a saturated solution of sodium bicarbonate (10 mL) was carefully added, and the mixture was extracted by dichloromethane (3 x 20 mL). The organic layers were combined, dried on magnesium sulfate and the solvents was evaporated under reduced pressure. The crude product was purified by preparative HPLC (C18 column and isocratic mobile phase MeCN:AcOH

0,1% 50:50) to give the title compound **5a**. Yield: 2%. m/z 340.2 $[M+H]^+$, 362.2 $[M+Na]^+$. ^1H RMN ($CDCl_3$, 400 MHz): δ = 7.35 (t, *J* = 7.5, 1H, H_{arom}), 7.46-7.71 (m, 9H, H_{arom}), 7.97 (t, *J* = 8.2 Hz, 1H, H_{arom}), 8.04 (d, *J* = 7.5 Hz, 1H, H_{arom}), 8.51 (d, *J* = Hz, 2H, H_{arom}). Rt_1 = 3.35 min; Rt_2 = 7.49 min. MS (ESI+) m/z 352.2 $[M+H]^+$.

5-(3-Methoxyphenyl)-3-phenyl-1H-pyrazolo[4,3-*c*]isoquinoline 5b - The title compound was synthesised from 4-(3-methoxybenzamido)-3,5-diphenyl-1H-pyrazole **10b** as starting material and according to the procedure described for compound **5a**. Yield: 7%. ^1H RMN ($CDCl_3$, 400 MHz): δ = 3.81(s, 3H, OCH_3), 7.11 (dd, J_1 = 2.2 Hz, J_2 = 8.1Hz, 1H, H_{arom}), 7.20-7.24 (m, 1H, H_{arom}), 7.21 (d, *J* = 2.2 Hz, 1H, H_{arom}), 7.35 (t, *J* = 7.3 Hz, 1H, H_{arom}), 7.46-7.50 (m, 3H, H_{arom}), 7.70 (t, *J* = 7.7 Hz, 1H, H_{arom}), 7.95 (t, *J* = 7.7 Hz, 1H, H_{arom}) 8.06 (d, *J* = 8.4 Hz, 1H, H_{arom}), 8.52-8.50 (m, 3H, H_{arom}). Rt_1 = 3.30 min; Rt_2 = 7.38 min. MS (ESI+) m/z 352.2 $[M+H]^+$.

5-(3-Methoxyphenyl)-3-methyl-1H-pyrazolo[4,3-*c*]isoquinoline 5c - The title compound was obtained from 4-(3-methoxybenzamido)-3-methyl-5-phenyl-1H-pyrazole **10c** as starting material and according to the procedure described for compound **5a**. Yield: 6%. ^1H RMN ($CDCl_3$, 400 MHz): δ = 2.76 (s, 3H, CH3), 3.87 (s, 3H, OCH3), 7.03 (d, *J* = 10.8 Hz, 1H, H_{arom}), 7.21-7.28 (m, 2H, H_{arom}), 7.44 (t, *J* = 12.1 Hz, 1H, H_{arom}), 7.59 (t, *J* = 10.8 Hz, 1H, H_{arom}), 7.81 (t, *J* = 10.8 Hz, 1H, H_{arom}), 8.13 (d, *J* = 12.1 Hz, 1H, H_{arom}), 8.22 (d, *J* = 12.1 Hz, 1H, H_{arom}). Rt_1 = 2.78 min; Rt_2 = 6.15 min. MS (ESI+) m/z 289.3 $[M+H]^+$.

3-Methyl-5-phenyl-1H-pyrazolo[4,3-*c*]isoquinoline 5d - The title compound was synthesised from 4-benzamido-3-methyl-5-phenyl-1H-pyrazole **10d** as starting material and according to the procedure described for compound **5a**. Yield: 13%. ^1H RMN ($CDCl_3$, 400 MHz): δ = 2.76 (s, 3H,

CH3), 7.51-7.60 (m, 4H, H_{arom}), 7.68 (d, *J* = 7.5 Hz, 2H, H_{arom}), 7.78 (t, *J* = 7.5 Hz, 1H, H_{arom}), 8.10 (d, *J* = 8.5 Hz, 1H, H_{arom}), 8.22 (d, *J* = 7.5 Hz, 1H, H_{arom}). Rt_1 = 2.78 min; Rt_2 = 6.15 min. MS (ESI+) m/z 260.1 $[M+H]^+$.

3-Oxo-2-phenyl-propionitrile 14a - The benzylcyanide **12** (87,2 mmol) was added to the ethyl formiate ester **13a** (104,6 mmol) and the mixture was stirred at room temperature. A solution of sodium ethanolate in ethanol 21% (165,6 mmol) was then added and the reaction was stirred for one minute at room temperature. The organic layer was extracted with dichloromethane (3 x 20 mL), acidified (HCl 3N, 4 mL), washed with a saturated solution of sodium bicarbonate (10 mL) and dried on magnesium sulfate. Solvants were finally removed under reduced pressure and the product was purified by crystallisation of methanol (4 mL). Yield: 44%. Anal. Calcul. for C_9H_7NO: C, 74.47; H, 4.86; N, 9.65. Found: C, 75.53; H, 4.54; N, 9.33. MS (ESI+) m/z 146.2 $[M+H]^+$.

3-Oxo-2-phenyl-butyronitrile 14b - The title compound is commercially available

3-Oxo-2-phenyl-pentanenitrile 14c - The title compound was prepared from ethyl propionate ester **13c** and benzylcyanide **12** as starting material and according to the procedure described for compound **14a**. Yield: 44% ^1H RMN (DMSO-d_6, 400 MHz): δ = 1.21 (t, *J* = 7.6 Hz, 3H, CH3), 2.57 (q, *J* = 7.6 Hz, 2H, CH2), 7.17 (t, *J* = 7.4 Hz, 1H, H_{arom}), 7.32 (t, *J* = 7.4 Hz, 2H, H_{arom}), 7.58 (d, *J* = 7.4 Hz, 2H, H_{arom}), 11.00 (s, 0.1H, CHCN), 11.52 (s, 0.9H, CHCN). Anal. Calcul. for $C_{11}H_{11}NO$: C, 76,28; H, 6,40; N, 8,09. Found: C, 77.02; H, 6,33; N, 8,37.

2,5-Dimethyl-4-phenyl-2H-pyrazol-3-ylamine 15a - 3-Oxo-2-phenyl-butyronitrile **14b** (2,0 g) was diluted in ethanol (8 mL). Methylhydrazine

(13,8 mmol) was then added at room temperature. The reaction was vigorously stirred under micro waves at 100°C during 20 minutes. The reaction was followed by TLC (AcOEt: cyclohexane 1:1). Solvents and hydrazine excess were the removed from the reaction mixture under reduced pressure. The crude product was diluted into ethyle acetate (5 mL) and acidified with HCl 3N (5 mL). Organic layer is discarded and aquous layer was neutralised by NaOH 1N (15 mL) and extracted with AcOEt (3 x 20 mL). The organic layers are combined and dried on Na_2SO_4. Finally, solvents were removed under reduced pressure. Crude product was purified by flash chromatography (normal phase on silica cartridge; mobile phase:AcOEt:cyclohexane with a gradient from 5% to 90% of AcOEt; duration: 30 min.). Yield: 60%. Anal. Calcul. for $C_{11}H_{13}N_{3:}$ C, 70,56; H, 7,00; N, 22,44. Found: C, 72,00; H, 6,78; N, 22,26.

3-Amino-5-methyl-4-phenyl-2H-pyrazole 15b - The title compound was prepared from 3-oxo-2-phenyl-butyronitrile **14b** and hydrazine hydrate according to the procedure described for compound **15a**. Yield: 42%. ^{1}H RMN ($CDCl_3$, 400 MHz): δ = 2.31 (s, 3H, CH3), 3.76 (s, 2H, NH_2), 7.26 (t, *J* = 7.3 Hz, 1H, H_{arom}), 7.35 (d, *J* = 7.3 Hz, 2H, H_{arom}), 7.41 (t, *J* = 7.3 Hz, 2H, H_{arom}). Anal. Calcul. for $C_{10}H_{11}N_3$: C, C, 69,34; H, 6,40; N, 24,26. Found: C, 70.69; H, 6.22; N, 24.12.

3-Amino-4-phenyl-2H-pyrazole 15c - The title compound was prepared from 3-oxo-2-phenyl-propionitrile **14a** and hydrazine hydrate according to the procedure described for compound **15a**. Yield: 37%. ^{1}H RMN ($CDCl_3$, 400 MHz): δ = 3.65 (s, 2H, NH_2), 7.24-7.75 (m, 5H, H_{arom}). MS (ESI+) m/z 160.1 $[M+H]^+$.

3-Amino-2-methyl-4-phenyl-2H-pyrazole 15d - The title compound was prepared from 3-oxo-2-phenyl-propionitrile **14a** and methylhydrazine

according to the procedure described for compound **15a**. Yield: 63% Anal. Calcul. for $C_{16}H_{15}N_3$: C, 78.74; H, 5.05; N, 16,02. Found: C, 78.74; H, 5.21; N, 15.31. MS (ESI+) m/z 260.1 $[M+H]^+$.

3-Amino-5-ethyl-2-methyl-4-phenyl-2H-pyrazole 15e - The title compound was prepared from 3-oxo-2-phenyl-pentanenitrile **14c** and methylhydrazine according to the procedure described for compound **15a**. Yield: 25% ^1H RMN ($CDCl_3$, 400 MHz): δ = 1.15 (t, *J* = 7.6 Hz, 3H, CH_3), 2.64 (q, *J* = 7.6 Hz, 2H, CH_2), 3.54 (s, 2H, NH_2) 3.67 (s, 3H, CH_3), 7.23-7.28 (m, 3H, H_{arom}), 7.40 (t, *J* = 7.7 Hz, 2H, H_{arom}). MS (ESI+) m/z 202.1 $[M+H]^+$.

3-Amino-5-ethyl-4-phenyl-2H-pyrazole 15f - The title compound was prepared from 3-oxo-2-phenyl-pentanenitrile **14c** and hydrazine hydrate according to the procedure described for compound **15a**. Yield: 37%. ^1H RMN ($CDCl_3$, 400 MHz): δ = 1.15 (t, *J* = 7.7 Hz, 3H, CH_3), 2.62 (q, *J* = 7.7 Hz, 2H, CH_2), 3.72 (s, 2H, NH_2), 7.27 (t, *J* = 7.1 Hz, 1H, H_{arom}), 7.34 (d, *J* = 7.1 Hz, 2H, H_{arom}), 7.40 (t, *J* = 7.1 Hz, 2H, H_{arom}).

3-Amino-5-methyl-4-phenyl-2-pyridin-2-yl-2H-pyrazole 15g - The title compound was prepared from 3-oxo-2-phenyl-butyronitrile **14b** and 2-pyridylhydrazine according to the procedure described for compound **15a**. Yield: 99%. ^1H RMN ($CDCl_3$, 400 MHz): δ = 2.14 (s, 3H, CH3), 3.26 (s, 2H, NH_2), 6.63 (d, *J* = 25.2 Hz, 2H, H_{arom}), 7.14 (d, *J* = 25.2 Hz, 2H, H_{arom}), 7.31-7.35 (m, 3H, H_{arom}), 7.80-7.85 (m, 2H, H_{arom}). Anal. Calcul. for $C_{15}H_{14}N_4$: C, 71,98; H, 5,64; N, 22,38. Found: C, 72.57; H, 5,60; N, 22,83. MS (ESI+) m/z 252.1 $[M+H]^+$.

3-Amino-5-methyl-2,4-diphenyl-2H-pyrazole 15h - The title compound was prepared from 3-oxo-2-phenyl-butyronitrile **14b** and phenylhydrazine

according to the procedure described for compound **15a**. Yield: 80%. Anal. Calcul. for $C_{16}H_{15}N_3$: C, 77,08; H, 6,06; N, 16,85. Found: C, 77,79; H, 6,06; N, 16,73. ^1H RMN (DMSO-d_6, 400 MHz): δ = 2.14 (s, 3H, CH3), 5.05 (s, 2H, NH_2), 7.20 (t, *J* = 7.2 Hz, 1H, H_{arom}), 7.27-7.41 (m, 5H, H_{arom}), 7.46 (t, *J* = 8.0 Hz, 2H, H_{arom}), 7.58 (d, *J* = 8.0 Hz, 2H, H_{arom}). Anal. Calcul. for $C_{15}H_{14}N_4$: C, 71,98; H, 5,64; N, 22,38. Found: C, 72.57; H, 5,60; N, 22,83. MS (ESI+) m/z 251.1 $[M+H]^+$.

1,3-Dimethyl-5-phenyl-3H-pyrazolo[3,4-*c*]isoquinoline 11a - Benzaldehyde **16a** (1,48mmol) is added to 3-amino-2,5-dimethyl-4-phenyl-2H-pyrazole **15a** (1,34 mmol) diluted in methanesulfonic acid (2 mL) with 2 drops of $BMimpF_6$. The reaction mixture is stirred under micro waves at 150°C for 15 minutes. The reaction is followed by TLC (AcOEt:cyclohexane 1:1). The mixture was then neutralised by addition of sodium hydroxide 1N (3 mL), extracted with ethyl acetate (3 x 10 mL) and dried on magnesium sulfate. Solvents were evaporated under reduced pressure and the crude product was purified by flash chromatography (inverse phase on C18 cartridge; mobile phase: water/MeCN with a gradient from 5% to 90% of MeCN for 30min). Yield: 18%. ^1H RMN ($CDCl_3$, 400 MHz): δ = 2.88 (s, 3H, CH3), 4.19 (s, 3H, NCH3), 7.44 (t, *J* = 7.9 Hz, 1H, H_{arom}), 7.52-7.85 (m, 3H, H_{arom}), 7.71 (d, *J* = 7.8 Hz, 2H, H_{arom}), 7.80 (t, *J* = 7.9 Hz, 1H, H_{arom}), 8.12 (d, *J* = 7.9 Hz, 1H, H_{arom}), 8.33 (d, *J* = 7.9 Hz, 1H, H_{arom}). MS (ESI+) m/z 274.2 $[M+H]^+$.

1-Methyl-5-phenyl-3H-pyrazolo[3,4-*c*]isoquinoline 11b - The title compound was prepared from 3-amino-5-methyl-4-phenyl-2H-pyrazole **15b** and benzaldehyde **16a** according to the procedure described for compound **11a**. Yield: 6%. ^1H RMN ($CDCl_3$, 400 MHz): δ = 2.91 (s, 3H, CH3), 7.46-7.56 (m, 4H, H_{arom}), 7.70 (d, *J* = 7.8 Hz, 2H, H_{arom}), 7.83 (t, *J* = 7.9 Hz, 1H, H_{arom}), 8.16 (d, *J* = 7.9 Hz, 1H, H_{arom}), 8.36 (d, *J* = 7.9 Hz, 1H, H_{arom}). Anal.

Calcul. for $C_{17}H_{13}N_3$: C, 78,74; H, 5,05; N, 16,20. Found: C, 77.85; H, 5.09; N, 15.86.

5-Phenyl-3H-pyrazolo[3,4-*c*]isoquinoline 11c - The title compound was prepared from 3-amino-4-phenyl-2H-pyrazole **15c** and benzaldehyde **16a** according to the procedure described for compound **11a**. Yield: 55%. ^{1}H RMN ($CDCl_3$, 400 MHz): δ = 7.50 (t, *J* = 8.5 Hz, 1H, H_{arom}), 7.54-7.60 (m, 3H, H_{arom}), 7.73 (d, *J* = 8.1 Hz, 2H, H_{arom}), 7.83 (t, *J* = 8.1 Hz, 1H, H_{arom}), 8.16 (d, *J* = 8.1 Hz, 1H, H_{arom}), 8.29 (d, *J* = 8.1 Hz, 1H, H_{arom}), 8.45 (s, 1H, $H_{1\text{-pyrazole}}$), 11.19 (s, 1H, NH).

5-(3-Hydroxyphenyl)-1,3-dimethyl-3H-pyrazolo[3,4-*c*]isoquinoline 11d - The title compound was prepared from 3-amino-2,5-dimethyl-4-phenyl-2H-pyrazole **15a** and 3-hydroxybenzaldehyde **16b** according to the procedure described for compound **11a**. Yield: 7%. ^{1}H RMN (DMSO-d_6, 400 MHz): δ = 2.76 (s, 3H, CH3), 4.03 (s, 3H, NCH3), 6.92 (d, *J* = 7.4 Hz, 1H, H_{arom}), 7.02 (s, 1H, H_{arom}), 7.03 (d, *J* = 7.4 Hz, 1H, H_{arom}), 7.34 (t, *J* = 7.8 Hz, 1H, H_{arom}), 7.52 (t, *J* = 7.8 Hz, 1H, H_{arom}), 7.88 (t, *J* = 7.4 Hz, 1H, H_{arom}), 8.04 (d, *J* = 7.8 Hz, 1H, H_{arom}), 8.34 (d, *J* = 7.8 Hz, 1H, H_{arom}), 9.68 (s, 1H, OH). Anal. Calcul. for $C_{18}H_{15}N_3O$: C, 74,72; H, 5,23; N, 14,52. Found: C, 72.51; H, 5,01; N, 13.11.

3-Methyl-5-phenyl-3H-pyrazolo[3,4-*c*]isoquinoline 11e - The title compound was prepared from 3-amino-2-methyl-4-phenyl-2H-pyrazole **15d** and benzaldehyde **16a** according to the procedure described for compound **11a**. Yield: 4%. ^{1}H RMN ($CDCl_3$, 400 MHz): δ = 4.26 (s, 3H, NCH3), 7.44 (t, *J* = 7.9 Hz, 1H, H_{arom}), 7.52-7.61 (m, 3H, H_{arom}), 7.72 (d, *J* = 8.1 Hz, 2H, H_{arom}), 7.79 (t, *J* = 7.9 Hz, 1H, H_{arom}), 8.11 (d, *J* = 7.9 Hz, 1H, H_{arom}), 8.24 (d, *J* = 7.9 Hz, 1H, H_{arom}), 8.37 (s, 1H, $H_{1\text{-pyrazole}}$).

5-(3-Hydroxyphenyl)-1-methyl-3H-pyrazolo[3,4-*c*]isoquinoline 11f - The title compound was prepared from 3-amino-5-methyl-4-phenyl-2H-pyrazole **15b** and 3-hydroxybenzaldehyde **16b** according to the procedure described for compound **11a**. Yield: 3%. ^{1}H RMN (DMSO-d_6, 400 MHz): δ = 2.77 (s, 3H, CH3), 6.91 (d, *J* = 7.4 Hz, 1H, H_{arom}), 7.01 (s, 1H, H_{arom}), 7.02 (d, *J* = 7.4 Hz, 1H, H_{arom}), 7.34 (t, *J* = 7.8 Hz, 1H, H_{arom}), 7.52 (t, *J* = 7.8 Hz, 1H, H_{arom}), 7.87 (t, *J* = 7.4 Hz, 1H, H_{arom}), 8.05 (d, *J* = 7.8 Hz, 1H, H_{arom}), 8.35 (d, *J* = 7.8 Hz, 1H, H_{arom}), 9.66 (s, 1H, OH). Anal. Calcul. for $C_{16}H_{11}N_3O$: C, 73,55; H, 4,24; N, 16,08. Found: 72.94; H, 4.60; N, 14.20.

5-(3-Hydroxyphenyl)-3H-pyrazolo[3,4-*c*]isoquinoline 11g - The title compound was prepared from 3-amino-4-phenyl-2H-pyrazole **15c** and 3-hydroxybenzaldehyde **16b** according to the procedure described for compound **11a**. Yield: 4%. ^{1}H RMN (DMSO-d_6, 400 MHz): δ = 6.92 (d, *J* = 7.4 Hz, 1H, H_{arom}), 7.05 (s, 1H, H_{arom}), 7.06 (d, *J* = 7.4 Hz, 1H, H_{arom}), 7.34 (t, *J* = 7.8 Hz, 1H, H_{arom}), 7.52 (t, *J* = 7.8 Hz, 1H, H_{arom}), 7.85 (t, *J* = 7.4 Hz, 1H, H_{arom}), 8.25 (d, *J* = 7.8 Hz, 1H, H_{arom}), 8.41 (d, *J* = 7.8 Hz, 1H, H_{arom}), 8.59 (s, 1H, NH), 9.67 (s, 1H, OH). Anal. Calcul. for $C_{16}H_{11}N_3O$: C, 73,55; H, 4,24; N, 16,08; O, 6,12. Found: 73,55; H, 4,07; N, 15.60.

1-Ethyl-3-methyl-5-phenyl-3H-pyrazolo[3,4-*c*]isoquinoline 11h - The title compound was prepared from 3-amino-5-ethyl-2-methyl-4-phenyl-2H-pyrazole **15e** and benzaldehyde **16a** according to the procedure described for compound **11a**. Yield: 14%. ^{1}H RMN ($CDCl_3$, 400 MHz): δ = 1.51 (t, *J* = 7.4 Hz, 3H, CH_3), 3.29 (q, *J* = 7.4 Hz, 2H, CH_2), 4.20 (s, 3H, NCH_3), 7.44 (t, *J* = 7.8 Hz, 1H, H_{arom}), 7.52-7.57 (m, 3H, H_{arom}), 7.71 (d, *J* = 6.4 Hz, 2H, H_{arom}), 7.81 (t, *J* = 7.8 Hz, 1H, H_{arom}), 8.12 (d, *J* = 7.8 Hz, 1H, H_{arom}), 8.29 (d, *J* = 7.8 Hz, 1H, H_{arom}). Anal. Calcul. for $C_{19}H_{17}N_3$: C, 79.41; H, 5.96; N, 14.62. Found: C, 79.24; H, 5.86; N, 14.08.

1-Ethyl-5-phenyl-3H-pyrazolo[3,4-*c*]isoquinoline 11i - The title compound was prepared from 3-amino-5-ethyl-4-phenyl-2H-pyrazole **15f** and benzaldehyde **16a** according to the procedure described for compound **11a**. Yield: 9%. ^{1}H RMN ($CDCl_3$, 400 MHz): δ = 1.51 (t, *J* = 7.7 Hz, 3H, CH_3), 3.32 (q, *J* = 7.7 Hz, 2H, CH_2), 7.47-7.57 (m, 4H, H_{arom}), 7.69 (d, *J* = 6.6 Hz, 2H, H_{arom}), 7.81 (t, *J* = 7.6 Hz, 1H, H_{arom}), 8.16 (d, *J* = 7.6 Hz, 1H, H_{arom}), 8.33 (d, *J* = 7.6 Hz, 1H, H_{arom}).

5-(3-Methoxy-phenyl)-1-methyl-3H-pyrazolo[3,4-*c*]isoquinoline 11j - The title compound was prepared from 3-amino-5-methyl-4-phenyl-2H-pyrazole **15b** and 3-methoxybenzaldehyde **16c** according to the procedure described for compound **11a**. Yield: 1%.^{1}H RMN ($CDCl_3$, 400 MHz): δ = 2.91 (s, 3H, CH_3), 3.88 (s, 3H, OCH_3), 7.07 (dd, J_1 = 8.5 Hz, J_2 = 2.1 Hz, 1H, H_{arom}), 7.23-7.27 (m, 2H, H_{arom}), 7.44-7.50 (m, 2H, H_{arom}), 7.83 (t, *J* = 7.7 Hz, 1H, H_{arom}), 8.18 (d, *J* = 8.2 Hz, 1H_{arom}), 8.36 (d, *J* = 8.2 Hz, 1H_{arom}), 10.69 (s, 1H, NH).

1-Methyl-5-phenyl-3-pyridin-2-yl-3H-pyrazolo[3,4-*c*]isoquinoline 11k - The title compound was prepared from 3-amino-5-methyl-4-phenyl-2-pyridin-2-yl-2H-pyrazole **15g** and benzaldehyde **16a** according to the procedure described for compound **11a**. Yield: 60%. ^{1}H RMN ($CDCl_3$, 400 MHz): δ = 3.04 (s, 3H, CH_3), 7.07 (dd, J_1 = 6.9 Hz, J_2 = 5.0 Hz, 1H, H_{arom}), 7.25-7.59 (m, 4H, H_{arom}), 7.78 (d, *J* = 7.6 Hz, 2H, H_{arom}), 7.87 (q, *J* = 8.2 Hz, 2H, H_{arom}), 8.24 (d, *J* = 8.2 Hz, 1H, H_{arom}), 8.44 (d, *J* = 8.2 Hz, 1H, H_{arom}), 8.66 (d, *J* = 5.0 Hz, 1H, H_{arom}), 8.74 (d, *J* =8.2 Hz, 1H, H_{arom}). Anal. Calcul. for $C_{22}H_{16}N_4$: C, 78.55; H, 4.79; N, 16.66. Found: C, 78.49; H, 4.89; N, 16.01.

1-Methyl-3,5-diphenyl-3H-pyrazolo[3,4-*c*]isoquinoline 11l - The title compound was prepared from 3-amino-5-methyl-2,4-diphenyl-2H-pyrazole

15h and benzaldehyde **16a** according to the procedure described for compound **11a**. Yield: 11%. ^{1}H RMN ($CDCl_3$, 400 MHz): δ = 2.99 (s, 3H, CH_3), 7.47-7.57 (m, 7H, H_{arom}), 7.77 (d, *J* = 7.8 Hz, 2H, H_{arom}), 7.85 (t, *J* = 7.8 Hz, 1H, H_{arom}), 8.22 (d, *J* = 8.5 Hz, 1H, H_{arom}), 8.34 (d, *J* = 8.5 Hz, 2H, H_{arom}), 8.41 (d, *J* = 8.5 Hz, 1H, H_{arom}). Anal. Calcul. for $C_{23}H_{17}N_3$: C, 82.36; H, 5.11; N, 12.53. Found: C, 82.48; H, 5.27; N, 11.95.

3,5-Dimethyl-4-propyl-1H-pyrazole 48 - 1,8-Diazabicyclo[5.4.0]undec-7-ene (97.4 mmol) was added to a solution of 2,4-pentanedione (97.4 mmol) in *tert*-butyl methyl ether (25 mL) and toluene (10 mL). Iodopropane (97.4 mmol) was added and the mixture was stirred at room temperature for 5 hours. Solvents were removed under reduced pressure and the crude product was diluted into EtOH (25 mL). Then, the hydrazine hydrate (97.4 mmol) was added and the reaction mixture was stirred overnight at room temperature. Solvents were evaporated under reduced pressure. The organic layer was separated by AcOEt (3x 100 mL) after acidification (pH = 5) by a formic acid solution 1N (60 mL), dried on Na_2SO_4 and solvents were removed under reduced pressure. The title compound product crystallised from the crude residue (yellow oil) to give 240mg of 3,5-dimethyl-4-propyl-1H-pyrazole **48** isolated by filtration. Yield: 2%. ^{1}H RMN ($CDCl_3$, 400 MHz): δ = 0.87 (t, *J* = 7.4 Hz, 3H, CH_3), 1.45 (q, *J* = 7.4 Hz, 2H, CH_2), 2.20 (s, 6H, $(CH_3)_2$), 2.30 (t, *J* = 7.4 Hz, 3H, CH_2), 9.93 (s, 1H, NH). Anal. Calcul. for $C_{19}H_{17}N_3$: C, 69.52; H, 10.21; N, 20.27. Found: C, 69.83; H, 10.04; N, 19.94.

3. Biology

3.1 NIK enzymatic assay

This experiment was performed by ProQinase using the 33PanQinase® technology (Figure 57). Inhibitory potency of staurosporine **28** and molecules selected by VS were evaluated on human recombinant NIK. DMSO was used as cosolvent and its final concentration was 1%. NIK was expressed in Sf9 insect cells as human recombinant GST-fusion protein. The kinase was purified by affinity chromatography using GSH-agarose. The purity of the kinase was checked by SDS-PAGE/silver staining and the identity was verified by mass spectroscopy. The NIK activity was measured as the incorporation on an artificial substrate of ^{33}P produced by hydrolysis of [γ-^{33}P]-ATP.

The substrate (RBER-CHKtide) was an artificial fusion protein expressed in E.coli. It was consisting of a *N*-terminal GST-tag separated by a thrombin cleavage site from a fragment of the human retinoblastoma protein RB1, amino acids S773-K928 followed by 11 arginine residues (ER) and a peptide sequence: KKKVRSGLYRSPSMPENLNRPR (CHKtide).

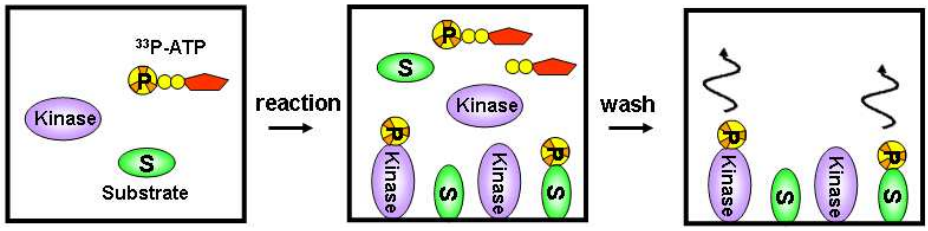

Figure 57: ProQinase *in vitro* enzymatic assay

All kinase assays were performed in 96-well FlashPlatesTM from Perkin Elmer (Boston, MA, USA) in a 50 µl reaction volume. The reaction cocktail was pipetted in 4 steps in the following order: (i) 20 µl of assay buffer; (ii) 5 µl of ATP solution (in H2O); (iii)5 µl of test compound (in 10 % DMSO); (iv) 10 µl of substrate / 10 µl of enzyme solution (premixed). The assay for NIK contained 60 mM HEPES-NaOH, pH 7.5, 3 mM MgCl2, 3 mM MnCl2, 3 µM Na-orthovanadate, 1.2 mM DTT, 50 µg/ml PEG20000, 1 µM [γ-^{33}P]-ATP (approx. 5 x 10^{05} cpm per well). The reaction cocktails were incubated at 30°C for 60 minutes. The reaction was stopped with 50 µl of 2 % (v/v) H_3PO_4, plates were aspirated and washed two times with 200 µl 0.9 % (w/v) NaCl. Incorporation of ^{33}Pi was determined with a microplate scintillation counter (Microbeta, Wallac).

The median value of the counts of each assay plate (n=8) was defined as "low control". This value reflects unspecific binding of radioactivity to the plate in the absence of a protein kinase but in the presence of the substrate. The median value of the counts of each assay plate (n=8) was taken as the "high control", *i.e.* full activity in the absence of any inhibitor. The difference between high and low control was taken as 100% activity. As part of the data evaluation the low control value from a particular plate was subtracted from the high control value as well as from all compound values of the corresponding plate. The residual activity (RA, in %) for each well was calculated by using the following formula:

RA (%) = 100 X [(cpm of compound – low control) / (high control – low control)]

3.2 NF-κB alternative pathway cellular assay

Human LTβR-positive HeLa cells were used to evaluate the NIK inhibitory potency expressed as the inhibition of the processing of p100 into

p52 (Figure 58). Briefly, HeLa cells were cultured in DMEM with 10% FBS and plated in 6 well plates until they reach 80% of confluence.

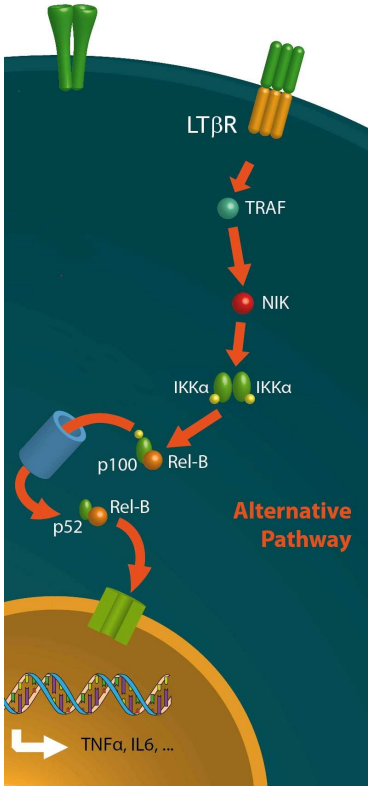

Figure 58: Alternative pathway activation assay

The cells were washed twice with PBS and incubated for 2 hours with Opimem-1 containing 10, 20 or 50 µM of inhibitor (pyrazoloisoquinolines or commercial compounds selected by the virtual screen). DMSO was used as cosolvent at a maximal concentration of 0.5% (v/v). At this concentration, DMSO has no effect. Then, an antibody acting as agonist of human LTβR (R&D Systems, Inc. / LIGHT) was added for 5 hours. Afterwards, the cells were washed twice with PBS and lysed in SDS

0.5% containing a cocktail of protease and phosphatase inhibitors (Complete and PhosStop, Roche). Protein extracts were quantified (Micro BCA protein kit assay, Pierce) and equal amounts of protein (15 µg) were loaded on SDS-PAGE for analysing the processing of p100 into p52. For detecting p100 and p52, an antibody anti-human p52 (Upstate Cell Signaling 05-361) was used and a goat anti-mouse HRP (DAKO) was used as secondary antibody prior to measurement of chemiluminescence using the ECL kit from Pierce.

3.3 Multikinase assay

This radiometric assay was performed by Millipore using the Kinase Profiler™ technology (Figure 59). Full protocols are available on the reported Millipore webpage.[e, 163]

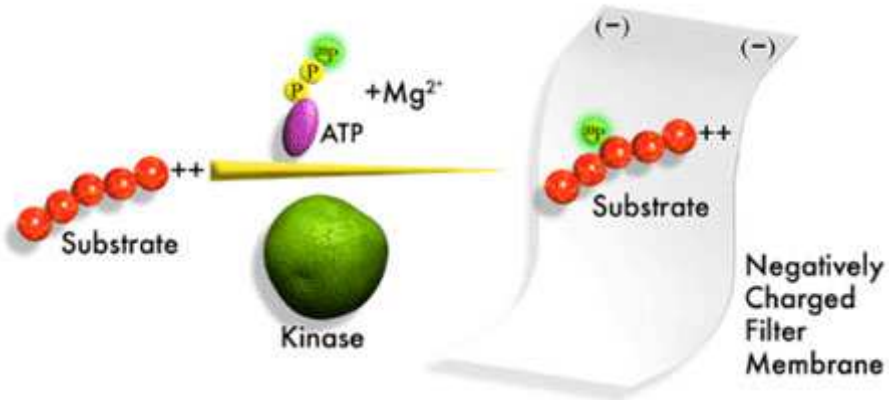

Figure 59: Millipore multikinase assay

[e] http://direct.millipore.com/techpublications/tech1/cd1000enus.

3.4 TAK1 enzymatic Assay

This experiment was performed by Invitrogen using LanthaScreen® Kinase Binding Assay technology (Figure 60).

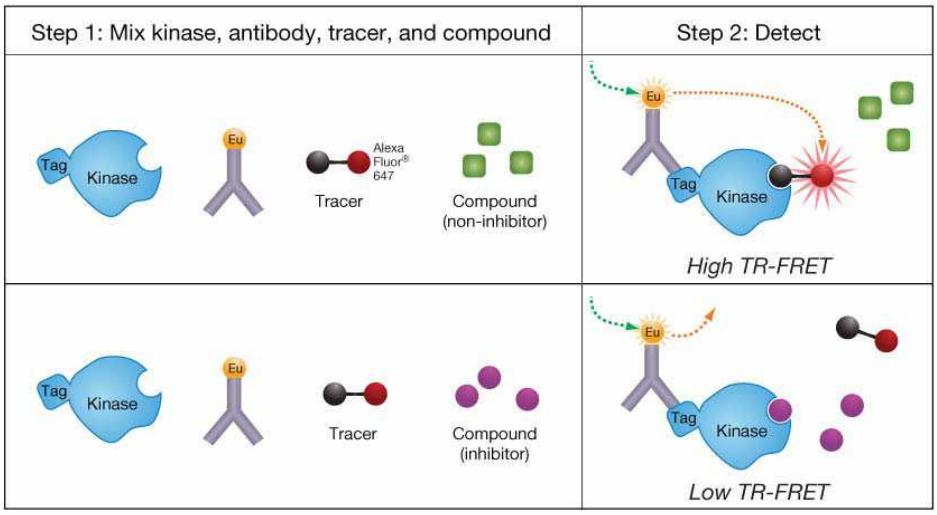

Figure 60: Schematic of LanthaScreen™ Eu Kinase Binding Assay

The tested compounds were screened in 1% DMSO as final concentration. Three-fold serial dilutions were conducted from the starting concentration. All kinase/Antibody mixtures were diluted to a 2X working concentration in the appropriate kinase buffer. The 4X AlexaFluor® (AF) labelled tracer was prepared in kinase buffer and the read out was on fluorescence plate reader. The AF/Europium emission ratio (665 nm and 615 nm respectively) were finally calculated.

3.5 NF-κB classical pathway cellular assay

HeLa cells were cultured in DMEM with 10% FBS and plated in 6-well plates until they reach 80% of confluence. The cells were washed twice with PBS and incubated for 2 hours with Opimem-1 containing 50 µM of inhibitor or DMSO alone. Then, TNF-α (Pepro Tech Inc.) was added at 100 U/mL for 0, 1 or 2 hours. Total RNA samples were isolated with the Tripure reagent (Roche Molecular Biochemicals). One microgram of RNA was submitted to reverse transcription using M-MLV reverse transcriptase and random primers (Invitrogen) in a total volume of 20 µL. Two microliters of cDNA were submitted to real-time PCR using TaqMan 7000 SDS (Applied Biosystems) and SYBR Green detection (Eurogentec). The results were normalised with the 18S transcript. PCR was performed with the following primers for the following human transcript :

il-6 : FW 5'-CCAGGAGCCCAGCTATGAAC-3'
and RV 5'-CCCAGGGAGAAGGCAACTG-3',
TNFα : FW 5'-GGAGAAGGGTGACCGACTCA-3'
and RV 5'-TGCCCAGACTCGGCAAAG-3',
18S : FW 5'-AACTTTCGATGGTAGTCGCCG-3'
and RV 5'- CCTTGGATGTGGTAGCCGTTT -3'.

3.6 Cell viability assay

HeLa cells were cultured in DMEM with 10% FBS and plated in 96 well plates until they reach 80% of confluence. The cells were washed twice with PBS and incubated for 6 hours with Opimem-1 containing 100, 50, 10 μM of inhibitors or DMSO alone. Cell viability assay was performed using CellTiter-Glo® luminescent cell viability assay (Promega) that determine the number of viable cells in culture. Detection was based on the luciferase reaction to measure the amount of ATP from viable cells. Briefly a volume of CellTiter-Glo® reagent equal to the volume of cell culture medium was added to each well and mixed for 2 minutes to induce cell lysis. The plate was incubated for 10 minutes at room temperature to stabilise the luminescent signal and, then, each well content was transferred in an opaque-walled multiwell. The luminescent signal was recorded using a 96 microplate luminometer.

References

(1) Lee, D. M.; Weinblatt, M. E. Rheumatoid arthritis. *Lancet* **2001**, *358*, 903-911.

(2) Feldmann, M.; Brennan, F. M.; Maini, R. N. Rheumatoid arthritis. *Cell* **1996**, *85*, 307-310.

(3) Gravallese, E. M.; Darling, J. M.; Ladd, A. L.; Katz, J. N.; Glimcher, L. H. In situ hybridization studies of stromelysin and collagenase messenger RNA expression in rheumatoid synovium. *Arthritis Rheum* **1991**, *34*, 1076-1084.

(4) McCachren, S. S.; Haynes, B. F.; Niedel, J. E. Localization of collagenase mRNA in rheumatoid arthritis synovium by in situ hybridization histochemistry. *J Clin Immunol* **1990**, *10*, 19-27.

(5) Saxne, T.; Palladino, M. A., Jr.; Heinegard, D.; Talal, N.; Wollheim, F. A. Detection of tumor necrosis factor alpha but not tumor necrosis factor beta in rheumatoid arthritis synovial fluid and serum. *Arthritis Rheum* **1988**, *31*, 1041-1045.

(6) Feldmann, M.; Brennan, F. M.; Maini, R. N. Role of cytokines in rheumatoid arthritis. *Annu Rev Immunol* **1996**, *14*, 397-440.

(7) Firestein, G. S.; Alvaro-Gracia, J. M.; Maki, R. Quantitative analysis of cytokine gene expression in rheumatoid arthritis. *J Immunol* **1990**, *144*, 3347-3353.

(8) Choy, E. H.; Panayi, G. S. Cytokine pathways and joint inflammation in rheumatoid arthritis. *N Engl J Med* **2001**, *344*, 907-916.

(9) Sweeney, S. E.; Firestein, G. S. Rheumatoid arthritis: regulation of synovial inflammation. *Int J Biochem Cell Biol* **2004**, *36*, 372-378.

(10) Firestein, G. S. Evolving concepts of rheumatoid arthritis. *Nature* **2003**, *423*, 356-361.

(11) Foxwell, B.; Browne, K.; Bondeson, J.; Clarke, C.; de Martin, R.; Brennan, F.; Feldmann, M. Efficient adenoviral infection with IkappaB alpha reveals

that macrophage tumor necrosis factor alpha production in rheumatoid arthritis is NF-kappaB dependent. *Proc Natl Acad Sci U S A* **1998**, *95*, 8211-8215.

(12) O'Dell, J. R. Therapeutic strategies for rheumatoid arthritis. *N Engl J Med* **2004**, *350*, 2591-2602.

(13) Whelton, A.; Maurath, C. J.; Verburg, K. M.; Geis, G. S. Renal safety and tolerability of celecoxib, a novel cyclooxygenase-2 inhibitor. *Am J Ther* **2000**, *7*, 159-175.

(14) Silverstein, F. E.; Faich, G.; Goldstein, J. L.; Simon, L. S.; Pincus, T.; Whelton, A.; Makuch, R.; Eisen, G.; Agrawal, N. M.; Stenson, W. F.; Burr, A. M.; Zhao, W. W.; Kent, J. D.; Lefkowith, J. B.; Verburg, K. M.; Geis, G. S. Gastrointestinal toxicity with celecoxib vs nonsteroidal anti-inflammatory drugs for osteoarthritis and rheumatoid arthritis: the CLASS study: A randomized controlled trial. Celecoxib Long-term Arthritis Safety Study. *Jama* **2000**, *284*, 1247-1255.

(15) Bombardier, C.; Laine, L.; Reicin, A.; Shapiro, D.; Burgos-Vargas, R.; Davis, B.; Day, R.; Ferraz, M. B.; Hawkey, C. J.; Hochberg, M. C.; Kvien, T. K.; Schnitzer, T. J. Comparison of upper gastrointestinal toxicity of rofecoxib and naproxen in patients with rheumatoid arthritis. VIGOR Study Group. *N Engl J Med* **2000**, *343*, 1520-1528, 1522 p following 1528.

(16) FitzGerald, G. A.; Patrono, C. The coxibs, selective inhibitors of cyclooxygenase-2. *N Engl J Med* **2001**, *345*, 433-442.

(17) McDougall, R.; Sibley, J.; Haga, M.; Russell, A. Outcome in patients with rheumatoid arthritis receiving prednisone compared to matched controls. *J Rheumatol* **1994**, *21*, 1207-1213.

(18) Saag, K. G.; Koehnke, R.; Caldwell, J. R.; Brasington, R.; Burmeister, L. F.; Zimmerman, B.; Kohler, J. A.; Furst, D. E. Low dose long-term corticosteroid therapy in rheumatoid arthritis: an analysis of serious adverse events. *Am J Med* **1994**, *96*, 115-123.

(19) Moreland, L. W.; O'Dell, J. R. Glucocorticoids and rheumatoid arthritis: back to the future? *Arthritis Rheum* **2002**, *46*, 2553-2563.

(20) Guidelines, A. C. o. R. S. o. R. A. Guidelines for the management of rheumatoid arthritis: 2002 Update. *Arthritis Rheum* **2002**, *46*, 328-346.

(21) Caporali, R.; Pallavicini, F. B.; Filippini, M.; Gorla, R.; Marchesoni, A.; Favalli, E. G.; Sarzi-Puttini, P.; Atzeni, F.; Montecucco, C. Treatment of rheumatoid arthritis with anti-TNF-alpha agents: a reappraisal. *Autoimmun Rev* **2009**, *8*, 274-280.

(22) van Vollenhoven, R. F. Treatment of rheumatoid arthritis: state of the art 2009. *Nat Rev Rheumatol* **2009**, *5*, 531-541.

(23) Weinblatt, M. E. Toxicity of low dose methotrexate in rheumatoid arthritis. *J Rheumatol Suppl* **1985**, *12 Suppl 12*, 35-39.

(24) Weinblatt, M. E.; Kaplan, H.; Germain, B. F.; Block, S.; Solomon, S. D.; Merriman, R. C.; Wolfe, F.; Wall, B.; Anderson, L.; Gall, E.; et al. Methotrexate in rheumatoid arthritis. A five-year prospective multicenter study. *Arthritis Rheum* **1994**, *37*, 1492-1498.

(25) Ortendahl, M.; Holmes, T.; Schettler, J. D.; Fries, J. F. The methotrexate therapeutic response in rheumatoid arthritis. *J Rheumatol* **2002**, *29*, 2084-2091.

(26) Choi, H. K.; Hernan, M. A.; Seeger, J. D.; Robins, J. M.; Wolfe, F. Methotrexate and mortality in patients with rheumatoid arthritis: a prospective study. *Lancet* **2002**, *359*, 1173-1177.

(27) O'Dell, J. R.; Haire, C. E.; Erikson, N.; Drymalski, W.; Palmer, W.; Eckhoff, P. J.; Garwood, V.; Maloley, P.; Klassen, L. W.; Wees, S.; Klein, H.; Moore, G. F. Treatment of rheumatoid arthritis with methotrexate alone, sulfasalazine and hydroxychloroquine, or a combination of all three medications. *N Engl J Med* **1996**, *334*, 1287-1291.

(28) Maini, R. N.; Breedveld, F. C.; Kalden, J. R.; Smolen, J. S.; Davis, D.; Macfarlane, J. D.; Antoni, C.; Leeb, B.; Elliott, M. J.; Woody, J. N.; Schaible, T. F.; Feldmann, M. Therapeutic efficacy of multiple intravenous infusions of anti-tumor necrosis factor alpha monoclonal antibody combined with low-dose weekly methotrexate in rheumatoid arthritis. *Arthritis Rheum* **1998**, *41*, 1552-1563.

(29) Olsen, N. J.; Stein, C. M. Drug therapy - New drugs for rheumatoid arthritis. *New Engl J Med* **2004**, *350*, 2167-2179.

(30) Jiang, Y.; Genant, H. K.; Watt, I.; Cobby, M.; Bresnihan, B.; Aitchison, R.; McCabe, D. A multicenter, double-blind, dose-ranging, randomized, placebo-controlled study of recombinant human interleukin-1 receptor antagonist in patients with rheumatoid arthritis: radiologic progression and correlation of Genant and Larsen scores. *Arthritis Rheum* **2000**, *43*, 1001-1009.

(31) Maini, R. N.; Taylor, P. C.; Szechinski, J.; Pavelka, K.; Broll, J.; Balint, G.; Emery, P.; Raemen, F.; Petersen, J.; Smolen, J.; Thomson, D.; Kishimoto, T.; Grp, C. S. Double-blind randomized controlled clinical trial of the interleukin-6 receptor antagonist, tocilizumab, in European patients with rheumatoid arthritis who had an incomplete response to methotrexate. *Arthritis Rheum* **2006**, *54*, 2817-2829.

(32) Emery, P.; Fleischmann, R.; Filipowicz-Sosnowska, A.; Schechtman, J.; Szczepanski, L.; Kavanaugh, A.; Racewicz, A. J.; Van Vollenhoven, R. F.; Li, N. F.; Agarwal, S.; Hessey, E. W.; Shaw, T. M.; Grp, D. S. The efficacy and safety of rituximab in patients with active rheumatoid arthritis despite methotrexate treatment - Results of a phase IIb randomized, double-blind, placebo-controlled, dose-ranging trial. *Arthritis Rheum* **2006**, *54*, 1390-1400.

(33) Cohen, S. B.; Emery, P.; Greenwald, M. W.; Dougados, M.; Furie, R. A.; Genovese, M. C.; Keystone, E. C.; Loveless, J. E.; Burmester, G. R.; Cravets, M. W.; Hessey, E. W.; Shaw, T.; Totoritis, M. C.; Grp, R. T. Rituximab for rheumatoid arthritis refractory to anti-tumor necrosis factor therapy - Results of a multicenter, randomized, double-blind, placebo-controlled, phase III trial evaluating primary efficacy and safety at twenty-four weeks. *Arthritis Rheum* **2006**, *54*, 2793-2806.

(34) Gupta, S.; Gollapudi, S. Molecular mechanisms of TNF-alpha-induced apoptosis in naive and memory T cell subsets. *Autoimmun Rev* **2006**, *5*, 264-268.

(35) Warris, A.; Bjorneklett, A.; Gaustad, P. Invasive pulmonary aspergillosis associated with infliximab therapy. *New Engl J Med* **2001**, *344*, 1099-1100.

(36) Kamath, B. M.; Mamula, P.; Baldassano, R. N.; Markowitz, J. E. Listeria meningitis after treatment with infliximab. *J Pediatr Gastr Nutr* **2002**, *34*, 410-412.

(37) Nakelchik, M.; Mangino, J. E. Reactivation of histoplasmosis after treatment with infliximab. *Am J Med* **2002**, *112*, 78-78.

(38) Lee, J. H.; Slifman, N. R.; Gershon, S. K.; Edwards, E. T.; Schwieterman, W. D.; Siegel, J. N.; Wise, R. P.; Brown, S. L.; Udall, J. N.; Braun, M. M. Life-threatening histoplasmosis complicating immunotherapy with tumor necrosis factor alpha antagonists infliximab and etanercept. *Arthritis Rheum* **2002**, *46*, 2565-2570.

(39) Kroesen, S.; Widmer, A. F.; Tyndall, A.; Hasler, P. Serious bacterial infections in patients with rheumatoid arthritis under anti-TNF-alpha therapy. *Rheumatology* **2003**, *42*, 617-621.

(40) Brown, S. L.; Greene, M. H.; Gershon, S. K.; Edwards, E. T.; Braun, M. M. Tumor necrosis factor antagonist therapy and lymphoma development: twenty-six cases reported to the Food and Drug Administration. *Arthritis Rheum* **2002**, *46*, 3151-3158.

(41) Moreland, L. W.; Schiff, M. H.; Baumgartner, S. W.; Tindall, E. A.; Fleischmann, R. M.; Bulpitt, K. J.; Weaver, A. L.; Keystone, E. C.; Furst, D. E.; Mease, P. J.; Ruderman, E. M.; Horwitz, D. A.; Arkfeld, D. G.; Garrison, L.; Burge, D. J.; Blosch, C. M.; Lange, M. L.; McDonnell, N. D.; Weinblatt, M. E. Etanercept therapy in rheumatoid arthritis. A randomized, controlled trial. *Ann Intern Med* **1999**, *130*, 478-486.

(42) Maini, R.; St Clair, E. W.; Breedveld, F.; Furst, D.; Kalden, J.; Weisman, M.; Smolen, J.; Emery, P.; Harriman, G.; Feldmann, M.; Lipsky, P. Infliximab (chimeric anti-tumour necrosis factor alpha monoclonal antibody) versus placebo in rheumatoid arthritis patients receiving concomitant methotrexate: a randomised phase III trial. ATTRACT Study Group. *Lancet* **1999**, *354*, 1932-1939.

(43) Mohan, N.; Edwards, E. T.; Cupps, T. R.; Oliverio, P. J.; Sandberg, G.; Crayton, H.; Richert, J. R.; Siegel, J. N. Demyelination occurring during anti-tumor necrosis factor alpha therapy for inflammatory arthritides. *Arthritis Rheum* **2001**, *44*, 2862-2869.

(44) Francis, G. S. TNF-alpha and heart failure. The difference between proof of principle and hypothesis testing. *Circulation* **1999**, *99*, 3213-3214.

(45) Knight, D. M.; Trinh, H.; Le, J.; Siegel, S.; Shealy, D.; McDonough, M.; Scallon, B.; Moore, M. A.; Vilcek, J.; Daddona, P.; et al. Construction and initial characterization of a mouse-human chimeric anti-TNF antibody. *Mol Immunol* **1993**, *30*, 1443-1453.

(46) CBIP Centre Belge d'Information Pharmacothérapeutique, 2010.

(47) INAMI Institut national d'assurance maladie-invalidité, 2009.

(48) Dejardin, E.; Droin, N. M.; Delhase, M.; Haas, E.; Cao, Y.; Makris, C.; Li, Z. W.; Karin, M.; Ware, C. F.; Green, D. R. The lymphotoxin-beta receptor induces different patterns of gene expression via two NF-kappaB pathways. *Immunity* **2002**, *17*, 525-535.

(49) Claudio, E.; Brown, K.; Park, S.; Wang, H.; Siebenlist, U. BAFF-induced NEMO-independent processing of NF-kappa B2 in maturing B cells. *Nat Immunol* **2002**, *3*, 958-965.

(50) Silverman, N.; Maniatis, T. NF-kappa B signaling pathways in mammalian and insect innate immunity. *Gene Dev* **2001**, *15*, 2321-2342.

(51) Barkett, M.; Gilmore, T. D. Control of apoptosis by Rel/NF-kappa B transcription factors. *Oncogene* **1999**, *18*, 6910-6924.

(52) Karin, M.; Lin, A. NF-kappa B at the crossroads of life and death. *Nat Immunol* **2002**, *3*, 221-227.

(53) Hayden, M. S.; Ghosh, S. Signaling to NF-kappaB. *Genes Dev* **2004**, *18*, 2195-2224.

(54) Han, Z.; Boyle, D. L.; Manning, A. M.; Firestein, G. S. AP-1 and NF-kappaB regulation in rheumatoid arthritis and murine collagen-induced arthritis. *Autoimmunity* **1998**, *28*, 197-208.

(55) Siebenlist, U.; Franzoso, G.; Brown, K. Structure, Regulation and Function of Nf-Kappa-B. *Annu Rev Cell Biol* **1994**, *10*, 405-455.

(56) Martinon, F.; Tschopp, J. NLRs join TLRs as innate sensors of pathogens. *Trends Immunol* **2005**, *26*, 447-454.

(57) Yamaguchi, K.; Shirakabe, T.; Shibuya, H.; Irie, K.; Oishi, I.; Ueno, N.; Taniguchi, T.; Nishida, E.; Matsumoto, K. Identification of a Member of the Mapkkk Family as a Potential Mediator of Tgf-Beta Signal-Transduction. *Science* **1995**, *270*, 2008-2011.

(58) Sato, S.; Sanjo, H.; Takeda, K.; Ninomiya-Tsuji, J.; Yamamoto, M.; Kawai, T.; Matsumoto, K.; Takeuchi, O.; Akira, S. Essential function for the kinase TAK1 in innate and adaptive immune responses. *Nat Immunol* **2005**, *6*, 1087-1095.

(59) Shim, J. H.; Xiao, C.; Paschal, A. E.; Bailey, S. T.; Rao, P.; Hayden, M. S.; Lee, K. Y.; Bussey, C.; Steckel, M.; Tanaka, N.; Yamada, G.; Akira, S.; Matsumoto, K.; Ghosh, S. TAK1, but not TAB1 or TAB2, plays an essential role in multiple signaling pathways in vivo. *Genes Dev* **2005**, *19*, 2668-2681.

(60) Vallabhapurapu, S.; Karin, M. Regulation and function of NF-kappaB transcription factors in the immune system. *Annu Rev Immunol* **2009**, *27*, 693-733.

(61) Dejardin, E. The alternative NF-kappaB pathway from biochemistry to biology: Pitfalls and promises for future drug development. *Biochem Pharmacol* **2006**, *72*, 1161-1179.

(62) Vallabhapurapu, S.; Matsuzawa, A.; Zhang, W.; Tseng, P. H.; Keats, J. J.; Wang, H.; Vignali, D. A.; Bergsagel, P. L.; Karin, M. Nonredundant and complementary functions of TRAF2 and TRAF3 in a ubiquitination cascade that activates NIK-dependent alternative NF-kappaB signaling. *Nat Immunol* **2008**, *9*, 1364-1370.

(63) Liao, G. X.; Zhang, M. Y.; Harhaj, E. W.; Sun, S. C. Regulation of the NF-kappa B-inducing kinase by tumor necrosis factor receptor-associated factor 3-induced degradation. *J Biol Chem* **2004**, *279*, 26243-26250.

(64) Coope, H. J.; Atkinson, P. G.; Huhse, B.; Belich, M.; Janzen, J.; Holman, M. J.; Klaus, G. G.; Johnston, L. H.; Ley, S. C. CD40 regulates the processing of NF-kappaB2 p100 to p52. *Embo J* **2002**, *21*, 5375-5385.

(65) Aloisi, F.; Pujol-Borrell, R. Lymphoid neogenesis in chronic inflammatory diseases. *Nat Rev Immunol* **2006**, *6*, 205-217.

(66) Drayton, D. L.; Liao, S.; Mounzer, R. H.; Ruddle, N. H. Lymphoid organ development: from ontogeny to neogenesis. *Nat Immunol* **2006**, *7*, 344-353.

(67) Gommerman, J. L.; Browning, J. L. Lymphotoxin/light, lymphoid microenvironments and autoimmune disease. *Nat Rev Immunol* **2003**, *3*, 642-655.

(68) Ng, L. G.; Mackay, C. R.; Mackay, F. The BAFF/APRIL system: life beyond B lymphocytes. *Mol Immunol* **2005**, *42*, 763-772.

(69) Edwards, J. C.; Cambridge, G. B-cell targeting in rheumatoid arthritis and other autoimmune diseases. *Nat Rev Immunol* **2006**, *6*, 394-403.

(70) Aya, K.; Alhawagri, M.; Hagen-Stapleton, A.; Kitaura, H.; Kanagawa, O.; Novack, D. V. NF-(kappa)B-inducing kinase controls lymphocyte and osteoclast activities in inflammatory arthritis. *J Clin Invest* **2005**, *115*, 1848-1854.

(71) Baud, V.; Karin, M. OPINION Is NF-kappa B a good target for cancer therapy? Hopes and pitfalls. *Nat Rev Drug Discov* **2009**, *8*, 33-40.

(72) Karin, M. Nuclear factor-kappa B in cancer development and progression. *Nature* **2006**, *441*, 431-436.

(73) Lawrence, T.; Bebien, M.; Liu, G. Y.; Nizet, V.; Karin, M. IKK alpha limits macrophage NF-kappa B activation and contributes to the resolution of inflammation. *Nature* **2005**, *434*, 1138-1143.

(74) Greten, F. R.; Eckmann, L.; Greten, T. F.; Park, J. M.; Li, Z. W.; Egan, L. J.; Kagnoff, M. F.; Karin, M. IKK beta links inflammation and tumorigenesis in a mouse model of colitis-associated cancer. *Cell* **2004**, *118*, 285-296.

(75) Dutta, J.; Fan, Y.; Gupta, N.; Fan, G.; Gelinas, C. Current insights into the regulation of programmed cell death by NF-kappa B. *Oncogene* **2006**, *25*, 6800-6816.

(76) Luo, J. L.; Kamata, H.; Karin, M. IKK/NF-kappa B signaling: balancing life and death - a new approach to cancer therapy. *J Clin Invest* **2005**, *115*, 2625-2632.

(77) Malinin, N. L.; Boldin, M. P.; Kovalenko, A. V.; Wallach, D. MAP3K-related kinase involved in NF-kappaB induction by TNF, CD95 and IL-1. *Nature* **1997**, *385*, 540-544.

(78) Lavorgna, A.; De Filippi, R.; Formisano, S.; Leonardi, A. TNF receptor-associated factor 1 is a positive regulator of the NF-kappaB alternative pathway. *Mol Immunol* **2009**, *46*, 3278-3282.

(79) Ling, L.; Cao, Z. D.; Goeddel, D. V. NF-kappa B-inducing kinase activates IKK-alpha by phosphorylation of Ser-176. *P Natl Acad Sci USA* **1998**, *95*, 3792-3797.

(80) Lin, X.; Mu, Y.; Cunningham, E. T., Jr.; Marcu, K. B.; Geleziunas, R.; Greene, W. C. Molecular determinants of NF-kappaB-inducing kinase action. *Mol Cell Biol* **1998**, *18*, 5899-5907.

(81) Cherry, M.; Williams, D. H. Recent kinase and kinase inhibitor X-ray structures: mechanisms of inhibition and selectivity insights. *Curr Med Chem* **2004**, *11*, 663-673.

(82) Hubbard, S. R.; Till, J. H. Protein tyrosine kinase structure and function. *Annu Rev Biochem* **2000**, *69*, 373-398.

(83) Scapin, G. Protein kinase inhibition: different approaches to selective inhibitor design. *Curr Drug Targets* **2006**, *7*, 1443-1454.

(84) Smyth, L. A.; Collins, I. Measuring and interpreting the selectivity of protein kinase inhibitors. *J Chem Biol* **2009**, *2*, 131-151.

(85) Squire, C. J.; Dickson, J. M.; Ivanovic, I.; Baker, E. N. Structure and inhibition of the human cell cycle checkpoint kinase, Wee1A kinase: an atypical tyrosine kinase with a key role in CDK1 regulation. *Structure* **2005**, *13*, 541-550.

(86) Zhang, J.; Yang, P. L.; Gray, N. S. Targeting cancer with small molecule kinase inhibitors. *Nat Rev Cancer* **2009**, *9*, 28-39.

(87) Hantschel, O.; Superti-Furga, G. Regulation of the c-Abl and Bcr-Abl tyrosine kinases. *Nat Rev Mol Cell Biol* **2004**, *5*, 33-44.

(88) Buchdunger, E.; Zimmermann, J.; Mett, H.; Meyer, T.; Muller, M.; Druker, B. J.; Lydon, N. B. Inhibition of the Abl protein-tyrosine kinase in vitro and in vivo by a 2-phenylaminopyrimidine derivative. *Cancer Res* **1996**, *56*, 100-104.

(89) Seeliger, M. A.; Nagar, B.; Frank, F.; Cao, X.; Henderson, M. N.; Kuriyan, J. c-Src binds to the cancer drug imatinib with an inactive Abl/c-Kit conformation and a distributed thermodynamic penalty. *Structure* **2007**, *15*, 299-311.

(90) Ghose, A. K.; Herbertz, T.; Pippin, D. A.; Salvino, J. M.; Mallamo, J. P. Knowledge based prediction of ligand binding modes and rational inhibitor design for kinase drug discovery. *J Med Chem* **2008**, *51*, 5149-5171.

(91) Gribble, F. M.; Loussouarn, G.; Tucker, S. J.; Zhao, C.; Nichols, C. G.; Ashcroft, F. M. A novel method for measurement of submembrane ATP concentration. *J Biol Chem* **2000**, *275*, 30046-30049.

(92) Traut, T. W. Physiological concentrations of purines and pyrimidines. *Mol Cell Biochem* **1994**, *140*, 1-22.

(93) Janne, P. A.; Gray, N.; Settleman, J. Factors underlying sensitivity of cancers to small-molecule kinase inhibitors. *Nat Rev Drug Discov* **2009**, *8*, 709-723.

(94) Tsang, C. K.; Qi, H.; Liu, L. F.; Zheng, X. F. Targeting mammalian target of rapamycin (mTOR) for health and diseases. *Drug Discov Today* **2007**, *12*, 112-124.

(95) Petrelli, A.; Giordano, S. From single- to multi-target drugs in cancer therapy: when aspecificity becomes an advantage. *Curr Med Chem* **2008**, *15*, 422-432.

(96) Krug, M.; Hilgeroth, A. Recent advances in the development of multi-kinase inhibitors. *Mini Rev Med Chem* **2008**, *8*, 1312-1327.

(97) Klebl, B. M.; Muller, G. Second-generation kinase inhibitors. *Expert Opin Ther Targets* **2005**, *9*, 975-993.

(98) Castrillo, A.; de Las Heras, B.; Hortelano, S.; Rodriguez, B.; Villar, A.; Bosca, L. Inhibition of the nuclear factor kappa B (NF-kappa B) pathway by tetracyclic kaurene diterpenes in macrophages. Specific effects on NF-kappa B-inducing kinase activity and on the coordinate activation of ERK and p38 MAPK. *J Biol Chem* **2001**, *276*, 15854-15860.

(99) Nemoto, S.; Xiang, J. L.; Huang, S.; Lin, A. N. Induction of apoptosis by SB202190 through inhibition of p38 beta mitogen-activated protein kinase. *J Biol Chem* **1998**, *273*, 16415-16420.

(100) Kim, H. B.; Evans, I.; Smallwood, R.; Holcombe, M.; Qwarnstrom, E. E. NIK and IKKbeta interdependence in NF-kappaB signalling-Flux analysis of regulation through metabolites. *Biosystems* **2009**.

(101) Chen, G.; Cushing, T., D.;; Fisher, B.; HE, X.; Li, K.; Li, Z.; McGee, L., R.;; Pattaropong, V.; Faulder, P. Alkynyl Alcohols As Kinase Inhibitors. In *WO 2009/158011 A1*, 2009.

(102) Majid, T., N.; Hopkins, C.; Pedgrift, L., B.; Collar, N.;Friederike, W-B.; Merrill, J. Pyrazoloisoquinoline derivatives as kinase inhibitors for the treatment of various disorders. In *US 2005/0009859 A1*, 2005.

(103) Flohr, S. N., T. Pyrazoloisoquinoline derivatives for inhibiting NF-kB inducing kinase. In *PCT Int. Appl. US 6,841,556 B2*, 2005.

(104) Altschul, S. F.; Madden, T. L.; Schaffer, A. A.; Zhang, J. H.; Zhang, Z.; Miller, W.; Lipman, D. J. Gapped BLAST and PSI-BLAST: a new generation of protein database search programs. *Nucleic Acids Res* **1997**, *25*, 3389-3402.

(105) Berman, H. M.; Westbrook, J.; Feng, Z.; Gilliland, G.; Bhat, T. N.; Weissig, H.; Shindyalov, I. N.; Bourne, P. E. The Protein Data Bank. *Nucleic Acids Res* **2000**, *28*, 235-242.

(106) Lambert, C.; Leonard, N.; De Bolle, X.; Depiereux, E. ESyPred3D: Prediction of proteins 3D structures. *Bioinformatics* **2002**, *18*, 1250-1256.

(107) Sali, A.; Blundell, T. L. Comparative protein modelling by satisfaction of spatial restraints. *J Mol Biol* **1993**, *234*, 779-815.

(108) Tripos, I. *SYBYL*; 8.0 ed.: 1699 South Hanley Rd., St. Louis, Missouri, 63144, USA.

(109) Ramachandran, G. N.; Ramakrishnan, C.; Sasisekharan, V. Stereochemistry of polypeptide chain configurations. *J Mol Biol* **1963**, *7*, 95-99.

(110) Mortier, J.; Frederick, R.; Ganeff, C.; Remouchamps, C.; Talaga, P.; Pochet, L.; Wouters, J.; Piette, J.; Dejardin, E.; Masereel, B. Pyrazolo[4,3-*c*]isoquinolines as potential inhibitors of NF-kappaB activation. *Biochem Pharmacol* **2010**, *79*, 1462-1472.

(111) Xiao, G. T.; Harhaj, E. W.; Sun, S. C. NF-kappa B-inducing kinase regulates the processing of NF-kappa B2 p100. *Mol Cell* **2001**, *7*, 401-409.

(112) Dejardin, E. **To be published**.

(113) Ruegg, U. T.; Burgess, G. M. Staurosporine, K-252 and UCN-01: potent but nonspecific inhibitors of protein kinases. *Trends Pharmacol Sci* **1989**, *10*, 218-220.

(114) Jones, G.; Willett, P.; Glen, R. C.; Leach, A. R.; Taylor, R. Development and validation of a genetic algorithm for flexible docking. *J Mol Biol* **1997**, *267*, 727-748.

(115) Saloutin, V. I.; Burgart, Y. V.; Skryabina, Z. E.; Kuzueva, O. G. Synthesis of fluoroalkyl-containing 2-oxyimino-1,3-dicarbonyl compounds and their reaction with hydrazine hydrate. *J Fluorine Chem* **1997**, *84*, 107-111.

(116) Majid, T.; Hopkins, C. R.; Pedgrift, B.; Collar, N. Convenient synthesis of 4-amino-3,5-disubstituted pyrazoles in one-step from the corresponding diketo oximes. *Tet Lett* **2004**, *45*, 2137-2139.

(117) Pictet, A.; Gams, A. New Method for the Synthetic Preparation of Isoquinoline Bases. *Ber Dtsch Chem Ges* **1910**, *43*, 2384-2391.

(118) Anand, N. K.; Blazey, C. M.; Bowles, O. J.; Bussenius, J.; Costanzo, S.; Curtis, J. K.; Dubenko, L.; Kennedy, A. R.; Khoury, R. G.; Kim, A. I.; Manalo, J.-C. L.; Peto, C. J.; Rice, K. D.; Tsang, T. H. Preparation of pyrazolo[3,4-c]isoquinoline derivatives as anaplastic lymphoma kinase modulators. In *PCT Int. Appl. US 2007/0032515*, 2005.

(119) Irwin, J. J.; Shoichet, B. K. ZINC - A free database of commercially available compounds for virtual screening. *J. Chem. Inf. Comput. Sci.* **2005**, *45*, 177-182.

(120) Manthey, C. L.; Wang, S. W.; Kinney, S. D.; Yao, Z. B. SB202190, a selective inhibitor of p38 mitogen-activated protein kinase, is a powerful regulator of LPS-induced mRNAs in monocytes. *J Leukocyte Biol* **1998**, *64*, 409-417.

(121) Atkins, C. M.; Selcher, J. C.; Petraitis, J. J.; Trzaskos, J. M.; Sweatt, J. D. The MAPK cascade is required for mammalian associative learning. *Nature Neurosci* **1998**, *1*, 602-609.

(122) Duncia, J. V.; Santella, J. B.; Higley, C. A.; Pitts, W. J.; Wityak, J.; Frietze, W. E.; Rankin, F. W.; Sun, J. H.; Earl, R. A.; Tabaka, A. C.; Teleha, C. A.; Blom, K. F.; Favata, M. F.; Manos, E. J.; Daulerio, A. J.; Stradley, D. A.; Horiuchi, K.; Copeland, R. A.; Scherle, P. A.; Trzaskos, J. M.; Magolda, R. L.; Trainor, G. L.; Wexler, R. R.; Hobbs, F. W.; Olson, R. E. MEK inhibitors: The chemistry and biological activity of U0126, its analogs, and cyclization products. *Bioorg Med Chem Lett* **1998**, *8*, 2839-2844.

(123) Wang, X. K.; Wang, H.; Xu, L.; Rozanski, D. J.; Sugawara, T.; Chan, P. H.; Trzaskos, J. M.; Feuerstein, G. Z. Significant neuroprotection against ischemic brain injury by inhibition of the MEK1 protein kinase in mice: Exploration of potential mechanism associated with apoptosis. *J Pharmacol Exp Ther* **2003**, *304*, 172-178.

(124) Dudley, D. T.; Pang, L.; Decker, S. J.; Bridges, A. J.; Saltiel, A. R. A Synthetic Inhibitor of the Mitogen-Activated Protein-Kinase Cascade. *P Natl Acad Sci USA* **1995**, *92*, 7686-7689.

(125) Dumont, F. J.; Staruch, M. J.; Fischer, P.; DaSilva, C.; Camacho, R. Inhibition of T cell activation by pharmacologic disruption of the MEK1/ERK MAP kinase or calcineurin signaling pathways results in differential modulation of cytokine production. *Journal of Immunology* **1998**, *160*, 2579-2589.

(126) Alessi, D. R.; Cuenda, A.; Cohen, P.; Dudley, D. T.; Saltiel, A. R. Pd-098059 Is a Specific Inhibitor of the Activation of Mitogen-Activated Protein-Kinase Kinase in-Vitro and in-Vivo. *J Biol Chem* **1995**, *270*, 27489-27494.

(127) Tamaoki, T.; Nomoto, H.; Takahashi, I.; Kato, Y.; Morimoto, M.; Tomita, F. Staurosporine, a potent inhibitor of phospholipid/Ca++dependent protein kinase. *Biochem Biophys Res Commun* **1986**, *135*, 397-402.

(128) Brown, K.; Vial, S. C.; Dedi, N.; Long, J. M.; Dunster, N. J.; Cheetham, G. M. Structural basis for the interaction of TAK1 kinase with its activating protein TAB1. *J Mol Biol* **2005**, *354*, 1013-1020.

(129) LCC, D. S. *Pymol*.

(130) Gaestel, M.; Kotlyarov, A.; Kracht, M. Targeting innate immunity protein kinase signalling in inflammation. *Nat Rev Drug Discov* **2009**, *8*, 480-499.

(131) Tang, M.; Wei, X.; Guo, Y.; Breslin, P.; Zhang, S.; Wei, W.; Xia, Z.; Diaz, M.; Akira, S.; Zhang, J. TAK1 is required for the survival of hematopoietic cells and hepatocytes in mice. *J Exp Med* **2008**, *205*, 1611-1619.

(132) Byth, K.; Palakurthi, S.; Yu, L.; Zang, Q. Methods for cancer treatment using TAK1 inhibitors; AstraZeneca AB (85 Sodertalje, SE), 2009.

(133) Nagar, B.; Bornmann, W. G.; Pellicena, P.; Schindler, T.; Veach, D. R.; Miller, W. T.; Clarkson, B.; Kuriyan, J. Crystal structures of the kinase domain of c-Abl in complex with the small molecule inhibitors PD173955 and imatinib (STI-571). *Cancer Res* **2002**, *62*, 4236-4243.

(134) Lengauer, T.; Lemmen, C.; Rarey, M.; Zimmermann, M. Novel technologies for virtual screening. *Drug Discov Today* **2004**, *9*, 27-34.

(135) Rees, D. C.; Congreve, M.; Murray, C. W.; Carr, R. Fragment-based lead discovery. *Nat Rev Drug Discov* **2004**, *3*, 660-672.

(136) Abad-Zapatero, C.; Metz, J. T. Ligand efficiency indices as guideposts for drug discovery. *Drug Discov Today* **2005**, *10*, 464-469.

(137) Reynolds, C. H.; Tounge, B. A.; Bembenek, S. D. Ligand binding efficiency: Trends, physical basis, and implications. *J Med Chem* **2008**, *51*, 2432-2438.

(138) Congreve, M.; Chessari, G.; Tisi, D.; Woodhead, A. J. Recent developments in fragment-based drug discovery. *J Med Chem* **2008**, *51*, 3661-3680.

(139) Zartler, E. R.; Shapiro, M. J. *Fragment-based drug discovery*; John Wiley & Sons, 2008.

(140) Frederick, R. **To be published**.

(141) Bemis, G. W.; Murcko, M. A. The properties of known drugs .1. Molecular frameworks. *J Med Chem* **1996**, *39*, 2887-2893.

(142) Bemis, G. W.; Murcko, M. A. Properties of known drugs. 2. Side chains. *J Med Chem* **1999**, *42*, 5095-5099.

(143) Baxter, C. A.; Murray, C. W.; Clark, D. E.; Westhead, D. R.; Eldridge, M. D. A new approach to molecular docking. *Abstr Pap Am Chem S* **1998**, *216*, U693-U693.

(144) Eldridge, M. D.; Murray, C. W.; Auton, T. R.; Paolini, G. V.; Mee, R. P. Empirical scoring functions .1. The development of a fast empirical scoring function to estimate the binding affinity of ligands in receptor complexes. *J Comput Aid Mol Des* **1997**, *11*, 425-445.

(145) Mooij, W. T. M.; Verdonk, M. L. General and targeted statistical potentials for protein-ligand interactions. *Proteins* **2005**, *61*, 272-287.

(146) Hopkins, A. L.; Groom, C. R.; Alex, A. Ligand efficiency: a useful metric for lead selection. *Drug Discov Today* **2004**, *9*, 430-431.

(147) Schulz, M. N.; Hubbard, R. E. Recent progress in fragment-based lead discovery. *Curr Opin Pharmacol* **2009**, *9*, 615-621.

(148) Mosyak, L.; Zhang, Y.; Glasfeld, E.; Haney, S.; Stahl, M.; Seehra, J.; Somers, W. S. The bacterial cell-division protein ZipA and its interaction with an FtsZ fragment revealed by X-ray crystallography. *Embo J* **2000**, *19*, 3179-3191.

(149) Hajduk, P. J.; Gerfin, T.; Boehlen, J. M.; Haberli, M.; Marek, D.; Fesik, S. W. High-throughput nuclear magnetic resonance-based screening. *J Med Chem* **1999**, *42*, 2315-2317.

(150) Lipinski, C. A.; Lombardo, F.; Dominy, B. W.; Feeney, P. J. Experimental and computational approaches to estimate solubility and permeability in drug discovery and development settings. *Adv Drug Deliver Rev* **1997**, *23*, 3-25.

(151) Teague, S. J.; Davis, A. M.; Leeson, P. D.; Oprea, T. The Design of Leadlike Combinatorial Libraries. *Angew Chem Int Ed Engl* **1999**, *38*, 3743-3748.

(152) Bolton, J. L.; Trush, M. A.; Penning, T. M.; Dryhurst, G.; Monks, T. J. Role of quinones in toxicology. *Chem Res Toxicol* **2000**, *13*, 135-160.

(153) Cooke, H.; Ridley, D. D. The challenges with substance databases and structure search engines. *Aust J Chem* **2004**, *57*, 387-392.

(154) Zhang, J. H.; Chung, T. D.; Oldenburg, K. R. A Simple Statistical Parameter for Use in Evaluation and Validation of High Throughput Screening Assays. *J Biomol Screen* **1999**, *4*, 67-73.

(155) Iversen, P. W.; Eastwood, B. J.; Sittampalam, G. S.; Cox, K. L. A comparison of assay performance measures in screening assays: Signal window, Z ' factor, and assay variability ratio. *J Biomol Screen* **2006**, *11*, 247-252.

(156) Lemke, T., L.; ; Williams, D., A.;; Roche, V., F.;; Zito, S., W. *Foye's principles of medicinal chemistry (6th edition)*; Lippincott Williams & Wilkins: Baltimore, 2008.

(157) Ludeman, S. M. The chemistry of the metabolites of cyclophosphamide. *Curr Pharm Des* **1999**, *5*, 627-643.

(158) Shoichet, B. K. Virtual screening of chemical libraries. *Nature* **2004**, *432*, 862-865.

(159) Mortier, J.; Masereel, B.; Remouchamps, C.; Ganeff, C.; Piette, J.; Frederick, R. Discovery of novel potent NF-kappaB inducing kinase (NIK) inhibitors through virtual screening. *Bioorg Med Chem Lett* **submitted for publication**.

(160) Tsou, H. R.; Liu, X.; Birnberg, G.; Kaplan, J.; Otteng, M.; Tran, T.; Kutterer, K.; Tang, Z. L.; Suayan, R.; Zask, A.; Ravi, M.; Bretz, A.; Grillo, M.; McGinnis, J. P.; Rabindran, S. K.; Ayral-Kaloustian, S.; Mansour, T. S. Discovery of 4-(Benzylaminomethylene)isoquinoline-1,3-(2H,4H)-diones and 4-[(Pyridylmethyl)aminomethylene]isoquinoline-1,3-(2H,4H)-diones as Potent and Selective Inhibitors of the Cyclin-Dependent Kinase 4. *J Med Chem* **2009**, *52*, 2289-2310.

(161) Tsou, H. R.; Otteng, M.; Tran, T.; Floyd, M. B.; Reich, M.; Birnberg, G.; Kutterer, K.; Ayral-Kaloustian, S.; Ravi, M.; Nilakantan, R.; Grillo, M.; McGinnis, J. P.; Rabindran, S. K. 4-(phenylaminomethylene)isoquinoline-1,3(2H,4H)-diones as potent and selective inhibitors of the cyclin-dependent kinase 4 (CDK4). *J Med Chem* **2008**, *51*, 3507-3525.

(162) Laskowski, R. A. PDBsum: summaries and analyses of PDB structures. *Nucleic Acids Res* **2001**, *29*, 221-222.

(163) Millipore KinaseProfiler™ Service Assay Protocols; Millipore, 2010.

Appendix

Appendix 1: Multikinase screening residual activities (%) for compounds **5d** and **11f** with the 263 reported kinases

Kinase	**5d**	**11f**
Abl(h)	94	**1**
Abl(m)	66	**2**
Abl (H396P) (h)	62	**2**
Abl (M351T)(h)	54	**8**
Abl (Q252H) (h)	59	**1**
Abl(T315I)(h)	**50**	53
Abl(Y253F)(h)	67	**3**
ACK1(h)	**18**	**9**
ALK(h)	51	**32**
ALK4(h)	105	69
Arg(h)	89	**1**
AMPK(r)	**39**	78
Arg(m)	80	**3**
ARK5(h)	**3**	72
ASK1(h)	**0**	68
Aurora-A(h)	**8**	52
Axl(h)	51	94
Blk(m)	67	**21**
Bmx(h)	**22**	**19**
BRK(h)	89	**-2**
BrSK1(h)	**31**	**16**
BrSK2(h)	**26**	**39**
BTK(h)	**40**	**30**
BTK(R28H)(h)	95	108
CaMKI(h)	66	104
CaMKIIβ(h)	52	56
CaMKIIγ(h)	**25**	62
CaMKIδ(h)	100	92
CaMKIIδ(h)	**11**	**42**
CaMKIV(h)	88	114
CDK1/cyclinB(h)	**44**	109
CDK2/cyclinA(h)	**40**	93
CDK2/cyclinE(h)	**29**	90
CDK3/cyclinE(h)	**19**	85
CDK5/p25(h)	**17**	**49**
CDK5/p35(h)	**19**	57
CDK7/cyclinH/MAT1(h)	72	96

CDK9/cyclin T1(h)	54	**47**
CHK1(h)	**6**	88
CHK2(h)	**18**	92
CHK2(I157T)(h)	**23**	87
CHK2(R145W)(h)	**22**	95
CK1γ1(h)	80	86
CK1γ2(h)	57	74
CK1γ3(h)	78	63
CK1δ(h)	81	**49**
CK1(y)	57	**31**
CK2(h)	96	94
CK2α2(h)	90	104
CLK2(h)	**18**	**20**
CLK3(h)	67	86
cKit(h)	71	**15**
cKit(D816V)(h)	100	56
cKit(D816H)(h)	**12**	**5**
cKit(V560G)(h)	**9**	**4**
cKit(V654A)(h)	**9**	**15**
CSK(h)	112	69
c-RAF(h)	84	**1**
cSRC(h)	78	**17**
DAPK1(h)	82	81
DAPK2(h)	76	57
DCAMKL2(h)	105	84
DDR2(h)	91	**40**
DMPK(h)	96	105
DRAK1(h)	**32**	70
DYRK2(h)	53	52
eEF-2K(h)	122	113
EGFR(h)	110	**22**
EGFR(L858R)(h)	**50**	**8**
EGFR(L861Q)(h)	66	**6**
EGFR(T790M)(h)	**30**	78
EGFR(T790M,L858R)(h)	**17**	53
EphA1(h)	**23**	**-1**
EphA2(h)	79	**0**
EphA3(h)	86	**5**
EphA4(h)	89	**2**
EphA5(h)	83	**-1**
EphA7(h)	60	89
EphA8(h)	82	**1**

EphB2(h)	86	**1**
EphB1(h)	77	**1**
EphB3(h)	80	**2**
EphB4(h)	86	**0**
ErbB4(h)	91	66
FAK(h)	**8**	91
Fer(h)	**5**	91
Fes(h)	**11**	59
FGFR1(h)	**12**	**9**
FGFR1(V561M)(h)	**10**	66
FGFR2(h)	**40**	**43**
FGFR2(N549H)(h)	**16**	**14**
FGFR3(h)	**27**	**44**
FGFR4(h)	99	90
Fgr(h)	58	**2**
Flt1(h)	**18**	**12**
Flt3(D835Y)(h)	**0**	**30**
Flt3(h)	**6**	76
Flt4(h)	**-2**	**7**
Fms(h)	**5**	**11**
Fyn(h)	61	**4**
GCK(h)	**7**	**25**
GRK5(h)	66	100
GRK6(h)	68	83
GRK7(h)	**43**	102
GSK3α(h)	**47**	**14**
GSK3β(h)	70	**19**
Haspin(h)	83	**37**
Hck(h)	71	**6**
HIPK1(h)	105	95
HIPK2(h)	67	80
HIPK3(h)	80	99
IGF-1R(h)	62	132
IGF-1R(h), activated	71	91
IKKα(h)	86	84
IKKβ(h)	55	**21**
IR(h)	55	97
IR(h), activated	62	93
IRR(h)	83	97
IRAK1(h)	**50**	94
IRAK4(h)	51	90
Itk(h)	53	124

JAK2(h)	**24**	79
JAK3(h)	**39**	110
JNK1α1(h)	61	90
JNK2α2(h)	65	99
JNK3(h)	**15**	61
KDR(h)	**8**	**21**
Lck(h)	**31**	**4**
LIMK1(h)	**26**	**17**
LKB1(h)	85	**5**
LOK(h)	**15**	**18**
Lyn(h)	96	**3**
Lyn(m)	85	**1**
MAPK1(h)	56	67
MAPK2(h)	63	106
MAPK2(m)	**34**	72
MAPKAP-K2(h)	114	115
MAPKAP-K3(h)	105	98
MEK1(h)	68	99
MARK1(h)	54	76
MELK(h)	**12**	**49**
Mer(h)	**5**	75
Met(h)	79	77
MINK(h)	74	66
MKK4(m)	**46**	58
MKK6(h)	106	**-6**
MKK7β(h)	52	80
MLCK(h)	64	**11**
MLK1(h)	**2**	**28**
Mnk2(h)	**14**	68
MRCKα(h)	102	104
MRCKβ(h)	109	110
MSK1(h)	76	81
MSK2(h)	**29**	61
MSSK1(h)	78	83
MST1(h)	**13**	93
MST2(h)	**23**	89
MST3(h)	95	**36**
mTOR(h)	103	106
mTOR/FKBP12(h)	95	103
MuSK(h)	76	105
NEK2(h)	104	120
NEK3(h)	97	83

NEK6(h)	99	108
NEK7(h)	96	106
NEK11(h)	111	**17**
NLK(h)	83	**27**
p70S6K(h)	68	76
PAK2(h)	92	98
PAK3(h)	81	91
PAK4(h)	60	103
PAK5(h)	59	99
PAK6(h)	**48**	89
PAR-1Bα(h)	59	73
PASK(h)	96	80
PDGFRα(h)	93	61
PDGFRα(D842V)(h)	**24**	**7**
PDGFRα(V561D)(h)	**11**	**0**
PDGFRβ(h)	119	113
PDK1(h)	**11**	95
PhKγ2(h)	72	115
Pim-1(h)	62	**37**
Pim-2(h)	73	**35**
Pim-3(h)	89	90
PKA(h)	109	61
PKBα(h)	106	90
PKBβ(h)	110	107
PKBγ(h)	90	**41**
PKCα(h)	99	99
PKCβI(h)	85	75
PKCβII(h)	98	109
PKCγ(h)	68	90
PKCδ(h)	66	**14**
PKCε(h)	91	86
PKCη(h)	95	**16**
PKCι(h)	103	86
PKCμ(h)	**43**	66
PKCθ(h)	91	**26**
PKCζ(h)	98	**21**
PKD2(h)	82	85
PKG1α(h)	99	96
PKG1β(h)	89	80
Plk1(h)	88	93
Plk3(h)	120	123
PRAK(h)	96	103
PRK2(h)	65	**31**

PrKX(h)	87	73
PTK5(h)	82	**6**
Pyk2(h)	**46**	59
Ret(h)	**-1**	**7**
Ret (V804L)(h)	**1**	75
Ret(V804M)(h)	**2**	65
RIPK2(h)	80	**0**
ROCK-I(h)	79	97
ROCK-II(h)	70	88
ROCK-II(r)	68	84
Ron(h)	99	68
Ros(h)	96	96
Rse(h)	116	86
Rsk1(h)	**13**	76
Rsk1(r)	**16**	90
Rsk2(h)	**5**	67
Rsk3(h)	**3**	**47**
Rsk4(h)	**9**	69
SAPK2a(h)	103	58
SAPK2a(T106M)(h)	94	112
SAPK2b(h)	104	**28**
SAPK3(h)	102	94
SAPK4(h)	96	93
SGK(h)	76	88
SGK2(h)	83	**10**
SGK3(h)	107	108
SIK(h)	**41**	**17**
Snk(h)	69	60
Src(1-530)(h)	**46**	**4**
Src(T341M)(h)	**27**	82
SRPK1(h)	90	94
SRPK2(h)	98	95
STK33(h)	59	65
Syk(h)	69	99
TAK1(h)	**30**	80
TAO1(h)	**36**	**45**
TAO2(h)	66	**50**
TAO3(h)	**49**	69
TBK1(h)	**28**	86
Tec(h) activated	**41**	**29**
Tie2(h)	98	69
Tie2(R849W)(h)	71	76
Tie2(Y897S)(h)	79	61

TLK2(h)	54	107
TrkA(h)	**5**	71
TrkB(h)	**6**	96
TSSK1(h)	**38**	106
TSSK2(h)	73	103
Txk(h)	**45**	**6**
ULK2(h)	**45**	86
ULK3(h)	**40**	55
WNK2(h)	84	**50**
WNK3(h)	67	**45**
VRK2(h)	64	54
Yes(h)	69	**0**
ZAP-70(h)	101	102
ZIPK(h)	81	97

Appendix 2: ZINC database screening (part 1)

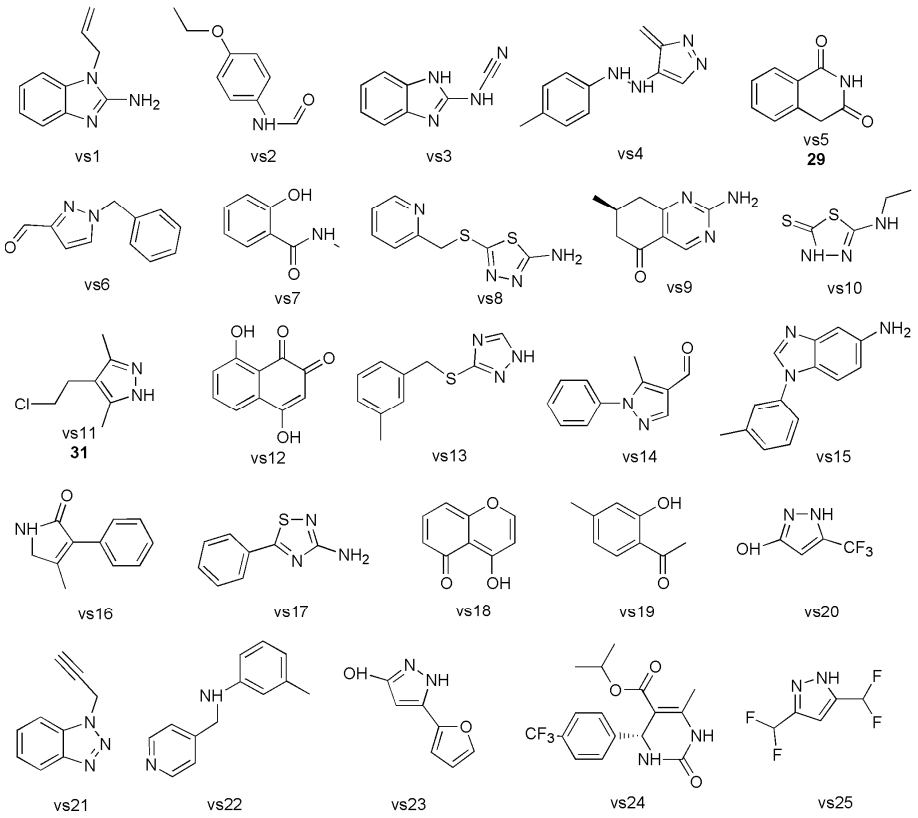

Appendix 3: ZINC database screening (part 2)

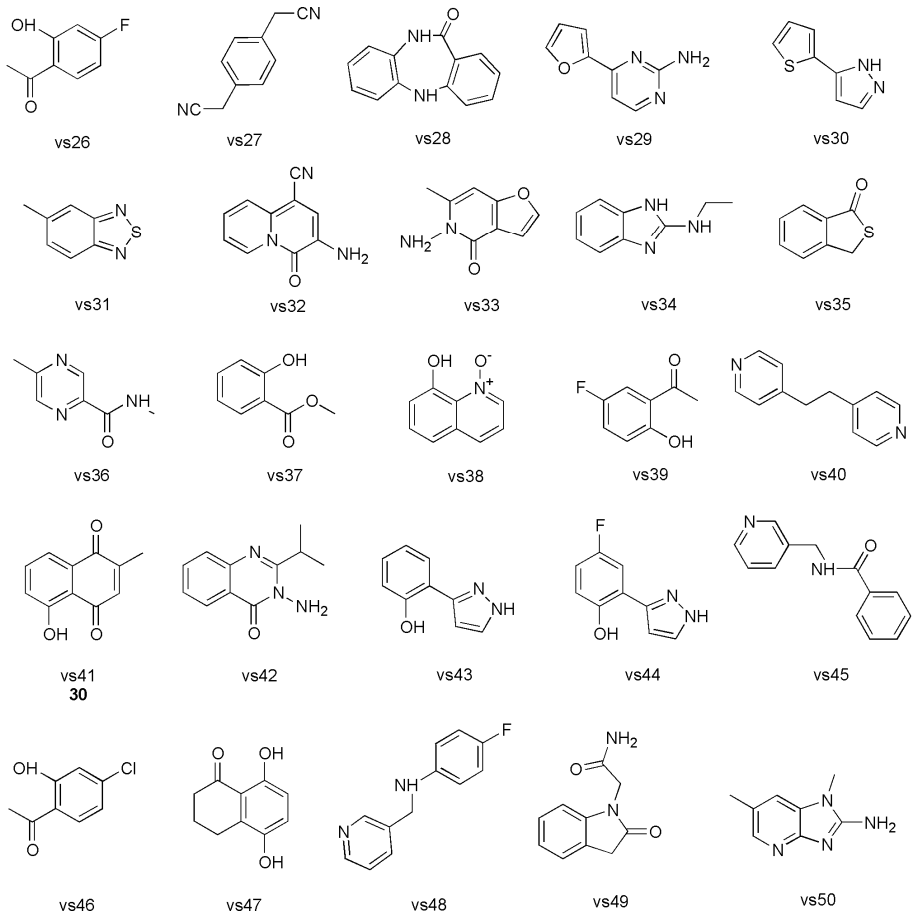

30

Appendix 4 : Published article

G Model
BCP-10430; No of Pages 11
ARTICLE IN PRESS

Biochemical Pharmacology xxx (2010) xxx–xxx

Contents lists available at ScienceDirect

Biochemical Pharmacology

journal homepage: www.elsevier.com/locate/biochempharm

Pyrazolo[4,3-c]isoquinolines as potential inhibitors of NF-κB activation

Jérémie Mortier [a,1], Raphaël Frederick [a,1], Corinne Ganeff [b], Caroline Remouchamps [b], Patrice Talaga [c], Lionel Pochet [a], Johan Wouters [a], Jacques Piette [b], Emmanuel Dejardin [b], Bernard Masereel [a,*]

[a] Drug Design & Discovery Center, University of Namur, FUNDP, 61 Rue de Bruxelles, 5000 Namur Belgium
[b] Laboratory of Virology and Immunology, GIGA Research, University of Liège, Belgium
[c] UCB SA Belgium

ARTICLE INFO

Article history:
Received 4 November 2009
Accepted 12 January 2010
Available online xxx

Keywords:
NF-κB inducing kinase
TGF-β activated kinase 1
Pyrazoloisoquinolines
Alternative pathway
Rheumatoid arthritis
Molecular modeling

ABSTRACT

In this work, we aimed to build a 3D-model of NIK and to study the binding of pyrazolo[4,3-c]isoquinolines with a view to highlight the structural elements responsible for their inhibitory potency. However, in the course of this work, we unexpectedly found that the pyrazolo[4,3-c]isoquinolines initially reported as NIK inhibitors were neither inhibitors of this enzyme nor of the alternative NF-κB pathway, but were in fact inhibitors of another kinase, the TGF-β activated kinase 1 (TAK1) which is involved in the classical NF-κB pathway.

1. Introduction

Rheumatoid arthritis (RA) is a systemic autoimmune disease affecting around 1–2% of worldwide population. Patients with RA have an increased risk of early death. This pathology is mainly characterized by an uncontrolled proliferation and accumulation of inflammatory cells within the synovial fluids, causing cartilage and bone resorption. Many cell types contribute to the pathogenesis ranging from lymphocytes to stroma cells [1]. These cells express a panel of inflammatory mediators that activate multiple signaling pathways. Most of these signaling pathways lead to the activation of the transcription factor NF-κB and MAPK cascade.

It was recently shown that two main pathways control the activation of NF-κB. The first one, named classical NF-κB pathway, is triggered by inflammatory cytokines such as TNFα or IL-1, or by bacterial and viral proteins through pathogen-recognition receptors (PRR) like TLRs and NLRs [2]. These inducers trigger the recruitment of specific adaptor proteins to their cognate receptors, which enable the activation of a cascade of kinases. Among them, TGF-β activated kinase 1 (TAK1) plays a key role at the crossroad of the NF-κB and MAPK signaling pathways (Fig. 1). TAK1 was first discovered as a TGF-β activated kinase and is part of the MAP kinase subfamily [3]. However, recent studies showed that IL-1β and TNFα signaling pathways are affected in TAK1 KO mice [4,5]. TAK1 activates the IKK complex by phosphorylating the subunit IKKβ and acts on MKK6 to trigger the activation of p38 and JNK (Fig. 1). Upon TAK1 activation, the IKK complex phosphorylates IκBα, the main inhibitor of the classical NF-κB pathway, releasing NF-κB (e.g.; p50/p65), which finally, translocates into the nucleus [6]. This pathway is activated within minutes and relies on the indispensable adaptor protein NEMO, or IKKγ, holding together IKKβ and IKKα to form the IKK complex.

The second NF-κB pathway, called alternative NF-κB pathway, is induced by a subset of TNFL family members as well as by some viral proteins [7]. This pathway is dependent on the stabilization and activation of the kinase NIK. The half-life of this particular kinase is negatively controlled by TRAF-2, TRAF-3, c-IAP-1 and c-IAP-2 [8,9]. Upon activation of receptors like CD40, BAFF or LTβR, the inhibitory function of TRAF-2 and -3 is alleviated. Then, stabilized NIK activates IKKα leading to the processing of p100 into p52 [10–12]. The latter, in association with its main partner Rel-B, fulfils non-redundant biological functions such as secondary lymphoid organ development and induction of specific chemokines involved in adaptive immunity [7].

Because a wide variety of pro-inflammatory cytokines play a role in the development of RA, it might be valuable to design a novel class of inhibitors targeting proteins at the crossroad of multiple pathways relevant to this pathology. Among the potential proteins, NIK certainly represents an attractive candidate since it is

* Corresponding author. Tel.: +32 81724338; fax: +32 4 81724299.
E-mail address: bernard.masereel@fundp.ac.be (B. Masereel).
[1] These authors equally contributed to this work.

0006-2952/$ – see front matter © 2010 Elsevier Inc. All rights reserved.
doi:10.1016/j.bcp.2010.01.007

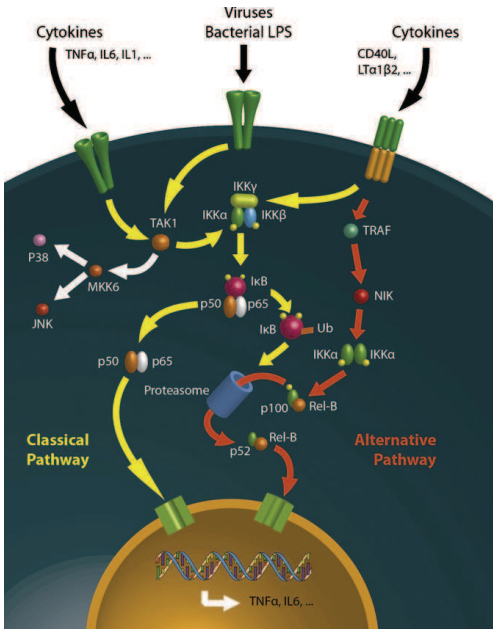

Fig. 1. Classical (yellow) and alternative (orange) NF-κB activation pathways.

involved downstream of many TNFR like CD40, RANK or LTβR involved in the pathogenesis of RA.

According to our knowledge, presently only one series of compounds has been claimed as NIK inhibitors. These are characterized by a pyrazolo[4,3-c]isoquinoline ring substituted in position 1, 3, 5, 7 and 9 (Fig. 2) [13]. Most of the chemical modifications around the pyrazolo[4,3-c]isoquinoline template involved the introduction of bulky, lipophilic groups such as phenyl, trifluoromethylphenyl, pyridine or pentafluorophenyl in the 5-position and introduction of small lipophilic groups like a methyl or a trifluoromethyl in the 1- and 5-positions. Unfortunately, poor information was given in the original patent relating to their biological evaluation. For instance, the claimed NIK inhibitory potency is only based on a whole cellular assay in presence of some derivatives. No data on isolated NIK enzyme are available.

At a structural point of view, the 3D-structure of NIK has not yet been elucidated. The NIK amino acid sequence is comprised of 947 residues with a kinase domain containing 256 residues (400 to 655). Thus, the absence of any 3D-structure of this enzyme hindered the discovery of novel NIK inhibitors.

In this work, we aimed to build a 3D-model of NIK and to study the binding of the reported pyrazolo[4,3-c]isoquinolines with a view to highlight the structural elements responsible for their inhibitory potency. This would help us to subsequently search for novel and more potent inhibitors of this enzyme using the gathered information.

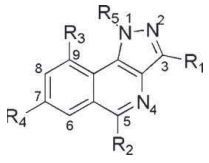

Fig. 2. Chemical structure of the pyrazolo[4,3-c]isoquinoline scaffold reported by Flohr as NIK inhibitors [13].

However, in the course of this work, we unexpectedly found that the pyrazolo[4,3-c]isoquinolines initially reported as NIK inhibitors were neither inhibitors of this enzyme nor of the alternative NF-κB pathway, but were in fact inhibitors of another kinase, the TGF-β activated kinase 1 (TAK1) which is involved in the classical NF-κB pathway. This was confirmed by the re-synthesis and the enzymatic evaluation of representative pyrazolo[4,3-c]isoquinolines. These results strongly suggesting a completely different mechanism of action for the pyrazolo[4,3-c]isoquinolines in modulating the NF-κB pathway, and allow to review the state-of-the-art of NIK inhibitors and should without any doubt be of value for scientists working in this field.

2. Material and methods

2.1. Homology modeling

The human M3K14 (NIK) sequence was obtained from the Swiss-Prot database (primary accession number Q99558). Sequence alignment was performed using *BLASTP* [14], through the Protein Data Bank (BLOSUM62 matrix) [15]. The human PAK1 (PDB code 1YHW_A) was selected as the most appropriate template, and amino acid sequences were then aligned by means of the *ESyPred3D* program [16]. Quality of the model has been analysed by means of PDBsum server, and the Ramachandran plot is available in supporting information [17]. To take into account protein flexibility, the resulting model was minimized using the *MINIMIZE* module included in *SYBYL 8.0* program [18].

2.2. Docking simulations

Compounds **6a–s** were built using the *SKETCH* module, as implemented in *SYBYL* (version 8.0) [18], and their geometry was optimized using *MINIMIZE* module. The minimization process uses *POWELL* method with the *TRIPOS* force field (dielectric constant 1*r*) to reach a final convergence of 0.01 kcal mol^{-1}. Docking simulation was then performed into the homology model of the human kinase NIK with the automated *GOLD* program. The active site was defined including all residues in a volume of 7 Å around 3-OH-staurosporine superimposed onto the model of NIK.

A similar procedure was used to dock **6d** inside the TAK1 binding cleft using the 3D-coordinates obtained from X-ray diffractions [19]. In the case of TAK1, the active site was defined by a sphere of 15 Å around residue A107 in the active site.

2.3. Chemistry

^{1}H NMR spectra were recorded at 20 °C in $CDCl_3$ or DMSO-d_6 on a 400 MHz Jeol Spectrometer (Jeol JNM EX-400). Chemical shifts are reported in δ ppm relative to tetramethylsilane (TMS) as a singlet at 0 ppm (δ). Thin-layer chromatography (TLC) was performed on aluminum supported 0.25 mm silica gel plates (Merck 5719, 250 meshes). TLC plates were visualized under 254 nm and 320 nm UV light. Elemental analyses (C, H, N) were performed on a Thermo Finnigan FlashEA 1112 apparatus. Mass spectra were recorded on an 1100 series MSD Trap spectrometer equipped with an electrospray ionization (ESI) source. Flash chromatography purifications were performed on a Biotage SP1 Purification System using silica or C18 Biotage FLASH+® Cartridges. Microwave assisted reactions were performed using an Initiator 16 Single-mode Microwave system producing a 2.450 GHz controlled irradiation (Biotage AB, Uppsala). The

Please cite this article in press as: Mortier J, et al. Pyrazolo[4,3-c]isoquinolines as potential inhibitors of NF-κB activation. Biochem Pharmacol (2010), doi:10.1016/j.bcp.2010.01.007

temperature was measured with an IR sensor on the outside of the reaction vial.

The purity of compounds **6a–d** was also verified by LC on an Agilent 1100 series system. System control, data collection and data processing were accomplished using ChemStation software (Agilent Technologies, Santa Clara). The mobile phase contained acetonitrile and acetic acid (0.1%). Compounds were detected and their purity was calculated using a UV detector (wavelength: 240 nm). Two different methods were used to analyse the reported compounds. Method 1: injection volume = 3 μL in acetonitrile; gradient elution from 5% to 95% of acetonitrile over 2.4 min, then 95% acetonitrile until 3.6 min; analytical column C8 Zorbax Eclipse Plus (4.6 mm × 50 mm, 1.8 μm particle size); flowrate = 1.25 mL min^{-1}; 1; temperature = 40 °C. Method 2: injection volume = 5 μL in acetonitrile; gradient elution from 5% to 95% of acetonitrile over 4.5 min, then 95% acetonitrile until 8.0 min; analytical column C18 Zorbax SB column (3.0 mm × 100 mm, 3.5 μm particle size); flowrate = 0.5 mL min^{-1}; temperature = 40 °C. Retention times were reported as Rt_1 and Rt_2 for these two methods respectively.

2.3.1. 1,3-Diphenyl-propane-1,2,3-trione 2-oxime **2b**

240 mg (3.46 mmol) of sodium nitrite were dissolved in water (2 mL) and added dropwise to a solution of 130 mg (0.58 mmol) of dibenzoylmethane **1b** diluted into acetic acid (10 mL). At room temperature, the solution was stirred for 1 h. The reaction mixture was extracted three times with diethyl ether (20 mL). The organic layers were combined and washed with a saturated aqueous solution of sodium bicarbonate (30 mL). Solvents were evaporated under reduced pressure, and the crude product purified by flash chromatography to give the title compound (Silica column; Eluant AcOEt: cyclohexane with gradient from 8% to 30% of AcOEt over 30 min; Flowrate 40 mL min^{-1}). Yield: 81%. ^{1}H RMN (DMSO-d_6, 400 MHz): δ = 7.52–7.58 (m, 4H, H_{arom}), 7.68 (t, 2H, H_{arom}), 7.82 (d, 2H, H_{arom}), 7.99 (d, 2H, H_{arom}). Anal. Calcul. for $C_{15}H_{11}NO_3$: C, 71.14; H, 4.38; N, 5.53. Found: C, 71.29; H, 4.62; N, 5.23. *m/z* 254.0 $[M + H]^+$, 276.1 $[M + Na]^+$

2.3.2. 4-Amino-3-methyl-5-phenyl-1H-pyrazole **3a**

At 0 °C, hydrazine hydrate (0.18 mL, 3.70 mmol) was added dropwise to a solution of 1-phenylbutane-1,2,3-trione-2-oxime **2a** (0,37 mmol) in ethanol (4 mL). Then, the mixture was stirred for 7 h at room temperature. Solvents were removed under reduced pressure and the crude product diluted in ethyl acetate (10 mL). The solution was acidified by HCl 3N (15 mL) and the organic layer discarded. The aqueous layer was neutralized by NaOH 1N (50 mL) and extracted with ethyl acetate (3 × 20 mL). The organic layers were combined, dried, and the solvent evaporated under reduced pressure. The crude product was purified by flash chromatography (Silica column; eluant: AcOEt:cyclohexane from 20% to 100% of AcOEt over 45 min; flowrate: 40 mL min^{-1}). Yield: 86%. ^{1}H RMN ($CDCl_3$, 400 MHz): δ = 2.37 (s, 3H, CH_3), 7.31 (t, 1H, H_{arom}), 7.42 (t, 2H, H_{arom}), 7.61 (d, 2H, H_{arom}). Anal. Calcul. for $C_{10}H_{11}N_3$: C, 69.34; H, 6.40; N, 24.26. Found: C, 69.30; H, 6.14; N, 23.56. *m/z* 174.1 $[M + H]^+$.

2.3.3. 4-Amino-3,5-diphenyl-1H-pyrazole **3b**

The title compound was synthesized with the same procedure than that used for **3a**. Yield: 88%. ^{1}H RMN ($CDCl_3$, 400 MHz): δ = 7.25 (t, 2H, H_{arom}), 7.48 (t, 4H, H_{arom}), 7.68 (d, 4H, H_{arom}). Anal. Calcul. for $C_{15}H_{13}N_3$: C, 76.57; H, 5.57; N, 17.86. Found: C, 76.27; H, 5.65; N, 17.62. *m/z* 236.2 $[M + H]^+$.

2.3.4. 4-Benzamido-3,5-diphenyl-1H-pyrazole **5a**

Benzoic acid **4a** (92.6 mmol), hydroxybenzotriazole (HOBt; 185 mmol) and *N*-(3-dimethylaminopropyl)-*N*′-ethylcarbodiimide (DEC; 79.5 mmol) were added to 4-amino-3,5-diphenyl-1H-pyrazole **3b** (92.6 mmol) diluted in dichloromethane (30 mL). Two drops of $BMimpF_6$ were added, and the mixture was heated in the microwave oven for 1 h (70 °C). Then, water (20 mL) was added and the mixture extracted by ethyl acetate (3 × 20 mL). The organic layers were combined, dried, and the solvent evaporated under reduced pressure. The crude product was purified by flash chromatography (Silica column; Eluant: AcOEt:cyclohexane from 20% to 71% of AcOEt over 40 min; flowrate: 40 mL min^{-1}). Yield: 60% ^{1}H RMN ($CDCl_3$, 400 MHz): δ = 7.28–7.46 (m, 6H, H_{arom}), 7.49 (t, *J* = 7.3 Hz, 2H, H_{arom}), 7.56 (t, *J* = 7.3 Hz, 1H, H_{arom}), 7.64 (d, *J* = 6.3 Hz, 2H, H_{arom}), 7.72 (d, *J* = 6.3 Hz, 2H, H_{arom}), 7.92 (d, *J* = 7.3 Hz, 2H, H_{arom}), 9.96 (s, 1H, HN_{amide}). Anal. Calcul. for $C_{22}H_{17}N_3O{\cdot}H_2O$: C, 73.93; H, 5.36; N, 11.76. Found: C, 74.03; H, 5.13; N, 11.42. *m/z* 340.2 $[M + H]^+$, 362.2 $[M + Na]^+$.

2.3.5. 4-(3-Methoxybenzamido)-3,5-diphenyl-1H-pyrazole **5b**

The title compound was synthesized from 3-methoxybenzoic acid **4b** and 4-amino-3,5-diphenyl-1H-pyrazole **3b** as starting material, and according to the same procedure than that described for **5a**. Yield: 60%. ^{1}H RMN (DMSO-d_6, 400 MHz): δ = 3.77 (s, 3H, OCH_3), 7.12 (d, *J* = 8.2 Hz, 1H, H_{arom}), 7.26–7.45 (m, 8H, H_{arom}), 7.52 (d, *J* = 7.3 Hz, 1H, H_{arom}), 7.64 (d, *J* = 7.3 Hz, 2H, H_{arom}), 7.72 (d, *J* = 7.3 Hz, 2H, H_{arom}), 9.94 (s, 1H, HN). Anal. Calcul. for $C_{23}H_{17}N_3O$: C, 78.61; H, 4.88; N, 11.96; C, 78.04; H, 5.19; N, 11.58. *m/z* 369.2 $[M + H]^+$, 391.3 $[M + Na]^+$.

2.3.6. 4-(3-Methoxybenzamido)3-methyl-5-phenyl-1H-pyrazole **5c**

The title compound was synthesized from 3-methoxybenzoic acid **4b** and 4-amino-3-methyl-5-phenyl-1H-pyrazole **3a** as starting material, and according to the same procedure than that described for **5a**. Yield: 57%. ^{1}H RMN (DMSO-d_6, 400 MHz): δ = 2.08 (s, 3H, CH_3), 3.78 (s, 3H, OCH_3), 7.12 (d, *J* = 8.2 Hz, 1H, H_{arom}), 7.22–7.41 (m, 4H, H_{arom}), 7.49 (s, 1H, H_{arom}), 7.54 (d, *J* = 7.5 Hz, 1H, H_{arom}), 7.6–7.7 (m, 2H, H_{arom}), 9.69 (s, 1H, HN). Anal. Calcul. for $C_{18}H_{17}N_3O_2$: C, 70,34; H, 5,58; N, 13,67. Found: C, 70,51; H, 5,35; N, 13,36. *m/z* 308.2 $[M + H]^+$.

2.3.7. 4-Benzamido-3-methyl-5-phenyl-1H-pyrazole **5d**

The title compound was synthesized from benzoic acid **4a** and 4-amino-3-methyl-5-phenyl-1H-pyrazole **3a** as starting material, and according to the same procedure than that described for **5a**. Yield: 75%. ^{1}H RMN ($CDCl_3$, 400 MHz): δ = 2.26 (s, 3H, CH_3), 7.34–7.51 (m, 6H, H_{arom}), 7.61 (d, *J* = 8.2 Hz, 2H, H_{arom}), 7.71 (d, *J* = 7.5 Hz, 1H, H_{arom}), 7.83 (d, *J* = 8.2 Hz, 1H, H_{arom}). Anal. Calcul. for $C_{17}H_{15}N_3O{\cdot}1/2H_2O$: C, 71.31; H, 5.63; N, 14.68. Found: C, 72.07; H, 5.33; N, 14.53. *m/z* 278.1 $[M + H]^+$.

2.3.8. 3,5-Diphenyl-1H-pyrazolo[4,3-c]isoquinoline **6a**

4-Benzamido-3,5-diphenyl-1H-pyrazole **5a** (0.36 mmol) and phosphorus pentoxyde (3.60 mmol) were suspended in dry chlorobenzene (10 mL) and *N*,*N*-diethylaniline (0.36 mmol). Under argon atmosphere, the mixture was warmed up to 120 °C and phosphorus oxychloride (0.54 mmol) was added dropwise. The temperature was maintained for 24 h. At the end, a saturated solution of sodium bicarbonate (10 mL) was carefully added, and the mixture was extracted by dichloromethane (3 × 20 mL). The organic layers were combined, dried on magnesium sulfate and the solvent was evaporated under reduced pressure. The crude product was purified by preparative HPLC (C18 column and isocratic mobile phase MeCN: AcOH 0.1% 50:50) to give the title compound **6a**. Yield: 2%. *m/z* 340.2 $[M + H]^+$, 362.2 $[M + Na]^+$. ^{1}H RMN ($CDCl_3$, 400 MHz): δ = 7.35 (t, *J* = 7.5, 1H, H_{arom}), 7.46–7.71 (m, 9H, H_{arom}), 7.97 (t, *J* = 8.2 Hz, 1H, H_{arom}), 8.04 (d, *J* = 7.5 Hz, 1H, H_{arom}), 8.51 (d, *J* = Hz, 2H, H_{arom}). Rt_1 = 3.35 min; Rt_2 = 7.49 min *m/z* 352.2 $[M + H]^+$.

Please cite this article in press as: Mortier J, et al. Pyrazolo[4,3-c]isoquinolines as potential inhibitors of NF-κB activation. Biochem Pharmacol (2010), doi:10.1016/j.bcp.2010.01.007

2.3.9. 5-(3-Methoxyphenyl)-3-phenyl-1H-pyrazolo[4,3-c]isoquinoline **6b**

The title compound was synthesized from 4-(3-methoxybenzamido)-3,5-diphenyl-1H-pyrazole **5b** as starting material and according to the procedure described for compound **6a**. Yield: 7%. ^{1}H RMN ($CDCl_3$, 400 MHz): δ = 3.81(s, 3H, OCH_3), 7.11 (dd, J_1 = 2.2 Hz, J_2 = 8.1 Hz, 1H, H_{arom}), 7.20–7.24 (m, 1H, H_{arom}), 7.21 (d, J_1 = 2.2 Hz, 1H, H_{arom}), 7.35 (t, J = 7.3 Hz, 1H, H_{arom}), 7.46–7.50 (m, 3H, H_{arom}), 7.70 (t, J = 7.7 Hz, 1H, H_{arom}), 7.95 (t, J = 7.7 Hz, 1H, H_{arom}) 8.06 (d, J = 8.4 Hz, 1H, H_{arom}), 8.52–8.50 (m, 3H, H_{arom}). Rt_1 = 3.30 min; Rt_2 = 7.38 min m/z 352.2 $[M + H]^+$.

2.3.10. 5-(3-Methoxyphenyl)-3-methyl-1H-pyrazolo[4,3-c]isoquinoline **6c**

The title compound was obtained from 4-(3-methoxybenzamido)-3-methyl-5-phenyl-1H-pyrazole **5c** as starting material and according to the procedure described for compound **6a**. Yield: 6%. ^{1}H RMN ($CDCl_3$, 400 MHz): δ = 2.76 (s, 3H, CH3), 3.87 (s, 3H, OCH3), 7.03 (d, J = 10.8 Hz, 1H, H_{arom}), 7.21–7.28 (m, 2H, H_{arom}), 7.44 (t, J = 12.1 Hz, 1H, H_{arom}), 7.59 (t, J = 10.8 Hz, 1H, H_{arom}), 7.81 (t, J = 10.8 Hz, 1H, H_{arom}), 8.13 (d, J = 12.1 Hz, 1H, H_{arom}), 8.22 (d, J = 12.1 Hz, 1H, H_{arom}). Rt_1 = 2.78 min; Rt_2 = 6.15 min. m/z 289.3 $[M + H]^+$.

2.3.11. 3-Methyl-5-phenyl-1H-pyrazolo[4,3-c]isoquinoline **6d**

The title compound was synthesized from 4-benzamido-3-methyl-5-phenyl-1H-pyrazole **5d** as starting material and according to the procedure described for compound **6a**. Yield: 13%. ^{1}H RMN ($CDCl_3$, 400 MHz): δ = 2.76 (s, 3H, CH3), 7.51–7.60 (m, 4H, H_{arom}), 7.68 (d, J = 7.5 Hz, 2H, H_{arom}), 7.78 (t, J = 7.5 Hz, 1H, H_{arom}), 8.10 (d, J = 8.5 Hz, 1H, H_{arom}), 8.22 (d, J = 7.5 Hz, 1H, H_{arom}). Rt_1 = 2.78 min; Rt_2 = 6.15 min. m/z 260.1 $[M + H]^+$.

2.4. NIK enzymatic assay

This experiment was performed by ProQinase using 33PanQinase® technology [31]. Inhibitory potency of staurosporine and molecules **6a–d** were evaluated on human recombinant NIK. DMSO was used as cosolvent and its final concentration was 1%. NIK was expressed in Sf9 insect cells as human recombinant GST-fusion protein. The kinase was purified by affinity chromatography using GSH-agarose. The purity of the kinase was checked by SDS-PAGE/silver staining and the identity was verified by mass spectroscopy. The NIK activity was measured as the incorporation on an artificial substrate of ^{33}P produced by hydrolysis of [γ-^{33}P]-ATP. The substrate (RBER-CHKtide) was an artificial fusion protein expressed in *Escherichia coli*. It was consisting of a N-terminal GST-tag separated by a thrombin cleavage site from a fragment of the human retinoblastoma protein RB1, amino acids S773–K928 followed by 11 Arg residues (ER) and a peptide sequence KKKVRSGLYRSPSMPENLNRPR (CHKtide).

2.5. Alternative pathway assay

Human LTβR-positive HeLa cells have been used to evaluate the NIK inhibitory potency expressed as the inhibition of the processing of p100 into p52. Briefly, HeLa cells were cultured in DMEM with 10% FBS and plated in 6 well plates until they reach 80% of confluence. The cells were washed twice with PBS and incubated for 2 h with Opimem-1 containing 10, 20 or 50 μM of inhibitors. DMSO was used as cosolvent at a maximal concentration of 0.5% (v/v). At this concentration, DMSO has no effect. Then, an antibody acting as agonist of human LTβR (R&D Systems, Inc.) was added for 5 h. Afterwards, the cells were washed twice with PBS and lysed in SDS 0.5% containing a cocktail of protease and phosphatase inhibitors (Complete and PhosStop, Roche). Protein extracts were quantified (Micro BCA protein kit assay, Pierce) and equal amounts of protein (15 μg) were loaded on SDS-PAGE for analyzing the processing of p100 into p52. For detecting p100 and p52, an antibody anti-human p52 (Upstate Cell Signaling 05-361) was used and a goat anti-mouse HRP (DAKO) was used as secondary antibody prior to measurement of the signal by chemiluminescence using the ECL kit from Pierce.

2.6. Multikinase assay

KinaseProfiler™ is a millipore technology using standard protocole.

2.7. TAK1 enzymatic assay

This experiment was performed by Invitrogen using LanthaScreen® Kinase Binding Assay technology [32]. The test compounds were screened in 1% DMSO as final concentration. 3-fold serial dilutions were conducted from the starting concentration. All kinase/antibody mixtures were diluted to a 2× working concentration in the appropriate kinase buffer. The 4× AlexaFluor® labeled tracer was prepared in kinase buffer and the read out was on fluorescence plate reader.

2.8. Classical pathway assay

HeLa cells were cultured in DMEM with 10% FBS and plated in 6 well plates until they reach 80% of confluence. The cells were washed twice with PBS and incubated for 2 h with Opimem-1 containing 50 μM of inhibitor or DMSO alone. Then, TNF-α (Pepro Tech Inc.) was added at 100 U/mL for 0, 1 or 2 h. Total RNA samples were isolated with the Tripure reagent (Roche Molecular Biochemicals). One microgram of RNA was submitted to reverse transcription using M-MLV reverse transcriptase and random primers (Invitrogen) in a total volume of 20 μL. Two microliters of cDNA were submitted to real-time PCR using TaqMan 7000 SDS (Applied Biosystems) and SYBR Green detection (Eurogentec). The results were normalized with the 18S transcript. PCR was performed with the following primers for the following human transcript: *il-6*: FW 5′-CCAGGAGCCCAGCTATGAAC-3′ and RV 5′-CCCAGGGAGAAGGCAACTG-3′, *TNFα*: FW 5′-GGAGAAGGGTGACCGACTCA-3′ and RV 5′-TGCCCAGACTCGGCAAAG-3′ and *18S*: FW 5′-AACTTTCGATGGTAGTCGCCG-3′ and RV 5′-CCTTGGATGTGGTAGCCGTTT-3′.

3. Results

3.1. Building of a 3D-model of NIK

Since no experimentally-derived structural data for NIK were reported to date, a molecular model of this enzyme was first developed using comparative modeling. This technique comprises four main steps: (i) identification of a template, *i.e.* a protein of known 3D-structure that shares sequence homology with the target protein, (ii) alignment of the sequences of the target and template, (iii) building and optimization of the 3D-model and finally, (iv) quality assessment of the resulting structure. Following a *BLASTP* alignment, we identified the protein PAK1 (p21 activated kinase 1; PDB code: 1YHW_A) [20] as the best template. This protein shares 30% sequence identity and up to 48% sequence homology (similar residues) with NIK. As the target/template alignment step is known to be critical to the quality of the models, we used the automated homology program *ESyPred3D* [16]. This performs a consensus alignment between the sequences of the target, the template and other homologous proteins with the help of several different alignment algorithms and then uses *MODELLER*

Please cite this article in press as: Mortier J, et al. Pyrazolo[4,3-c]isoquinolines as potential inhibitors of NF-κB activation. Biochem Pharmacol (2010), doi:10.1016/j.bcp.2010.01.007

[21] to generate the 3D-coordinates. The overall quality of the resulting models was finally evaluated using different methods. Ramachandran plots (available as Supporting Information) proved to be very satisfactory with 90.2% residues located in the most favored regions, 7.3% in the allowed regions, only four residues (1.6%) in the generously allowed regions (Phi and Psi torsion angles slightly larger than usual) and two residues in the disallowed regions (unfavorable Phi and Psi torsion angles). It should be noted that these six residues (Q484, T401, Y391, E395, D544 and S572) are located far from the active site and the hinge region.

A superimposition of NIK with PAK1 (Fig. 3) shows that the overall folding pattern (β-sheets, helices and main loops) is well preserved. The ATP-binding site region is also highly preserved. First, active site residues common to all serine–threonine kinases were identified. In the NIK structure, M469, which corresponds to M344 in PAK1, was identified as the gatekeeper (gk) residue. It is one of the essential residues in the ATP-binding site. Indeed, the nature of the gatekeeper (size and volume of the side-chain) is variable from one kinase to another, thus dictating the access to a specific pocket of the ATP-binding site (specificity pocket). Then, residues E470 (gk + 1) and L472 (gk + 3) which correspond to residues E345 and L347 in PAK1, were respectively identified in the hinge region [22]. These two residues are responsible for the stabilization of the adenine moiety of ATP. In the co-crystal structure of the complex between PAK1 and 3-OH-staurosporine (PDB code 2HY8), both residues are involved in the stabilization of the aromatic ring of 3-OH-staurosporine. Finally, in the back of the active site cavity, a salt bridge between residues K429 and E440 corresponding to the salt bridge between R299 and E315 in PAK1 is also highly preserved.

The catalytic pocket of NIK was refined by minimization to take into account the protein flexibility. The position of the side-chains of the residues located 20 Å around L472 were minimized by mean of the *MINIMIZE* module as implemented in *SYBYL 8.0* [18].

To appraise the reliability of our model, the binding of the previously reported pyrazolo[4,3-c]isoquinolines was studied within the modeled active site. Staurosporine, which is known as a pankinase inhibitor including NIK [24] was also studied in our model. At a structural point of view, staurosporine is far from the template of the synthesized pyrazolo[4,3-c]isoquinolines.

3.2. Docking of pyrazolo[4,3-c]isoquinolines into the 3D-model of NIK

The pyrazolo[4,3-c]isoquinolines **6a–s** (Table 1) and staurosporine were docked inside the ATP-binding site of NIK using the automated *GOLD* program [25]. For each molecule, 20 conformations were generated and further evaluated following two parameters: (i) the number of different orientations adopted by one molecule inside the NIK binding cleft and (ii) the number of different orientations where the compound is found to be stabilized with at least one H-bond with the residue L472 in the hinge region.

Interestingly, staurosporine fits perfectly the catalytic pocket, adopting a similar binding orientation as observed for 3-OH-staurosporine in PAK1 (Fig. 3). All of the 20 conformations generated lie in the same orientation with two H-bonds between the lactam ring of staurosporine and the NH and CO moieties of L472 and E470, respectively, stabilizing the moiety (Fig. 4a and b). In addition, hydrophobic interactions with aliphatic residues L406, V414, A427, L522 and C533 (not shown here for clarity) also contribute to the stabilization on both sides of the aromatic plane.

Conversely, when pyrazolo[4,3-c]isoquinolines **6a–s** are docked inside the ATP-binding site of NIK, several different orientations (2–6) were observed for each compound (Table 1), except for **6f** and **6r** for which a unique binding orientation of the pyrazolo[4,3-c]isoquinoline motif was found. But these two compounds did not interact with L472 through an H-bound as requested. In addition, in some cases, the inhibitor is not stabilized through H-bond interaction(s) with the hinge region residue L472. This interaction was however shown to be critical for kinase inhibition [22]. To see if an unique orientation could be highlighted, compounds **6a–s** were docked again inside the NIK binding cleft imposing a H-bond between the NH of L472 and one acceptor atom of the ligand. By doing so, two orientations (orientation 1 and orientation 2) were found as illustrated in Fig. 4 using compound **6d** as an example (Fig. 4c and d for orientation 1, and Fig. 4e and f for orientation 2). Although in both orientations the pyrazolo[4,3-c]isoquinoline scaffold is well stabilized by two H-bonds in the hinge region (as expected following a constraint docking), none of these two orientations seems more plausible than the other or would allow a better understanding of the structure–activity relationships in this series. Thus, this docking study does not allow to highlight an unique, obvious orientation of compounds **6a–s** into the NIK binding cavity.

Based on these observations, different hypothesis could be suggested: (i) although staurosporine, a true NIK inhibitor (discussed later), fits perfectly its active site, the 3D-model of NIK is not reliable, (ii) the pyrazolo[4,3-c]isoquinolines **6a–s** are effectively NIK inhibitors but through a different mechanism of inhibition, for instance through interaction with an allosteric site or (iii) the pyrazolo[4,3-c]isoquinolines are devoid of NIK inhibitory potency. To assess this assumption, some representative pyrazolo[4,3-c]isoquinolines (**6a–d**) were synthesized and their NIK inhibitory potency evaluated on isolated human recombinant

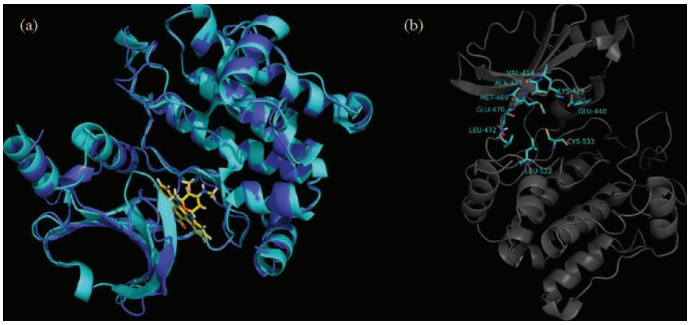

Fig. 3. (a) Superimposition of PAK1 (cyan) with 3-OH-staurosporine (yellow) and NIK (blue) and (b) view of NIK with main active site residues in cyan. Pictures made using PYMOL [23].

Please cite this article in press as: Mortier J, et al. Pyrazolo[4,3-c]isoquinolines as potential inhibitors of NF-κB activation. Biochem Pharmacol (2010), doi:10.1016/j.bcp.2010.01.007

Table 1
Structure and docking results for the pyrazolo[4,3-c]isoquinolines **6a–s**.

Cmpd	R_1	R_2	R_3	R_4	R_5	Docking	
						Number of different orientations	Number of different orientations with H-bond with L472
Staurosporine						1	1
6a			H	H	H	4	1
6b		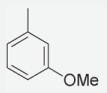	H	H	H	6	2
6c	Me	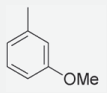	H	H	H	2	0
6d	Me		H	H	H	2	0
6e	Me	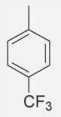	H	H	H	3	0
6f	Me		H	H	Me	1	0
6g	CF_3		H	H	H	2	0
6h	Me	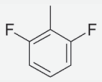	H	H	Me	2	1
6i	Me		H	COOMe	H	4	2
6j	Me		H	COOMe	H	3	2
6k	Me		H	H	Me	3	0
6l	Me		H	NMe_2	H	2	0

Please cite this article in press as: Mortier J, et al. Pyrazolo[4,3-c]isoquinolines as potential inhibitors of NF-κB activation. Biochem Pharmacol (2010), doi:10.1016/j.bcp.2010.01.007

Table 1 (*Continued*)

Cmpd	R_1	R_2	R_3	R_4	R_5	Docking	
						Number of different orientations	Number of different orientations with H-bond with L472
6m	Me		CF_3	H	H	2	1
6n	Me		CF_3	H	H	4	2
6o	Me	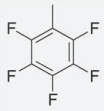	H	H	H	4	1
6p	Me		H	NMe_2	H	3	2
6q	Me	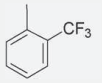	H	H	H	4	1
6r	Me	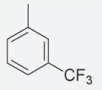	H	H	H	1	0
6s	Me	CH_2OMe	H	H	H	5	1

enzyme as well as on HeLa cells where the NF-κB alternative pathway was induced.

3.3. Chemistry

The pyrazolo[4,3-c]isoquinolines **6a–d** were synthesized in four steps (Scheme 1). Starting from the commercially available diketones **1a–b**, oximes **2a–b** were prepared with a high yield by reaction of sodium nitrite in acidic conditions [26]. The oximes **2a–b** further reacted with hydrazine hydrate to form pyrazoles **3a–b** [26,27]. Then, benzoic acids **4a–b** activated by HOBT/DEC were condensed on pyrazoles **3a–b** to form the corresponding amides **5a–d**. Finally, the desired pyrazolo[4,3-c]isoquinolines **6a–d** (Table 1) were obtained according to the Pictet-Gams reaction in poor yields due to the formation of several side products during the reaction (Scheme 1) [28].

3.4. Biological evaluation

The NIK inhibitory potency of the prepared pyrazolo[4,3-c]isoquinolines (**6a–d**) was evaluated in two enzymatic systems (i) isolated human recombinant NIK and (ii) cultured HeLa cells where the alternative NF-κB pathway was induced by an LTβR agonist antibody.

3.4.1. Human recombinant NIK inhibition

A radiometric protein kinase assay was used to measure the residual activity of NIK in presence of the synthesized inhibitors at a single concentration of 10 μM. Briefly, NIK was expressed in Sf9 insect cells as human recombinant GST-fusion protein and purified by affinity chromatography using GSH-agarose. The substrate, a recombinant protein kinase (RBER-CHKtide) was also expressed in *E.coli*. The assay cocktails were incubated at 30 °C for 60 min with [γ-^{33}P]-ATP (1 μM, pH 7.5). Incorporation of ^{33}P was measured with a microplate scintillation counter. Staurosporine was chosen as Ref. [24].

Although the inhibition of NIK in the presence of staurosporine was >70%, none of the pyrazoloisoquinolines **6a–d** significantly reduced NIK activity at 10 μM (Table 2). This corroborates the modeling study and demonstrates that the pyrazolo[4,3-c]isoquinolines **6a–d** are not NIK inhibitors.

To confirm that these molecules could not inhibit other proteins of the NF-κB alternative pathway, their inhibition property was then investigated in a cellular assay where the alternative pathway is solely involved.

3.4.2. NF-κB alternative pathway inhibition

Briefly, pyrazolo[4,3-c]isoquinolines **6a–d** were assayed using carcinoma HeLa cells expressing LTβR. The NF-κB alternative pathway was induced or not by an LTβR agonist antibody. After induction, NIK was overexpressed and the processing of p100 into p52 was triggered by phosphorylation of IKKα (Fig. 1). The p100/p52 ratio was finally analysed by Western blot. DMSO, used as cosolvent, has no effect. The results are reported on Fig. 5.

Staurosporine which strongly inhibit isolated human recombinant NIK also blocks this pathway (Fig. 5). Here again, none of the pyrazolo[4,3-c]isoquinolines **6a–d** inhibited the NF-κB alternative pathway. In fact, the processing of p100 into p52 was observed in

Please cite this article in press as: Mortier J, et al. Pyrazolo[4,3-c]isoquinolines as potential inhibitors of NF-κB activation. Biochem Pharmacol (2010), doi:10.1016/j.bcp.2010.01.007

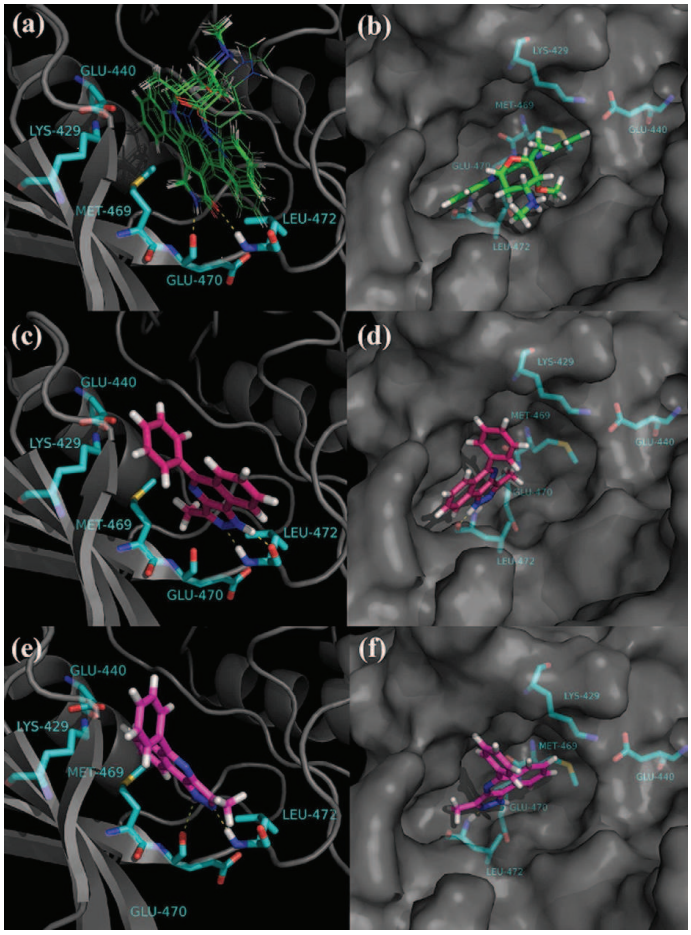

Fig. 4. (a) All of the 20 conformations obtained for staurosporine; (b) view of staurosporine in the active site cavity of NIK illustrated with the Connolly surface; (c and d) view of **6d** in the orientation 1 and (e and f) view of **6d** in the orientation 2 inside the NIK binding cleft. Pictures made using PYMOL [23].

the presence (+) and in the absence (−) of **6a–d** whatever the concentration of the inhibitor used (10, 20 or 50 μM). On the contrary to the claims of the original patent, the pyrazolo[4,3-c]isoquinolines **6a–d** cannot be considered as NIK inhibitors neither as blockers of the NF-κB alternative pathway.

3.4.3. Multikinase assay

With the aim to identify the putative target of the pyrazolo[4,3-c]isoquinolines, a multikinase screening assay was performed. The pyrazolo[4,3-c]isoquinoline **6d** was selected to carry out this study. The inhibitory properties of **6d** were thus evaluated on a panel of 263 kinases (Millipore KinaseProfiler™) at 10 μM.

As a result, an inhibition of at least 50% was observed for 92 kinases over the 263 kinases assayed (data not shown). Interestingly, among these, **6d** particularly decreased (70%) the activity of TAK1, the TGF-β-activated kinase which is involved in the classical NF-κB pathway (see Fig. 1).

3.4.4. TAK1 inhibition

Following this result, the TAK1 dose-inhibitory potency of compounds **6a–d** were evaluated using an Invitrogen Lanthascreen® Eu Kinase Binding Assay [32]. Briefly, this assay is based on the detection of the binding of a "tracer" to a kinase by addition of a Eu-labeled anti-tag antibody. Binding of the tracer and antibody to a kinase results in a high degree of FRET, whereas displacement of the tracer with a kinase inhibitor results in a loss of FRET. The results are reported in Table 3.

As expected, staurosporine, the reference inhibitor in this assay, strongly inhibits TAK1 with an IC_{50} of 0.021 μM. From the four compounds analysed, only two, **6c** and **6d**, effectively inhibit TAK1 with an IC_{50} value of 0.58 and 2.1 μM, respectively, whereas no inhibition was observed at maximum solubility for **6a** and **6b**.

As the 3D-coordinates of TAK1 were recently available (PDB code 2EVA), [19] the molecular interactions stabilizing **6c** and **6d** inside the TAK1 cavity were analysed with a view to identify the structural elements required for their inhibitory potency.

Please cite this article in press as: Mortier J, et al. Pyrazolo[4,3-c]isoquinolines as potential inhibitors of NF-κB activation. Biochem Pharmacol (2010), doi:10.1016/j.bcp.2010.01.007

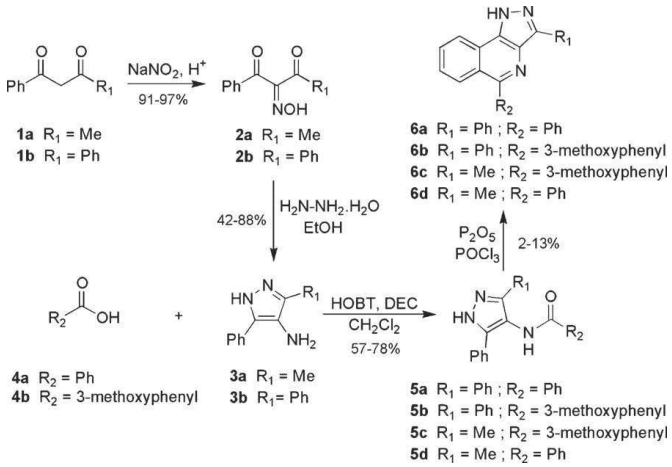

Scheme 1. Synthesis of pyrazolo[4,3-c]isoquinolines.

Table 2
Inhibition of NIK in presence of pyrazolo[4,3-c]isoquinolines **6a–d** at 10 μM. Results are mean of 3 experiments.

Cmpd	NIK inhibition
Staurosporine	72%
6a	6%
6b	0%
6c	18%
6d	2%

Table 3
IC_{50} of pyrazolo[4,3-c]isoquinolines **6a–d** against TAK1 (N.I = no inhibition at maximum solubility).

Cmpd	TAK1 IC_{50} (μM)
Staurosporine	0.021
6a	N.I.
6b	N.I.
6c	0.58
6d	2.1

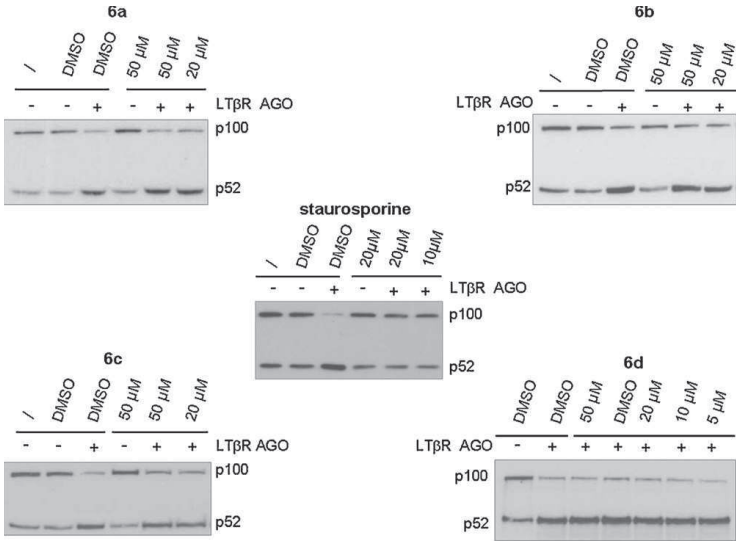

Fig. 5. Processing of p100 into p52 from HeLa cells expressing LTβR stimulated by an LTβR agonist antibody (AGO). Cells were incubated in absence or in presence of pyrazolo[4,3-c]isoquinolines **6a–d** or with staurosporine. DMSO has no effect.

Please cite this article in press as: Mortier J, et al. Pyrazolo[4,3-c]isoquinolines as potential inhibitors of NF-κB activation. Biochem Pharmacol (2010), doi:10.1016/j.bcp.2010.01.007

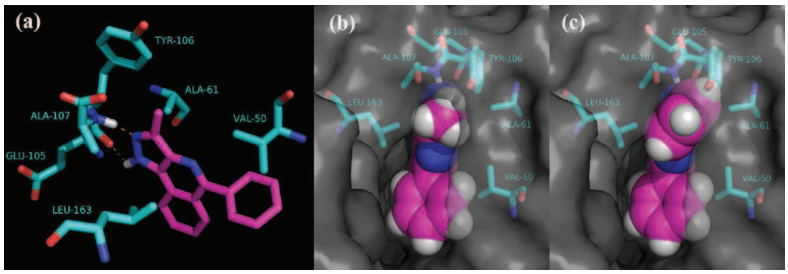

Fig. 6. Molecular interactions between (a) **6d** with stick representation, (b) **6d** and (c) **6a** with sphere representation in the hinge region of TAK1. Pictures made using PYMOL [23].

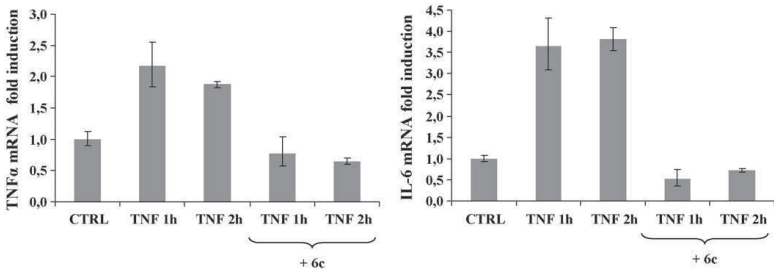

Fig. 7. Normalized TNFα and IL-6 mRNA-levels induced by TNFα (100 U/mL) in absence or in presence of TAK1 inhibitor **6c** (50 μM). Measurements were conducted 1 h and 2 h following TNFα addition. TNFα and IL-6 mRNA-levels prior to TNFα addition (CTRL) are considered as 1. Mean ± s.d.

When **6c** or **6d** are docked inside the TAK1 binding cleft, all of the 20 conformations adopt the same orientation with the pyrazolo[4,3-c]isoquinoline deeply inserted in the cavity and the R_1-methyl (see Fig. 1) pointing towards the entrance of the active site (Fig. 6a). Both compounds are stabilized by (i) two H-bonds with residues E105 and A107 in the hinge region and (ii) hydrophobic interactions with residues V50, A61 and L163 (Fig. 6a and b). Indeed, **6c** and **6d** fits perfectly the TAK1 ATP-binding site.

Interestingly, the inactivity of compounds **6a** and **6b** might be explained by a steric clash between the phenyl group in position R_1 of the pyrazolo[4,3-c]isoquinoline ring and the residue Y106 of TAK1 (Fig. 6c).

This study thus suggest that pyrazolo[4,3-c]isoquinoline are TAK1 inhibitors, at least when they are substituted in position R_1 by a methyl group (**6c–s**). When this methyl is replaced by bulkier group such as a phenyl (**6a–b**), the steric hindrance certainly prevents the compounds to bind TAK1.

3.4.5. NF-κB classical pathway inhibition

Briefly, **6c** (50 μM), the best TAK1 inhibitor (IC_{50} = 0.58 μM), was assayed using carcinoma HeLa cells stimulated by TNFα. The NF-κB classical pathway was induced by TNFα (100 U/mL), then the levels of TNFα and IL-6 mRNA-levels were quantified in presence or in absence of **6c**. As expected (Fig. 7), TNFα doubles the relative TNFα mRNA-level 1 h (2.2-fold) and 2 h (1.9-fold) following induction, whereas the induction in presence of **6c** is only 0.77-fold and 0.65-fold respectively. TNFα strongly increases the relative IL-6 mRNA-level 1 h (3.7-fold) and 2 h (3.8-fold) after TNFα-induction. On the contrary, the addition of **6c** prevents an increase of the normalized IL-6 mRNA-levels which are 0.5-fold and 0.7-fold when measured 1 h and 2 h after induction respectively.

4. Discussion and conclusions

The initial goal of this work was to build a 3D-model of NIK to study a series of known pyrazolo[4,3-c]isoquinolines, claimed as NIK inhibitors, [13] with a view to elucidate the required structural elements for NIK inhibition. In the absence of any experimental structural data on this enzyme, we built a 3D-model of NIK by using comparative modeling techniques. The binding of known pyrazolo[4,3-c]isoquinolines was directly analysed in the putative active site. Surprisingly, this study revealed a poor binding orientation of the template inside the ATP-binding pocket of NIK. This suggested either a poor inhibitory potency or an alternative mechanism of inhibition. Based on the modeling results, we synthesized some pyrazolo[4,3-c]isoquinolines and characterized their inhibitory activity in two tests involving NIK: (i) an isolated enzyme assay using human recombinant NIK and (ii) a cellular assay where the alternative NF-κB pathway only was involved. As a result, all synthesized molecules were completely deprived of any significant inhibition on both systems. On the contrary to the original patent, this confirmed these compounds were neither inhibitor of NIK nor even of the alternative NF-κB activation pathway. To elucidate the potential target of these pyrazolo[4,3-c]isoquinolines, in modulating the NF-κB pathway, a multikinase screen was performed using **6d** as example. This screening revealed interesting inhibition properties of **6d** for TAK1, a kinase which is involved in the classical NF-κB activation pathway. This was further confirmed by determination of the inhibition (IC_{50}) of **6a–d** *vs.* TAK1. By preventing the increase of the TNFα and IL-6 mRNA-levels induced by TNFα, the best TAK1 inhibitor **6c** (IC_{50} = 0.58 μM) confirmed its ability to block the classical NF-κB pathway.

Indeed, in the original patent, [13] the NIK inhibitory potency claimed by Flohr was based on the ability of

Please cite this article in press as: Mortier J, et al. Pyrazolo[4,3-c]isoquinolines as potential inhibitors of NF-κB activation. Biochem Pharmacol (2010), doi:10.1016/j.bcp.2010.01.007

pyrazolo[4,3-c]isoquinolines to prevent TNFα and IL-6 release from human peripheral blood lymphocytes after stimulation by LPS or IL1β. On the contrary, the present study demonstrated that pyrazolo[4,3-c]isoquinolines are not NIK inhibitors but are likely modulators of the classical NF-κB pathway through TAK1 inhibition. These results are of particular importance as they allow to re-assess the mechanism of inhibition in this series. Moreover it should be noted that recent results from Tang et al. showed that conditional deletion of TAK1 in knockout mice led to multiple organ defects during development and to death after 8–10 days [29,30]. This suggests that inhibition of TAK1 is certainly not advantageous.

Finally, this study led to a reliable 3D-model of NIK that could be used to search for novel inhibitors of this enzyme.

Acknowledgments

The authors thank C. Bertolla and J. Deglim for configuring LC Methods; A-M. Murray for performing elemental analysis; C. Swijsen for designing NF-κB activation pathways scheme; the "Fonds de la Recherche Scientifique – FNRS" for funding the Biotage SP1 Purification System; the Walloon Region for financially supporting this work (PRALTER no. 0516272). R.F. is greatly indebted to the Belgian "Fonds de la Recherche Scientifique – FNRS" for the award of a postdoctoral research grant.

Appendix A. Supplementary data

Supplementary data associated with this article can be found, in the online version, at doi:10.1016/j.bcp.2010.01.007.

References

[1] McInnes IB, Schett G. Cytokines in the pathogenesis of rheumatoid arthritis. Nat Rev Immunol 2007;7(6):429–42.
[2] Martinon F, Tschopp J. NLRs join TLRs as innate sensors of pathogens. Trends Immunol 2005;26(8):447–54.
[3] Yamaguchi K, Shirakabe T, Shibuya H, Irie K, Oishi I, Ueno N, et al. Identification of a member of the Mapkkk family as a potential mediator of Tgf-Beta signal-transduction. Science 1995;270(5244):2008–11.
[4] Sato S, Sanjo H, Takeda K, Ninomiya-Tsuji J, Yamamoto M, Kawai T, et al. Essential function for the kinase TAK1 in innate and adaptive immune responses. Nat Immunol 2005;6(11):1087–95.
[5] Shim JH, Xiao C, Paschal AE, Bailey ST, Rao P, Hayden MS, et al. TAK1, but not TAB1 or TAB2, plays an essential role in multiple signaling pathways in vivo. Genes Dev 2005;19(22):2668–81.
[6] Vallabhapurapu S, Karin M. Regulation and function of NF-kappaB transcription factors in the immune system. Annu Rev Immunol 2009;27:693–733.
[7] Dejardin E. The alternative NF-kappaB pathway from biochemistry to biology: pitfalls and promises for future drug development. Biochem Pharmacol 2006;72(9):1161–79.
[8] Vallabhapurapu S, Matsuzawa A, Zhang W, Tseng PH, Keats JJ, Wang H, et al. Non-redundant and complementary functions of TRAF2 and TRAF3 in a ubiquitination cascade that activates NIK-dependent alternative NF-kappaB signaling. Nat Immunol 2008;9(12):1364–70.
[9] Liao GX, Zhang MY, Harhaj EW, Sun SC. Regulation of the NF-kappa B-inducing kinase by tumor necrosis factor receptor-associated factor 3-induced degradation. J Biol Chem 2004;279(25):26243–50.
[10] Claudio E, Brown K, Park S, Wang H, Siebenlist U. BAFF-induced NEMO-independent processing of NF-kappa B2 in maturing B cells. Nat Immunol 2002;3(10):958–65.
[11] Coope HJ, Atkinson PG, Huhse B, Belich M, Janzen J, Holman MJ, et al. CD40 regulates the processing of NF-kappaB2 p100 to p52. EMBO J 2002;21(20):5375–85.
[12] Dejardin E, Droin NM, Delhase M, Haas E, Cao Y, Makris C, et al. The lymphotoxin-beta receptor induces different patterns of gene expression via two NF-kappaB pathways. Immunity 2002;17(4):525–35.
[13] Flohr S, Pyrazoloisoquinoline derivatives as kinase inhibitors. In: PCT Int. Appl. US 6,841,556, 2005.
[14] Altschul SF, Madden TL, Schaffer AA, Zhang JH, Zhang Z, Miller W, et al. Gapped BLAST and PSI-BLAST: a new generation of protein database search programs. Nucleic Acids Res 1997;25(17):3389–402.
[15] Berman HM, Westbrook J, Feng Z, Gilliland G, Bhat TN, Weissig H, et al. The protein data bank. Nucleic Acids Res 2000;28(1):235–42.
[16] Lambert C, Leonard N, De Bolle X, Depiereux E. ESyPred3D: prediction of proteins 3D-structures. Bioinformatics 2002;18(9):1250–6.
[17] Laskowski RA. PDBsum: summaries and analyses of PDB structures. Nucleic Acids Res 2001;29(1):221–2.
[18] Tripos I, SYBYL. 1699 South Hanley Rd., St. Louis, Missouri, 63144, USA.
[19] Brown K, Vial SC, Dedi N, Long JM, Dunster NJ, Cheetham GM. Structural basis for the interaction of TAK1 kinase with its activating protein TAB1. J Mol Biol 2005;354(5):1013–20.
[20] Lei M, Robinson MA, Harrison SC. The active conformation of the PAK1 kinase domain. Structure 2005;13(5):769–78.
[21] Sali A, Blundell TL. Comparative protein modelling by satisfaction of spatial restraints. J Mol Biol 1993;234(3):779–815.
[22] Ghose AK, Herbertz T, Pippin DA, Salvino JM, Mallamo JP. Knowledge based prediction of ligand binding modes and rational inhibitor design for kinase drug discovery. J Med Chem 2008;51(17):5149–71.
[23] LCC DS, Pymol. 2008.
[24] Ruegg UT, Burgess GM. Staurosporine, K-252 and UCN-01: potent but non-specific inhibitors of protein kinases. Trends Pharmacol Sci 1989;10(6):218–20.
[25] Jones G, Willett P, Glen RC, Leach AR, Taylor R. Development and validation of a genetic algorithm for flexible docking. J Mol Biol 1997;267(3):727–48.
[26] Saloutin VIYVB, Skryabina ZE, Kuzueva OG. Synthesis of fluoroalkyl-containing 2-oxyimino-1,3-dicarbonylcompounds and their reaction with hydrazine hydrate. J Fluorine Chem 1997;84:107.
[27] Majid T, Hopkins CR, Pedgrift B, Collar N. Convenient synthesis of 4-amino-3,5-disubstituted pyrazoles in one-step from the corresponding diketo oximes. Tetrahedron Lett 2004;45(10):2137–9.
[28] Pictet AG. Alfons, new method for the synthetic preparation of isoquinoline bases. Berichte der Dtsch Chemischen Gesellschaft 1910;43:2384–91.
[29] Gaestel M, Kotlyarov A, Kracht M. Targeting innate immunity protein kinase signalling in inflammation. Nat Rev Drug Discov 2009;8(6):480–99.
[30] Tang M, Wei X, Guo Y, Breslin P, Zhang S, Wei W, et al. TAK1 is required for the survival of hematopoietic cells and hepatocytes in mice. J Exp Med 2008;205(7):1611–9.
[31] ^{33}PanQinase® Activity Assay performed by ProQinase, Freiburg, Germany.
[32] Lanthascreen® Eu Kinase Binding Assay performed by Invitrogen Limited, Paisley, Scotland, United Kingdom.

Please cite this article in press as: Mortier J, et al. Pyrazolo[4,3-c]isoquinolines as potential inhibitors of NF-κB activation. Biochem Pharmacol (2010), doi:10.1016/j.bcp.2010.01.007